

Ph. D. Dissertation

고속, 고분해능, 그리고 편광 민감 테라헤르츠
분광 기술 개발에 관한 연구

Development of high-speed, high-resolution, and polarization-sensitive te-
rahertz spectroscopic techniques



김 영 찬 (金 永 燦 Kim, Youngchan)

Department of Physics

KAIST

2011

고속, 고분해능, 그리고 편광 민감 테라헤르츠
분광 기술 개발에 관한 연구

Development of high-speed, high-resolution, and polarization-sensitive te-
rahertz spectroscopic techniques



Development of high-speed, high-resolution, and polarization-sensitive terahertz spectroscopic techniques

Advisor : Professor Ahn, Jaewook

by

Kim, Youngchan

Department of Physics

KAIST

A thesis submitted to the faculty of KAIST in partial fulfillment of the requirements for the degree of Doctor of Philosophy in the Department of Physics. The study was conducted in accordance with Code of Research Ethics¹

2011. 04. 04

Approved by

Professor Ahn, Jaewook

[Advisor]

¹Declaration of Ethical Conduct in Research: I, as a graduate student of KAIST, hereby declare that I have not committed any acts that may damage the credibility of my research. These include, but are not limited to: falsification, thesis written by someone else, distortion of research findings or plagiarism. I affirm that my thesis contains honest conclusions based on my own careful research under the guidance of my thesis advisor.

고속, 고분해능, 그리고 편광 민감
테라헤르츠 분광 기술 개발에 관한 연구

김 영 찬

위 논문은 한국과학기술원 박사학위논문으로
학위논문심사위원회에서 심사 통과하였음.

The logo for KAIST (Korea Advanced Institute of Science and Technology) is displayed in a light blue color. It consists of the letters 'KAIST' in a bold, sans-serif font, with a horizontal line underneath the letters.

2011 년 4 월 4 일

심사위원장 안 재 욱 (인)

심사위원 공 홍 진 (인)

심사위원 박 용 근 (인)

심사위원 윤 춘 섭 (인)

심사위원 이 대 수 (인)

DPH
20085035

김 영 찬. Kim, Youngchan. Development of high-speed, high-resolution, and polarization-sensitive terahertz spectroscopic techniques. 고속, 고분해능, 그리고 편광 민감 테라헤르츠 분광 기술 개발에 관한 연구. Department of Physics. 2011. 89 p. Advisor Prof. Ahn, Jaewook. Text in English

ABSTRACT

Conventional terahertz time-domain spectroscopy (THz-TDS), which uses a single mode-locked femto-second (fs) laser and a mechanical delay method, has an inherent tradeoff between frequency resolution and measurement time since the frequency resolution is equal to the reciprocal of the overall time delay. Recently, asynchronous optical sampling (ASOPS) technique, which employs two fs lasers with slightly different repetition frequencies without a mechanical delay line, has been applied to THz-TDS to overcome the shortcomings of the conventional THz-TDS such as the trade-off between measurement time and time delay window, and the residual variation of beam pointing owing to the use of a mechanical delay line. Although the ASOPS technique was invented and used for time-resolved pump-probe spectroscopy in 1987, it was in 2005 that the ASOPS technique was firstly applied for THz-TDS. Therefore, previous researches on THz spectroscopic technique using THz frequency comb are immature that there is room to enhance the spectroscopic techniques such as the measurement speed by avoiding the unnecessary time delay scanning.

In this thesis, we have developed and demonstrated various high-speed, high-resolution, and polarization sensitive THz spectroscopic techniques. First, we have demonstrated and characterized two known high-speed, high-resolution THz spectroscopy: ASOPS THz-TDS and THz frequency comb spectroscopy (TFCS). For this, we have investigated stabilization of the repetition frequencies of the fs lasers and difference frequency optimization. As a central part of this thesis, we have demonstrated three new high-speed, high-resolution THz spectroscopic techniques: (1) wavelet power spectrum estimation technique (WPSET), (2) THz frequency-comb multiheterodyne spectroscopy (TFCMS), and (3) electronically controlled optical sampling (ECOPS) THz-TDS. We have successfully applied WPSET, a denoising technique, to this high-resolution THz-TDS. TFCMS has been newly implemented and proved its spectroscopic capability as a high-resolution THz time-domain spectroscopy. Through the characterization of water vapor absorption lines, and ammonia, the high resolution capability of TFCMS has been tested. Also we have devised and implemented ECOPS THz-TDS, where the time delay between the two laser pulses have been rapidly swept by an external offset voltage applied to a locking electronics at a fast scan rate of 1 kHz. Lastly, we have developed a polarization sensitive THz spectroscopic technique. Using this technique, we have investigated the THz birefringence in various condensed matters, such as ZnO, Al₂O₃ and LiNbO₃, and the results are verified with *ab initio* calculations.

Keywords: Terahertz, Terahertz time-domain spectroscopy, Asynchronous optical sampling, Birefringence

Contents

Abstract	i
Contents	ii
List of Tables	iv
List of Figures	v
Chapter 1. Introduction	1
Chapter 2. Asynchronous optical sampling THz spectrometers	6
2.1 Introduction	6
2.2 Principles of operation	6
2.2.1 ASOPS THz-TDS	6
2.2.2 THz frequency comb spectroscopy (TFCS)	7
2.3 Experimental apparatus	9
2.3.1 ASOPS THz-TDS	9
2.3.2 TFCS	9
2.3.3 Stabilization of repetition frequencies	10
2.4 Results and data analysis	12
2.4.1 ASOPS THz-TDS	12
2.4.2 TFCS	18
2.5 Discussion	20
Chapter 3. Advanced high-speed, high-resolution THz spectroscopy techniques	21
3.1 Introduction	21
3.2 Wavelet power spectrum estimation technique	21
3.2.1 Introduction	21
3.2.2 Experiment	22
3.2.3 Theoretical description of the WPSET	25
3.2.4 Spectrum denoising by the WPSET	29
3.3 Terahertz frequency-comb multiheterodyne spectroscopy	33
3.3.1 Introduction	33
3.3.2 Principles of operation	34

3.3.3 Experiment	36
3.3.4 Results and data analysis	39
3.4 Electronically controlled optical sampling THz-TDS	44
3.4.1 Introduction	44
3.4.2 Principles of operation	45
3.4.3 Experiment	45
3.4.4 Results and data analysis	47
3.5 Discussion	51
Chapter 4. Polarization-sensitive THz-TDS	53
4.1 Introduction	53
4.2 THz birefringence in ZnO	54
4.2.1 Introduction	54
4.2.2 Experiment	55
4.2.3 Experimental results	57
4.2.4 <i>Ab initio</i> calculation and discussion	58
4.3 THz birefringence in LiNbO ₃ , and Al ₂ O ₃	65
4.3.1 Introduction	65
4.3.2 Polarization sensitive THz detection	67
4.3.2 Measurement for THz birefringence	69
4.3.3 Calculation for THz birefringence	71
4.4 Discussion	75
Chapter 5. Conclusion	76
Reference	78
Summary (in Korean)	84

List of Tables

2.1: Measurement conditions under which the results of Fig. 2.5 were obtained.	14
2.2: Absorption lines of water vapor in the frequency range from 0.1 to 1.5 THz.	14
3.1: Center frequencies, linewidths, and transmittances of the absorption lines extracted from the raw and denoised transmission spectra of water vapor.	32
3.2: Fitting Parameters for Water Vapor Absorption Lines in Fig. 3.14(a).	43
4.1: Classical oscillator fitting parameter for Al_2O_3 [80,81].	73
4.2: Measured and calculated refractive indices of Al_2O_3 and LiNbO_3 at 1 THz.	74

The logo for KAIST (Korea Advanced Institute of Science and Technology) is centered on the page. It consists of the letters "KAIST" in a bold, blue, sans-serif font. Below the text is a light blue, horizontal, oval-shaped shadow or gradient effect.

List of Figures

1.1: THz gap in the electromagnetic spectrum.	1
1.2: Schematic of a conventional setup for THz-TDS using fs optical pulses.	3
1.3: Principles of THz pulse generation (a) and detection via photoconductive antenna (PCA). (Image courtesy of Teraview corp.)	3
1.4: (a) Typical THz time-domain data. (b) THz spectrum obtained by using a FFT of the time-domain waveform in (a).	4
2.1: (a) Illustration of the principle of the ASOPS THz-TDS in the time-domain. (b) Illustration of the principle of the TFCS in the frequency domain.	8
2.2: (a) Experimental setup for ASOPS THz-TDS, (EM: THz emitter, DT: THz detector, PM: off-axis parabolic mirror, PD: photodetector, Amp1: current amplifier, Amp 2: variable-gain current amplifier, NOC: nonlinear optical crystal). (b) Our experimental setup for TFCS.	10
2.3: (a) A schematic diagram of the phase-locked loops; optical paths are represented by red solid lines and electrical signals by black dashed lines, (DRO: dielectric resonator oscillator, DBM: double-balanced mixer, PI Amp: proportional-integral amplifier, HV Amp: high-voltage amplifier, PD: photodetector). (b) A single-scan cross-correlation signal (blue line) between the two fs lasers using non-collinear sum-frequency generation and a cross-correlation signal averaged over 10000 scans (black line).	11
2.4: (a) A typical time-domain waveform on a 10 ns time window measured from ASOPS THz-TDS. (b) THz spectrum obtained by using a FFT of the time-domain waveform in (a).	15
2.5: SNR versus difference frequency.	16
2.6: SNR versus measurement time. The red line is a fit to the data in the form of $Y = \alpha * X^\beta$	16
2.7: (a) THz transmittance spectrum of water vapor. (b) Experimental data (black dot) and its Lorentz fit (red line) with respect to the absorption line 1 of water vapor.	17
2.8: (a) Typical spectrum measured from TFCS. (b) THz frequency comb modes are clearly resolved at around 0.5 THz.	19
3.1: Experimental setup for ASOPS THz-TDS. PD: photodetector, EM: THz emitter, DT: THz detector, PM: off-axis parabolic mirror, Amp: variable-gain current amplifier, and NOC: nonlinear optical crystal.	23

3.2: (a) Typical time-domain waveform on a 10 ns time delay window measured from ASOPS THz-TDS at relative humidity of 28 %. (b) THz amplitude spectrum obtained by FFT of the time-domain waveform in (a).	24
3.3: THz amplitude spectra of wavelet-denoised time-domain waveforms. The orange lines show the raw spectrum in Fig. 3.2(b) and the black lines the spectra of the time-domain waveforms that are denoised using the Daubechies wavelet with 10 vanishing moments at the scale of 5 for a low (a) and high (b) threshold value, respectively. The low threshold can scarcely remove the fluctuation, whereas the high threshold distorts the singularities.	26
3.4: THz amplitude spectrum denoised by using the WPSET. The orange and black lines display the raw and denoised spectra, respectively.	29
3.5: Magnified views at around 1.16 THz of the raw spectrum (a) and the spectra denoised using the Haar wavelet at the scale of 5 (b), the Daubechies wavelet with 10 vanishing moments at the scale of 4 (c), and the Daubechies wavelet with 10 vanishing moments at the scale of 5, respectively.	30
3.6: THz transmission spectra of water vapor resulting from the raw (orange line) and denoised (black line) amplitude spectra. The inset is an enlarged view around 1.16 THz.	30
3.7: Frequency-dependent refractive index (a) and absorption coefficient (b) of ZnO. The raw and denoised results are indicated by the orange and black lines, respectively.	31
3.8: Illustration of the principles of the TFCMS in (a) the time domain and (b) the frequency domain.	35
3.9: Schematic diagram of the experimental setup for THz-FC multiheterodyne spectroscopy. PD: photodetector, DRO: dielectric resonator oscillator, SG: signal generator, PLL: phase-locked loop, EM: THz emitter (PCA here), Amp: preamplifier, and NOC: nonlinear optical crystal.	38
3.10: Cross-correlation signal between two optical pulses emitted from the fs lasers. The blue line indicates the trigger pulse used to trigger the digitizer and the black one the subsequent pulse 50 ms away from the trigger pulse, with Δf_r set to 20 Hz.	38
3.11: Typical interferogram measured from THz-FC multiheterodyne spectroscopy. With Δf_r set to 20 Hz, 10,000 interferogram traces acquired during 1,000 s were averaged to enhance the SNR. The inset shows a zoom into the interferogram at the zero time delay.	40
3.12: THz power spectra obtained by FFT of interferograms measured with Δf_r of 20 (black line) and 100 (red line) Hz. The spectrum acquired with Δf_r of 20 Hz is broader than that with Δf_r of 100 Hz.	41
3.13: The Peak SNR of the THz power spectrum versus the measurement time. The closed circles are experimental results and the red line a fitting result of them.	42

3.14: (a) THz transmission spectrum of water vapor (black line) and the dynamic range limit (orange dot) in the frequency range up to 2 THz. (b) A zoom into the spectrum in (a) around 1.16 THz.	42
3.15: Power absorption spectrum (gray line) of ammonia at 1 atm in the frequency range up to 2 THz, measured using a gas cell. The black line displays the denoised spectrum through the wavelet power spectrum estimation.	44
3.16: Schematic diagram of the experimental setup for ECOPS THz-TDS. DBM: double-balanced mixer, PI Amp: proportional-integral amplifier, HV Amp: high-voltage amplifier, PD: photodetector, EM: THz emitter, DT: THz detector, PM: off-axis parabolic mirror, Amp: preamplifier. Optical beams are represented by red lines, electrical signals by black solid lines, and 10 MHz reference signals by black dashed lines, respectively.	46
3.17: Schematic diagram of the time delay measurement setup. LPF1: 100 MHz low-pass filter, LPF2: 1.9 MHz low-pass filter. (b) Signal (blue line) measured from the time delay measurement setup and temporal variation of the time delay (red line) determined from the signal by Eq. (3.22) when the time delay is swept at a scan rate of 1 kHz by the ECOPS system.	48
3.18: The dashed curve represents a single scan trace of cross-correlation signal and the solid curve an average over 1,000 scans of cross-correlation signal.	48
3.19: (a) Typical THz temporal waveforms measured by ECOPS and ASOPS. (b) THz amplitude spectra obtained by FFT of the waveforms in (a). The black and red curves indicate ECOPS and ASOPS results, respectively.	49
3.20: SNR versus measurement time for THz pulse measurements using ECOPS and ASOPS. The black dots represent ECOPS results and the red dots ASOPS results. The lines are fits of the results to $Y = \alpha * X^\beta$	51
4.1: Brief procedure of <i>ab initio</i> calculation using the CRYSTAL09.	54
4.2: Illustration of the experimental configuration. PM: off-axis parabolic mirror, EM: THz emitter, DT: THz detector, o: ordinary axis, and e: extraordinary axis.	56
4.3: Transmitted THz waveforms (a) measured with varying the azimuthal angle φ of the ZnO sample in the parallel-polarization configuration illustrated in (b), and measured ordinary and extraordinary refractive indices (c) of the ZnO sample. The solid curves in (a) represent the waveforms measured at 90° and 180°, respectively.	60
4.4: (a) Frequency-dependent phase retardation through the 2-mm-thick ZnO crystal. (b) THz transmission spectra of the 2-mm-thick ZnO crystal measured at various azimuthal angles in the parallel-polarization configuration.	61

4.5: Azimuthal angle dependence of transmittances at 0.42 and 1.24 THz of the 2-mm-thick ZnO crystal, measured in the parallel-polarization configuration. The 0° (180°) and 90° (270°) orientations represent extraordinary and ordinary waves, respectively.	62
4.6: <i>Ab initio</i> calculation results for the ZnO. (a) Real and (b) imaginary part of complex dielectric constant, and (c) real and (d) imaginary part of complex refractive index of ZnO in the frequency range between 0 and 30 THz for the extraordinary (red line) and ordinary (blue line) waves, respectively.	63
4.7: Calculated birefringence in the frequency range between 0 to 30 THz. Note that the imaginary part of the complex refractive index is huge in the larger birefringence region from 5 THz to 20 THz, as shown in Fig. 4.6.	64
4.8: Refractive indices and absorption coefficients of ZnO in the THz region for the extraordinary (red curve) and ordinary (blue curve) waves, obtained from the <i>ab initio</i> calculation. The dashed curves indicate experimental results.	64
4.9: The atomic structure of LiNbO ₃ . [36]	66
4.10: The atomic structure of Al ₂ O ₃ . [37]	66
4.11: Illustration of the experimental configuration. PCA: photoconductive antenna, WP: Wollaston prism, QWP: quarter waveplate, Pellicle b/s: Pellicle beamsplitter, o: ordinary axis, and e: extraordinary axis. The directions of the generated and detected THz polarizations are depicted beside the THz emission and detection parts, respectively. The inset shows the angles of the THz and probe beam polarization directions with respect to the (001) axis of the ZnTe crystal.	68
4.12: THz polarization-dependent THz time-domain waveforms (arbitrary units) measured with varying the THz polarization angle α with respect to the (001) axis of the ZnTe crystal.	68
4.13: Transmitted THz time-domain waveforms (arbitrary units) measured with varying the azimuthal angle θ of the LiNbO ₃	70
4.14: Measurement of THz waveforms with and without the sample. The frequency dependent complex refractive index of sample, $\tilde{n}_s(\omega)$, is obtained from Eqs (4.7) and (4.8).	70
4.15: Dispersion of measured ordinary and extraordinary refractive indices of Al ₂ O ₃ and LiNbO ₃ . The extraordinary and ordinary waves are indicated by the red and blue curves, respectively.	71
4.16: Dispersion of calculated ordinary and extraordinary refractive indices of Al ₂ O ₃ and LiNbO ₃ by using an <i>ab initio</i> calculation. The extraordinary and ordinary waves are indicated by the red and blue curves, respectively.	74

Chapter 1. Introduction

Terahertz (THz) radiation is electromagnetic radiation whose frequency lies between the microwave and infrared bands of spectral ranging from 0.1 THz to 10 THz (where 1 THz is 10^{12} cycles/s), as shown in Fig. 1.1. The electromagnetic radiation at 1 THz has a period of 1 ps, a wavelength of 300 μm , a wave number of 33 cm^{-1} , a photon energy of 4.1 meV, and an equivalent temperature of 47.6 K. Even though we cannot see the THz radiation, it is a natural part of our environment. However, the electromagnetic spectrum of THz radiation remains the least explored part mainly due to the inefficient generation and detection techniques and high atmospheric absorption for the THz radiation. Over the last two decades, research interest in the field of the THz electromagnetic radiation has increased with the development of THz science and technology [1-3]. THz research field is enabling to be applied in many sectors. The photon energy of THz radiation is typically considered to occupy energy between 0.4 meV and 80 meV, which corresponds to the range of fundamental energies associated with changes between molecular energy levels [4]. Also, the photon energy spans the range of low-energy excitations in electronic materials [5] and vibrational and rotational transitions in molecules [6], many materials extending from gases and liquids to solid-state and biological media have complex dielectric response in the THz frequency range [7]. When a molecule interacts with THz photons, the molecule may absorb the THz photons with particular energies and change its quantized states. In particular, since many rotational lines of constituent molecules exist within the THz gap compared with the radio waves and IR ranges, the atmospheric absorption is exceedingly high in the THz gap [4]. Furthermore THz radiation has been a promising candidate for nondestructive evaluation of the internal structures of targets since THz radiation is transparent to most of dry dielectric materials [8-10]. Therefore the THz frequency is a key spectral region for probing fundamental physical interactions, as well as for practical applications such as medical imaging, homeland security, environmental monitoring and process monitoring in manufacturing.

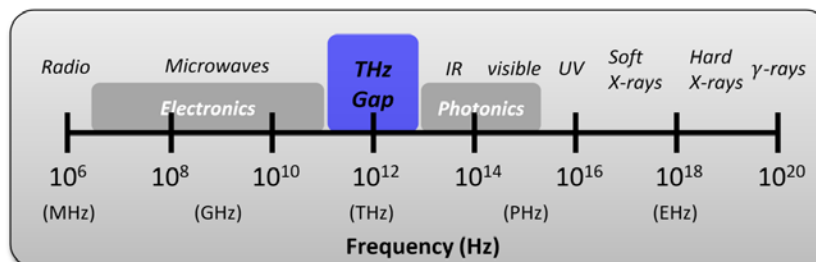


Figure 1.1: THz gap in the electromagnetic spectrum.

Over the last two decades, the THz field has made remarkable progress with terahertz time-domain spectroscopy (THz-TDS). The experimental configuration of THz-TDS is depicted in Fig. 1.2. The principle of conventional THz-TDS using photoconductive antennas for THz generation and detection is that pump pulse from the femtosecond (fs) laser are incident on a THz emitter to generate THz pulses, which are guided into the THz detector by using four off-axis parabolic mirrors. Probe pulses from the same laser are used to optically sample the THz pulses incident upon a THz detector. A photocurrent output from the THz detector represents the magnitude of the electric field of the THz pulses temporally sampled. In this case, photoconductive antennas are used as the THz emitter and THz detector. The principles of operating method to generate and detect THz wave via photoconductive antenna are shown in Fig. 1.3. It is noteworthy that THz-TDS has been pioneered as a basic measurement tool for characterizing optical and electrical properties of materials using the phase and amplitude of the THz pulse at each frequency [11,12]. THz-TDS also provides a potentially attractive method for probing fundamental physical interactions as well as practical applications [1-3,13]. Figure 1.4 shows the typical THz time domain data and its spectrum. There are two main advantages in THz-TDS system. Although the THz power is generally fairly weak in a THz-TDS system, the measurement dynamic range could be as high as 10^6 benefiting from the nature of time gating and coherent detection, thus background noise is dramatically suppressed. Another advantage of THz-TDS is its intrinsic temporal resolution, which allows it to provide ps temporal resolution in a dynamic spectroscopy. Conventional THz-TDS combines the pulse generation by using a fs laser onto a nonlinear crystal or photoconductive antenna with a coherent detection by using an electro-optic crystal or also a photoconductive antenna [1,7].

The recording speed in conventional THz-TDS is mainly dependent upon the scanning time delay in sampling process. Therefore, conventional THz-TDS, which uses a single mode-locked fs laser and a mechanical delay method, has an inherent tradeoff between frequency resolution and measurement time, or the frequency resolution is equal to the reciprocal of the overall time delay window. Generally, translational stage methods need a measurement time of several minutes, though they enable a time delay scan up to hundreds of picoseconds. Contrarily, a vibrating mirror can scan faster with a rate of up to 100 Hz, but its measurement time window is limited to less than 100 ps. Also, there exist unconventional types of optical delay lines which enable rapid data acquisition or high spectral resolution [14,15]. Recently, asynchronous optical sampling (ASOPS) THz-TDS using THz frequency comb has been introduced to overcome this tradeoff, which employs two fs lasers with slightly different stabilized repetition frequencies for THz wave generation and detection respectively so that a maximum time delay window can be obtained at a high scan rate [16-19]. Moreover, precise frequency metrology has been actively studied through the THz frequency comb [20].

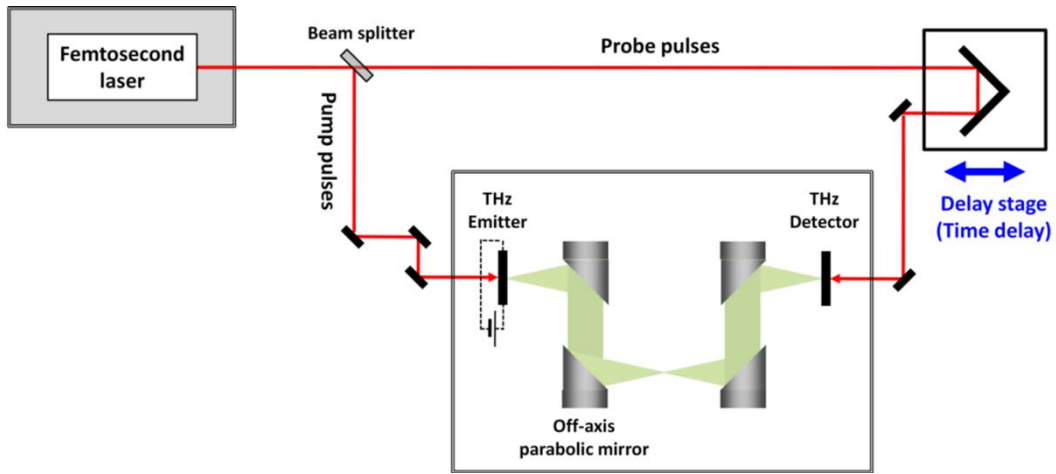


Figure 1.2: Schematic of a conventional setup for THz-TDS using fs optical pulses.

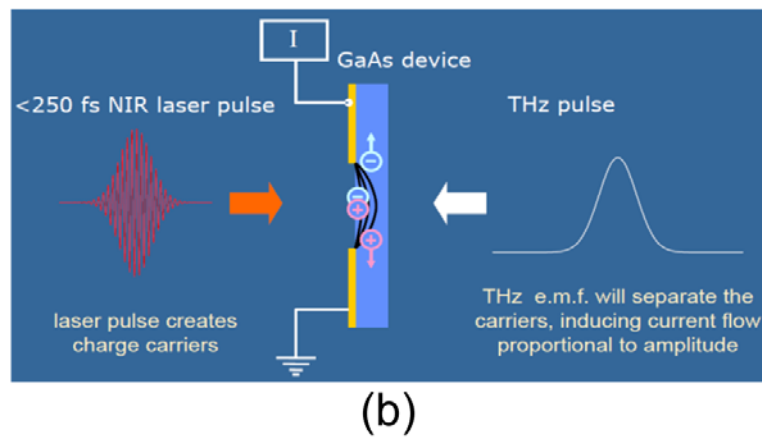
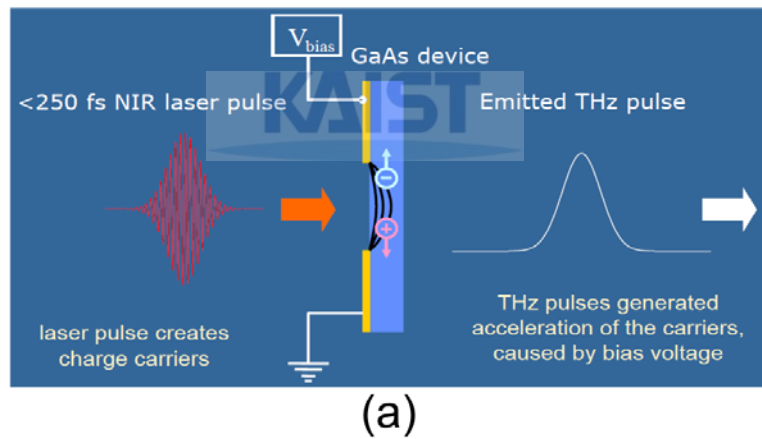


Figure 1.3: Principles of THz pulse generation (a) and detection via photoconductive antenna (PCA). (Image courtesy of Teraview corp.)

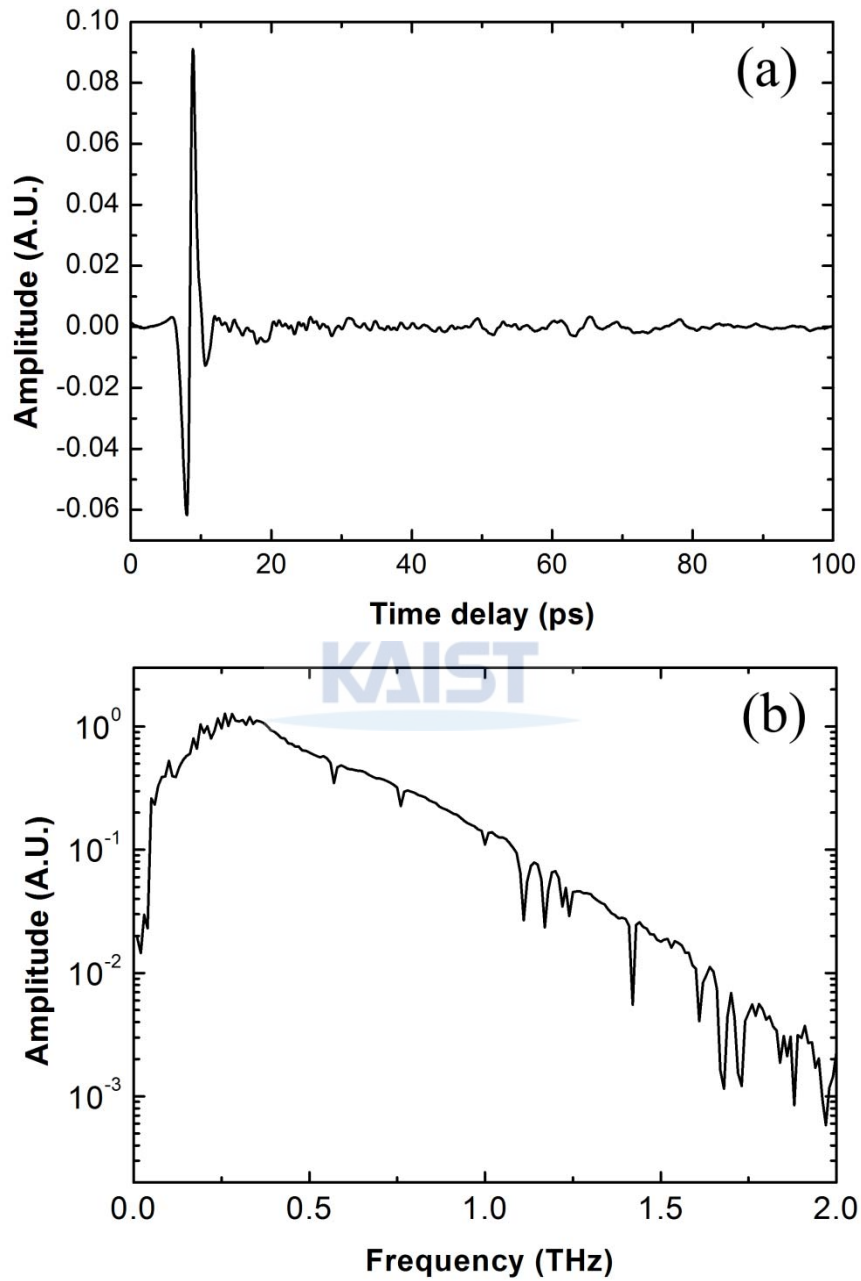


Figure 1.4: (a) Typical THz time-domain data. (b) THz spectrum obtained by using a FFT of the time-domain waveform in (a).

In this thesis, we have demonstrated and investigated high-speed, high-resolution, and polarization sensitive THz spectroscopic techniques. Moreover we have performed experimental measurements of THz birefringence in ZnO, LiNbO₃, and Al₂O₃ using the polarization sensitive THz-TDS and the experimental results are verified with *ab initio* calculations. The content of this thesis is organized as follow. In chapter 2, the basic theory and characteristics of ASOPS THz spectrometers are analyzed and discussed. We have summarized the principles of operation, stabilization of repetition frequencies of fs lasers, time delay resolution, optimization of repetition frequency difference of fs lasers, and typical experimental results. In chapter 3, three new high-speed, high-resolution THz-TDS techniques are introduced. They are (1) wavelet power spectrum estimation technique (WPSET), (2) THz frequency-comb multiheterodyne spectroscopy (TFCMS), and (3) electronically controlled optical sampling (ECOPS) THz-TDS are demonstrated. WPSET has been applied to high-resolution THz-TDS based on ASOPS technique. This WPSET removes noise-like fluctuations effectively above the background noise level of THz amplitude spectra without sacrificing spectral features. TFCMS is a new type of time-domain spectroscopy in the THz frequency region. The high resolution capability TFCMS has been demonstrated through the characterization of absorption lines of water vapor and ammonia gas. And we have demonstrated ECOPS-based high-speed THz-TDS. It has been confirmed that ECOPS can exactly reproduce a THz pulse of distortion-free spectrum, equivalent to a typical ASOPS measurement, by adopting a proper calibration of time-delay. In chapter 4, we have further developed a THz polarization sensitive time-domain spectroscopy, and applied it for the study of THz birefringence of various materials, such as ZnO, LiNbO₃, and Al₂O₃. For theoretical verifications, an *ab initio* band calculation and phonon calculation using CRYSTAL09 [21] have been considered. The results of *ab initio* calculation using the hybrid exchange-correlation function in the THz region, few meV range are in good agreement with the experimental results.

Chapter 2. Asynchronous optical sampling THz spectrometers

2.1 Introduction

THz-TDS using a coherent measurement method is one of the basic measurement tools in the THz field. A trade-off between frequency resolution and measurement time exists in conventional THz-TDS utilizing a single mode-locked fs laser because frequency resolution is inversely proportional to the overall time window. Recently, asynchronous optical sampling (ASOPS) has been proposed to be applied to THz-TDS to eliminate the trade-off [16,18,19,23], which should employ two fs lasers with slightly different repetition frequencies for THz wave generation and detection, respectively. ASOPS has been effectively applied to THz-TDS to achieve rapid data acquisition and high spectral resolution.

Frequency comb technology emerged in the fields of optical metrology and spectroscopy in 2000. Also, terahertz frequency comb spectroscopy (TFCS) has been recently demonstrated through generation and detection of a THz frequency comb [24,25]. The THz frequency comb has many attractive features for frequency metrology, such as high accuracy, broadband selectivity, and ultranarrow linewidth. Furthermore, it can be used as a precise ruler in the frequency domain because it is extended to the THz region with no offset frequency. Thus, TFCS can be an effective tool for identifying interesting molecules with spectral fingerprints in the THz range.

2.2 Principles of operation

2.2.1 ASOPS THz-TDS

The conventional THz-TDS utilizes a pump-probe measurement, where a single fs laser is employed to provide pump and probe pulses and an optical delay line is used to scan the time delay between pump and probe pulses. Usually, lock-in detection and signal modulation by mechanical or electro-optical chopping are performed in the pump-probe measurement. The ASOPS was used for time-resolved pump-probe spectroscopy in 1987 [26], where two fs lasers provided pump and probe pulses at different repetition frequencies so that the time delay between the pump and probe pulses was scanned with no use of a mechanical delay line. Also, THz-TDS using ASOPS has been demonstrated by use of fs lasers at a repetition frequency of 82.6 MHz and

1 GHz [16,23]. In the ASOPS THz-TDS, one fs laser gives pump pulses to generate THz pulses, and the other gives probe pulses to optically sample the THz pulses. The time delay is repetitively scanned at a difference frequency ($\Delta f = f_{r1} - f_{r2}$), where the f_{r1} and f_{r2} are stabilized repetition frequencies of fs lasers, as shown in Fig. 2.1(a). In our system, the repetition frequency of pump pulses (f_{r1}) is fixed at 100 MHz. The real time can be converted into the time delay by using

$$\tau \text{ (time delay)} = t \text{ (real time)} \times \frac{\Delta f}{f_{r1}}. \quad (2.1)$$

Since the time scaling factor ($\Delta f/f_{r1}$) is on the order of magnitude of 10^{-7} for our system, time-domain data of THz pulses can be acquired at a RF sampling rate by using a digital oscilloscope or digitizer.

2.2.2 THz frequency comb spectroscopy (TFCS)

Fig. 2.1(b) describes the principle of the TFCS in the frequency domain. Optical pulses from two fs lasers consist of optical modes whose frequencies are represented as

$$\begin{aligned} f_1 &= nf_{r1} + f_{o1}, \\ f_2 &= nf_{r2} + f_{o2}, \end{aligned} \quad (2.2)$$

where f_{r1} and f_{r2} are stabilized repetition frequencies, f_{o1} and f_{o2} are carrier-envelope offset frequencies, and n is an integer. Optical pulses from the fs laser 1 generate a THz frequency comb from a THz emitter, and those from the fs laser 2 generate photocarrier pulses in a THz detector. The THz frequency comb and photocarrier pulses are represented as

$$\begin{aligned} f_1 &= mf_{r1}, \\ f_2 &= mf_{r2}, \end{aligned} \quad (2.3)$$

where m is an integer. In a THz detector, photocurrent pulses are induced by the photocarrier pulses and the electric field of the THz frequency comb, which are represented as

$$f = m(f_{r1} - f_{r2}) = m\Delta f. \quad (2.4)$$

From Eqs. (2.3) and (2.4), the spectrum of the photocurrent pulses can be viewed as the spectrum of the THz frequency comb downscaled by a factor of $\Delta f/f_{r1}$ and can be directly measured using a RF spectrum analyzer. That is, the spectrum of a THz frequency comb can be measured by using multifrequency-heterodyne detection.

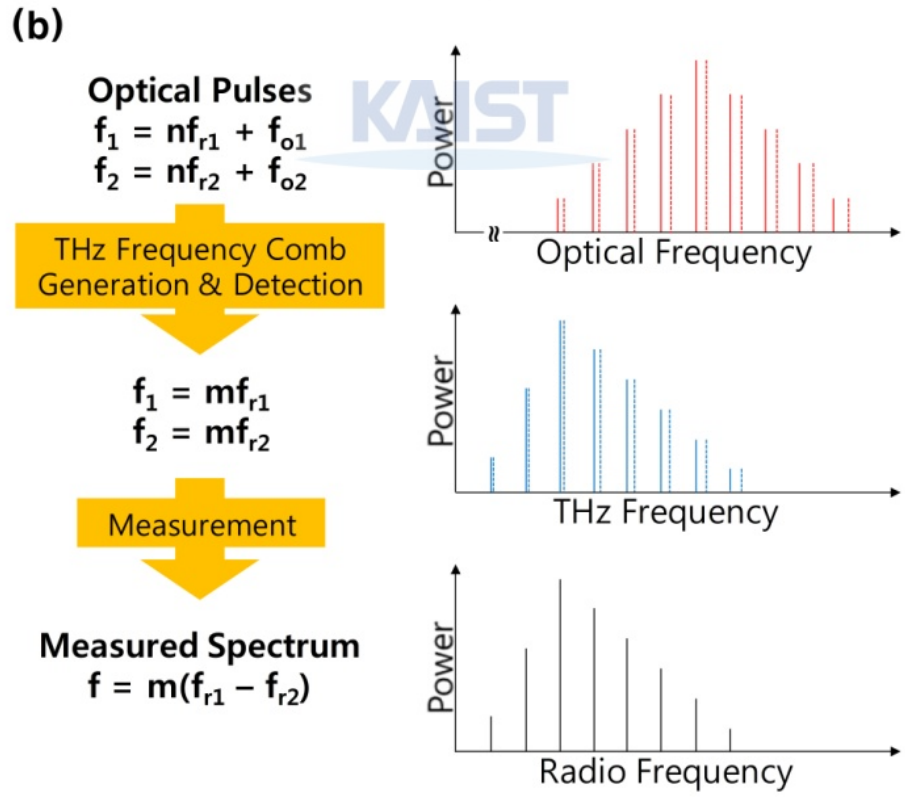
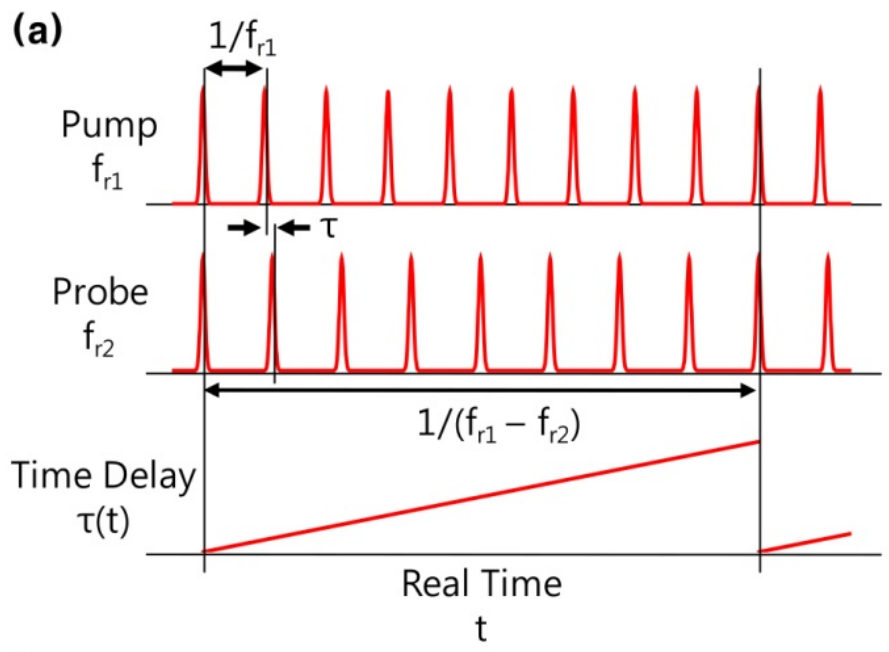


Figure 2.1: (a) Illustration of the principle of the ASOPS THz-TDS in the time-domain. (b) Illustration of the principle of the TFCS in the frequency domain.

2.3 Experimental apparatus

2.3.1 ASOPS THz-TDS

Our experimental setup for ASOPS THz-TDS is sketched in Fig. 2.2(a). We employ a laser system where the two fs lasers with repetition frequencies around 100 MHz are pumped by a diode-pumped solid state laser at a 532-nm wavelength. The whole laser system is placed on a temperature-controlled baseplate to avoid thermal fluctuations. The fs lasers have a center wavelength of 800 nm, and the pulse durations of fs lasers 1 and 2 are 10 and 20 fs, respectively. The repetition frequencies of the fs lasers are, respectively, stabilized by using two phase-locked loops to reduce the time jitter of the optical pulses, as explained below. We use two low-temperature-grown GaAs photoconductive antennas, one as a THz emitter (EM) and the other as a detector (DT).

Optical pulses from the fs laser 1 are incident on the EM to generate THz pulses, which are guided into the DT by using four off-axis parabolic mirrors. Optical pulses from the fs laser 2 are used to optically sample the THz pulses incident upon the DT. A photocurrent output from the DT represents the magnitude of the electric field of the THz pulses temporally sampled. It is amplified by using a variable-gain current amplifier and is then input to a 24-bit flexible resolution digitizer (National Instruments PXI-5922). The digitizer is triggered by a sum-frequency signal generated from a nonlinear optical crystal (2-mm-thick BBO crystal) on which optical pulses from the two fs lasers are non-collinearly focused. The trigger signal has a repetition frequency equal to the difference frequency. We can acquire time-domain data by using the digitizer, and we can average repetitive scans to enhance the signal-to-noise ratio (SNR). The time axis of the time-domain data is converted from a real time to a time delay according to Eq. (2.1); then, a THz spectrum is obtained by Fourier-transforming the time-domain data.

2.3.2 TFCS

Fig. 2.2(b) depicts our experimental setup for TFCS, which is the same as that for ASOPS THz-TDS except for the data acquisition part. A THz frequency comb generated from the EM by using repetition-frequency-stabilized optical pulses is incident upon the DT via four off-axis parabolic mirrors. Through multifrequency-heterodyne detection, the spectrum of a THz frequency comb is measured with a RF spectrum analyzer (Agilent Technologies N9020A-526).

2.3.3 Stabilization of repetition frequencies

We use two phase-locked loops to stabilize the repetition frequencies of the fs lasers. A schematic diagram of the phase-locked loops is displayed in Fig. 2.3(a). f_{r1} and f_{r2} are phase-locked to a fixed frequency of 100 MHz and a variable frequency, respectively, so that the difference frequency can be adjusted. By using double-balanced mixers (DBM), the tenth harmonics of f_{r1} and f_{r2} are compared with the outputs of a 1-GHz dielectric resonator oscillator (DRO) and a signal generator (Agilent Technologies N5181A), respectively. The DRO and the signal generator share a 10-MHz reference oscillator to reduce the relative time jitter between optical pulses from the two fs lasers. The phase error signal output from the DBM is amplified by using a proportional-integral amplifier (PI amp) and a high-voltage amplifier (HV amp) and is supplied to a piezoelectric transducer (PZT) to which a cavity mirror is attached. The repetition frequencies are stabilized by controlling the cavity lengths via the PZTs.

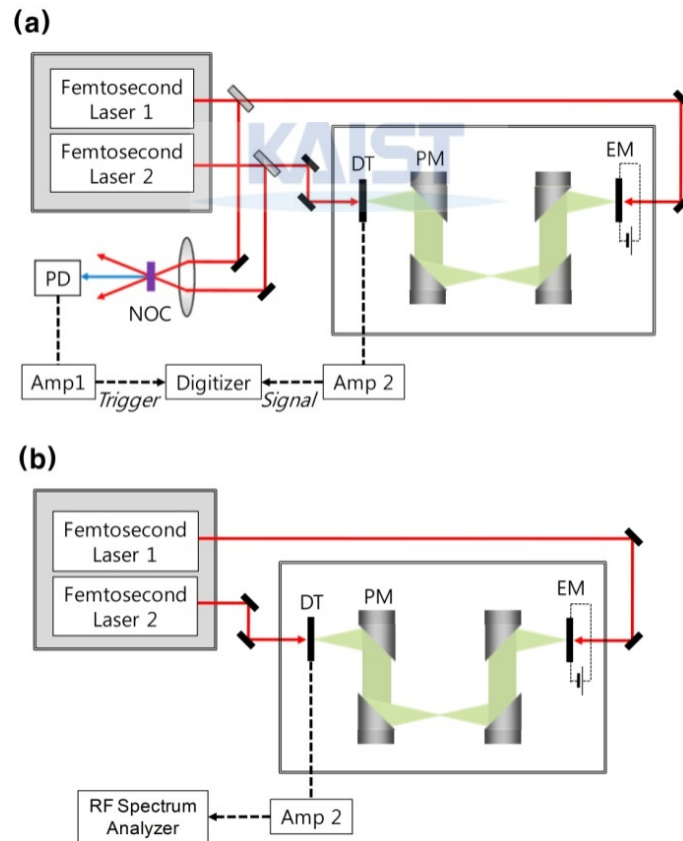


Figure 2.2: (a) Experimental setup for ASOPS THz-TDS, (EM: THz emitter, DT: THz detector, PM: off-axis parabolic mirror, PD: photodetector, Amp1: current amplifier, Amp 2: variable-gain current amplifier, NOC: nonlinear optical crystal). (b) Our experimental setup for TFCS.

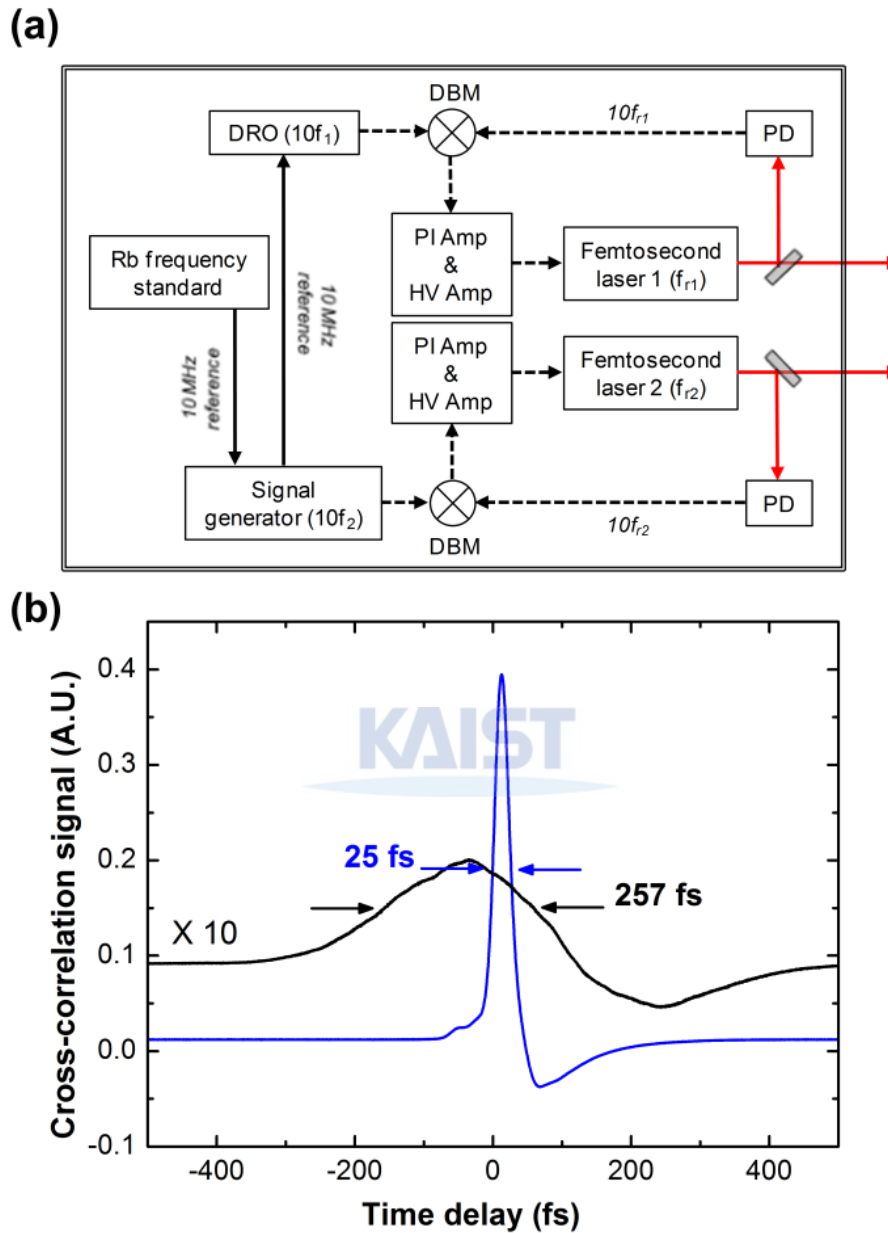


Figure 2.3: (a) A schematic diagram of the phase-locked loops; optical paths are represented by red solid lines and electrical signals by black dashed lines, (DRO: dielectric resonator oscillator, DBM: double-balanced mixer, PI Amp: proportional-integral amplifier, HV Amp: high-voltage amplifier, PD: photodetector). (b) A single-scan cross-correlation signal (blue line) between the two fs lasers using non-collinear sum-frequency generation and a cross-correlation signal averaged over 10000 scans (black line).

To evaluate stabilization performance of the phase-locked loops, we performed optical cross-correlation measurements, where a sum-frequency signal is generated from a nonlinear optical crystal (2-mm-thick BBO crystal) on which optical pulses from the two fs lasers are non-collinearly focused. Figure 2.3(b) shows optical cross-correlation results obtained when the difference frequency is set to 100 Hz and the sum-frequency signal is detected by a photodetector with a bandwidth of 12.5 MHz. As shown by the blue line, a single scan of cross-correlation has a full width at half maximum (FWHM) of 25 fs, which results from broadening of the optical pulse due to dispersion and the response time of the photodetector. The black line displays a cross-correlation signal averaged over 10000 repetitive scans of the adjacent pulse 10 ms apart from the trigger pulse. It shows a FWHM of 257 fs, which is wider than the FWHM of a single scan and is caused by the relative timing jitter between the optical pulses from the two fs lasers. The time resolution of our system can be taken to be 257 fs.

2.4 Results and data analysis

2.4.1 ASOPS THz-TDS



Typical time-domain data on a 10-ns time window measured from ASOPS-THz TDS are shown in Fig. 2.4(a). With a difference frequency of 20 Hz, these time domain data are acquired by averaging 1,000 repetitive scans during a measurement time of 100 s. In Fig. 2.4(b), the THz spectrum obtained by fast Fourier transformation (FFT) of the time-domain data has a frequency resolution of 100 MHz, the inverse of 10 ns. The spectrum has a band of approximately 0.1 ~ 1.5 THz, as can be better seen with the vertical axis on a log scale.

Significant characteristics of this spectrometer are its measurement time, SNR, spectral bandwidth, and spectral resolution. This spectrometer can have a spectral resolution down to 100 MHz, corresponding to the repetition frequency of the fs lasers. In terms of measurement time, SNR, and spectral bandwidth, we tried to find optimal conditions for the difference frequency, a set of parameter for the variable-gain current amplifier, and a sampling rate for the digitizer. When the measurement time was fixed at 100 sec, the set of parameters for the current amplifier was adjusted to keep the virtual spectral bandwidth above 1 THz, and the sampling rate of the digitizer was adjusted to keep a minimum time delay step of 100 fs, we investigated the SNR for various difference frequencies. We define a virtual spectral bandwidth as

$$SB = AB \frac{f_{rl}}{\Delta f}, \quad (2.5)$$

where SB is a virtual spectral bandwidth and AB is the bandwidth of the current amplifier. Fig. 2.5 shows the SNR versus the difference frequency, and the measurement conditions under which the results of Fig. 2.5 are obtained are given in Table 2.1. We obtain the highest SNR at a difference frequency of 10 ~ 20 Hz, as shown in Fig. 2.5. It should be noted that the scan rate is equivalent to half the difference frequency in our measurements. When the digitizer was triggered by a trigger pulse, it acquired data during the entire time interval between the trigger pulse and the next one so that it could not be triggered by the next one. As a result, the dead time amounts to half the measurement time. For example, a scan rate of 10 Hz is obtained at a difference frequency of 20 Hz.

Also, we investigated the relation between the SNR and the measurement time. Fig. 2.6 shows the variation in the SNR with measurement time, which was measured at a difference frequency of 20 Hz. The SNR increases from 9 to 860 as the measurement time increases from 0.1 sec to 1,000 sec. The red line is a fit to the data in the form of $Y = \alpha * X^\beta$, where X is the measurement time and Y is the SNR. When the system noise is limited by the shot noise, the value of β is expected to be close to 0.5. Therefore, the noise level of our system for the ASOPS THz-TDS is confirmed to be close to the shot noise limit.

Using our system for ASOPS THz-TDS, we investigated the THz transmission of water vapor. Fig. 2.7(a) shows a THz transmittance spectrum of water vapor obtained from THz spectra at a relative humidities of 35 and 5% at 21.5°C. Nine absorption lines of water vapor are shown in the frequency range of 0.1 ~ 1.5 THz. The absorption lines were analyzed assuming a Lorentzian line shape, and the central frequencies and the linewidths of the lines are given in Table 2.2. As an instance, Fig. 2.7(b) shows a Lorentz fit of the absorption line 1 at 557.2 GHz. We also confirm that the measured results are in good agreement with previous ones [11].

Table 2.1: Measurement conditions under which the results of Fig. 2.5 were obtained.

Difference frequency (Hz)		1	2	5	10	20	50	100
Measurement time (sec)		100						
# of averaged scans		50	100	250	500	1000	2500	5000
Variable-gain current amplifier	Bandwidth (MHz)	0.22	0.22	0.22	0.22	0.22	1.8	1.8
	Gain (V/A)	10^7	10^7	10^7	10^7	10^7	10^6	10^6
Virtual spectral bandwidth (THz)		22	11	4.4	2.2	1.1	3.6	1.8
Digitizer	Sampling rate (MS/sec)	0.1	0.2	0.5	1	2	5	10
	Vertical resolution (bits)	24	24	24	22	20	20	18
Recording length (minimum time delay step (fs))		 10^5 (100)						

Table 2.2: Absorption lines of water vapor in the frequency range from 0.1 to 1.5 THz.

	Frequency (GHz)	Linewidth (GHz)
1	557.2	7.6
2	752.3	6.8
3	987.9	6.8
4	1097.3	10.1
5	1113.0	5.9
6	1160.9	14.1
7	1207.7	7.7
8	1228.9	4.7
9	1410.2	9.8

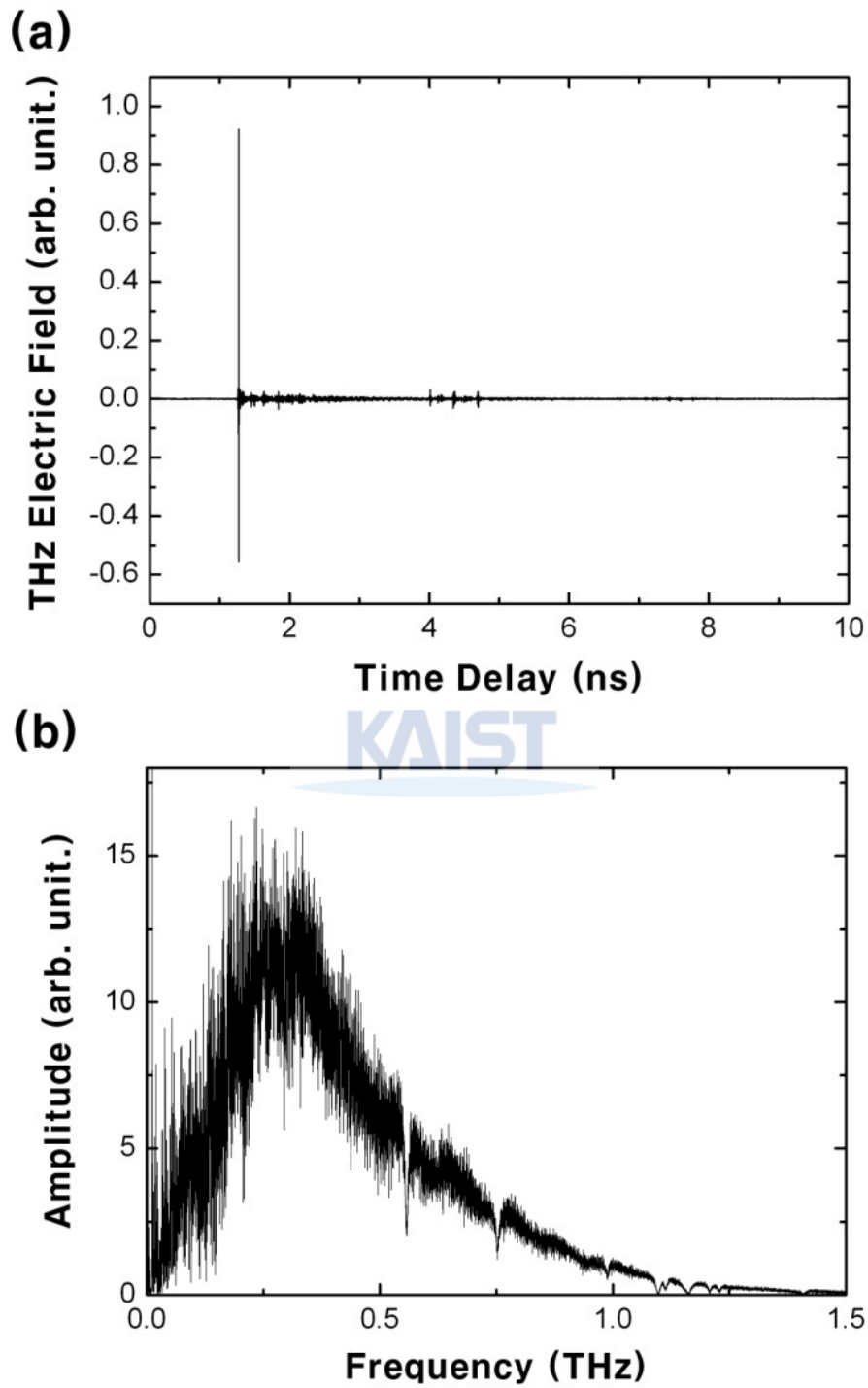


Figure 2.4: (a) A typical time-domain waveform on a 10 ns time window measured from ASOPS THz-TDS. (b) THz spectrum obtained by using a FFT of the time-domain waveform in (a).

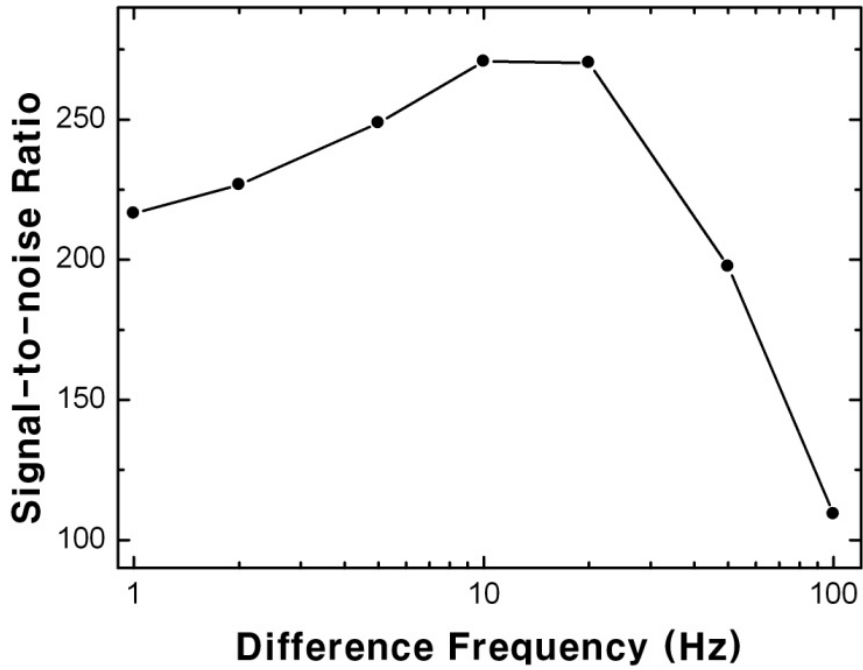


Figure 2.5: SNR versus difference frequency.

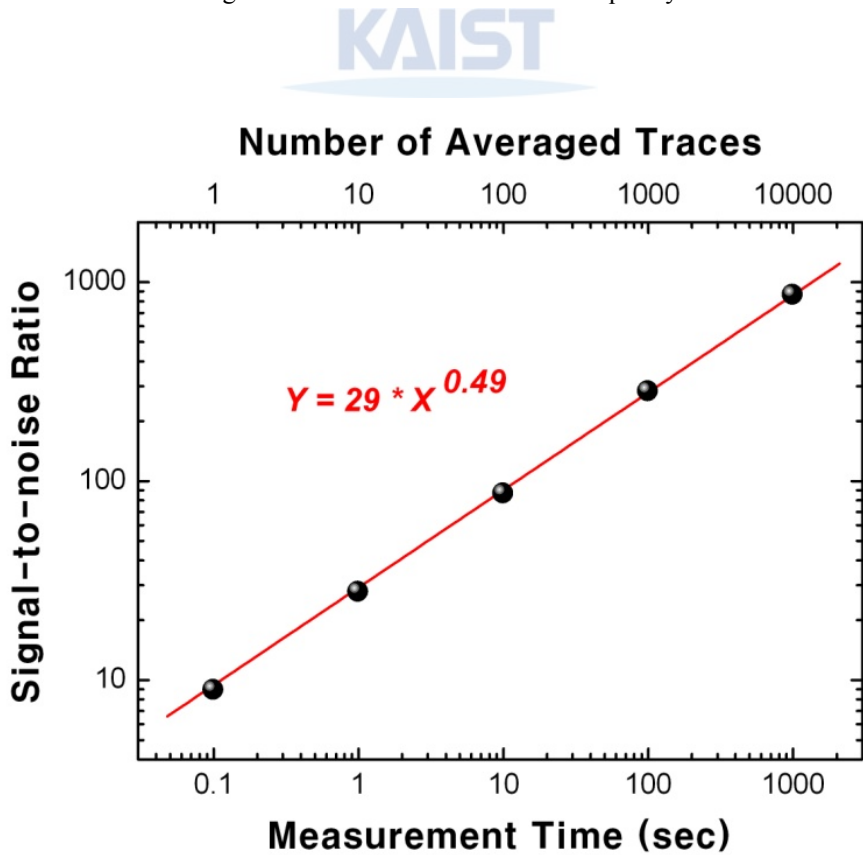


Figure 2.6: SNR versus measurement time. The red line is a fit to the data in the form of $Y = \alpha * X^\beta$.

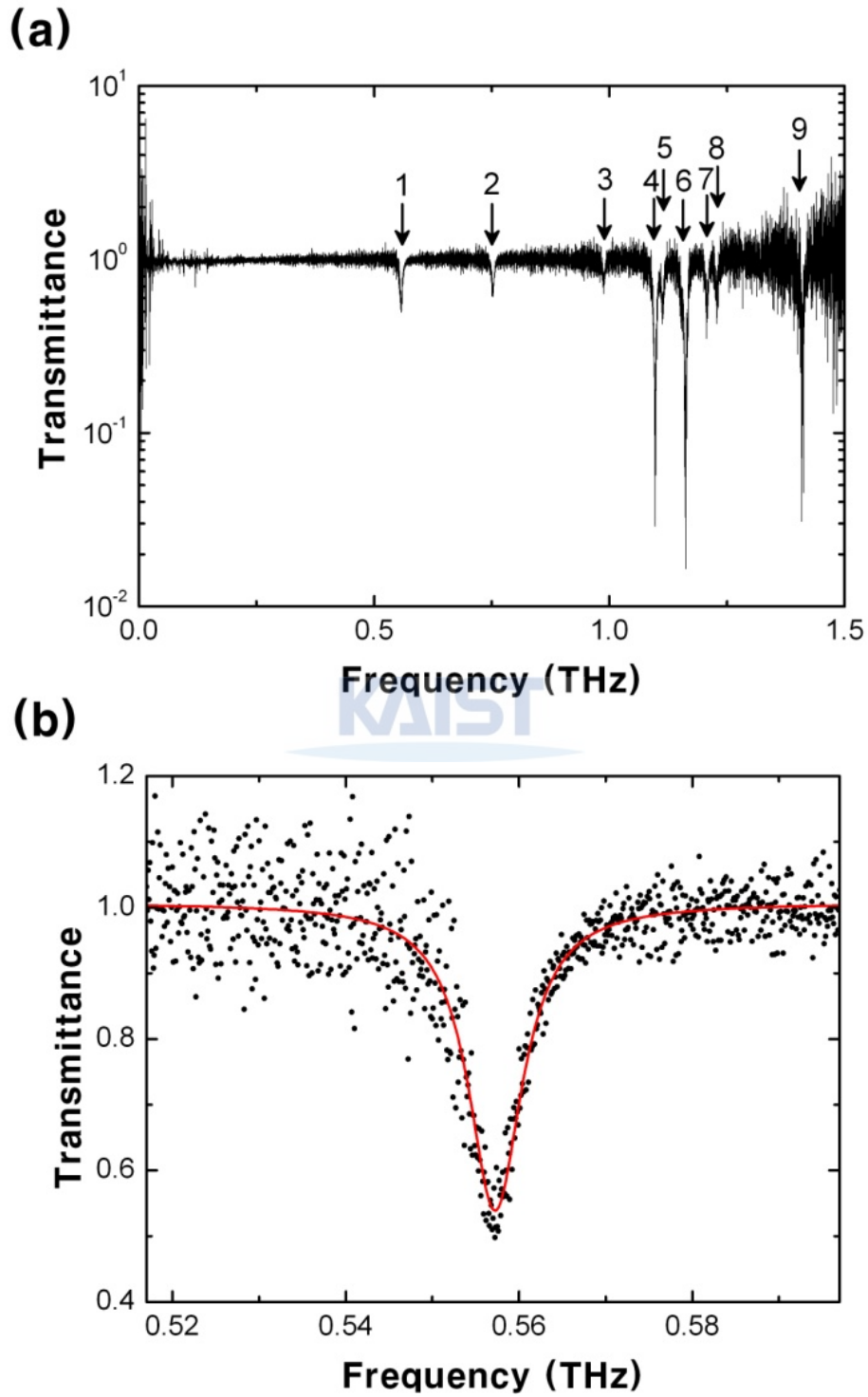


Figure 2.7: (a) THz transmittance spectrum of water vapor. (b) Experimental data (black dot) and its Lorentz fit (red line) with respect to the absorption line 1 of water vapor.

2.4.2 TFCS

In contrast with ASOPS THz-TDS where a time-domain data are measured with a digitizer and a FFT should be performed to obtain a spectrum, we can directly measure the THz spectrum by using a RF spectrum analyzer, instead of a digitizer, in TFCS. A trigger signal for data acquisition, as well as a FFT of a time-domain data, is not needed. A typical THz spectrum obtained from a single sweep is shown in Fig. 2.8(a), which was measured with a resolution bandwidth (RBW) of 20 Hz and a video bandwidth (VBW) of 20 Hz during a measurement time of 907 sec. Because the difference frequency and the number of data points are set to 20 Hz and 15000, respectively, the spectrum has a frequency resolution of 100 MHz. It is almost similar to the spectrum (Fig. 2.4(b)) measured from ASOPS THz-TDS, and the absorption lines of water vapor can be also seen. The SNR of the spectrum is estimated to be 10. In addition, individual comb modes can be clearly resolved in the spectrum.

Fig. 2.8(b) shows a spectrum with a span of 500 MHz at around 0.5 THz, which is obtained by averaging 100 traces for a measurement time of 180 sec with a RBW of 1 Hz and a VBW of 1 Hz. It is shown that the comb modes have frequencies of multiples of the repetition frequency (100 MHz), as described in Eq. (2.3). TFCS will be able to be used for high-accuracy THz frequency metrology. However, it should be noted that ASOPS THz-TDS has an advantage over TFCS in terms of SNR and needs a shorter measurement time than TFCS to attain a specific SNR.

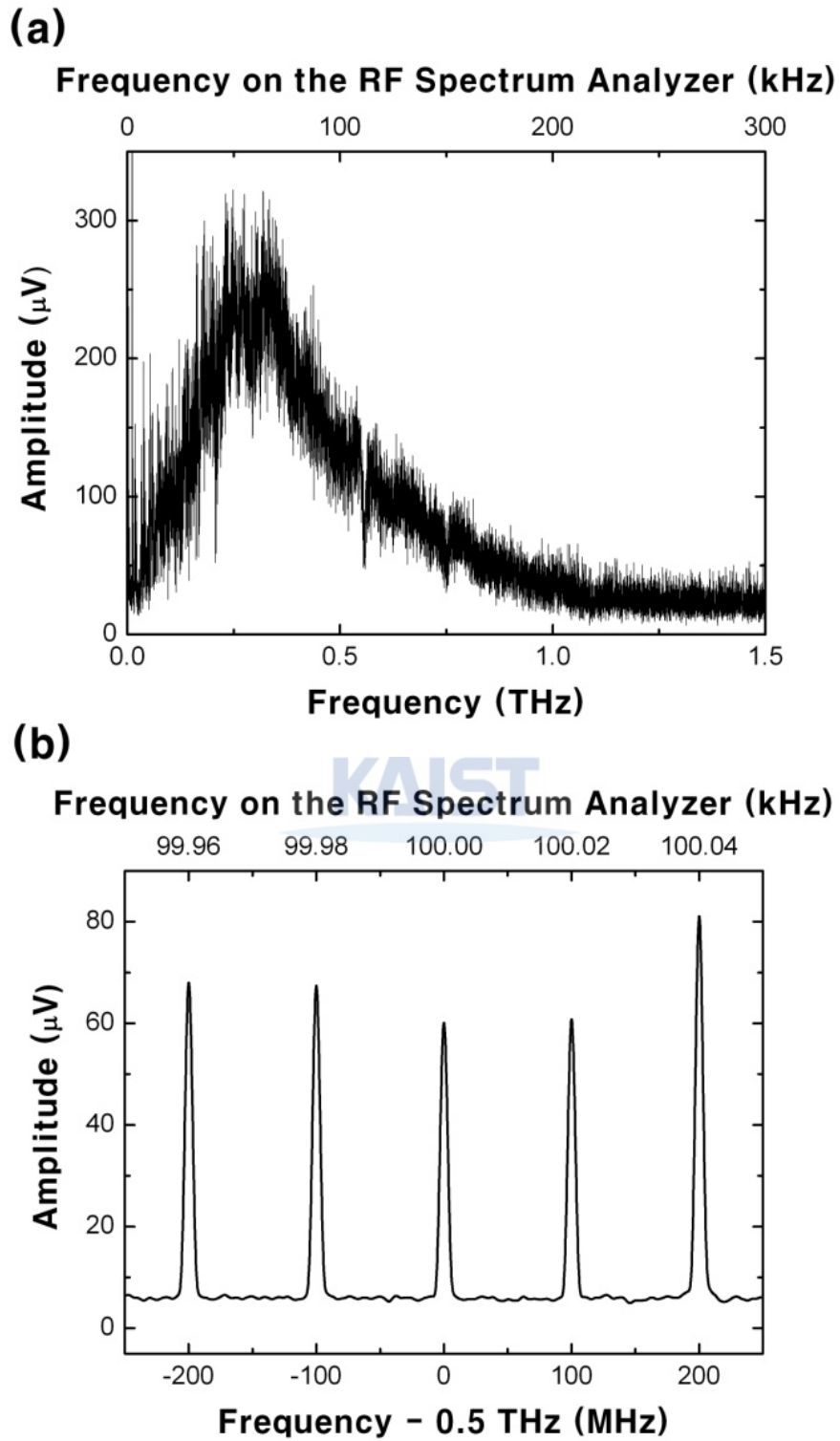


Figure 2.8: (a) Typical spectrum measured from TFCS. (b) THz frequency comb modes are clearly resolved at around 0.5 THz.

2.5 Discussion

We have demonstrated and characterized two types of high-speed high-resolution THz spectrometers. We showed that our system for ASOPS THz-TDS had a time resolution of 257 fs and that its noise level was close to the shot noise limit. The THz transmittance spectrum of water vapor was measured using the ASOPS THz-TDS. Both AOS THz-TDS and TFCS have a frequency resolution of 100 MHz. Although TFCS is simpler experimentally and for data acquisition; ASOPS THz-TDS enables a more rapid measurement. The spectrometers will be able to be widely used as powerful spectroscopic and metrological tools in the THz field.

The logo for KAIST (Korea Advanced Institute of Science and Technology) is centered on the page. It consists of the letters "KAIST" in a bold, blue, sans-serif font. Below the text is a light blue, horizontal, oval-shaped graphic element that tapers at both ends, resembling a stylized shadow or a base.

Chapter 3. Advanced high-speed, high-resolution THz spectroscopy techniques

3.1 Introduction

In this chapter, we demonstrate and discuss the three advanced techniques for high-speed, high resolution THz spectroscopic techniques which are the wavelet power spectrum estimation technique (WPSET), THz frequency-comb multiheterodyne spectroscopy (TFCMS), and electronically controlled optical sampling (ECOPS) THz-TDS.

3.2 Wavelet power spectrum estimation technique

3.2.1 Introduction

ASOPS THz-TDS has recently been demonstrated to overcome the trade-off [16,18]. The ASOPS THz-TDS can serve for high-resolution spectroscopy as well as high-speed monitoring of dynamic processes [27]. It should be noted, however, that an additional noise can significantly appear on high-resolution THz spectra measured in ASOPS THz-TDS. It is caused by a long-lasting tail signal following a main THz pulse in time-domain waveforms. The tail signal is considered to be due to multiple reflections within and between optical components. Since the tail signal causes noise-like fluctuations on the spectrum above the background noise level, signal processing techniques are needed to remove the fluctuations. Signal processing based on wavelets is expected to contribute to enhance a quality of signal without losing information compared to filtering or smoothing. Actually, there have been a few reports in which the wavelet denoising technique is applied to time-domain waveforms from THz-TDS for gas sensing [28], imaging [29,30], and local tomography [31]. We intend to directly apply the wavelet denoising technique to high-resolution THz amplitude spectra to enhance the spectrum quality. Our ASOPS THz-TDS setup with a frequency resolution of 100 MHz is described along with typical experimental results. Then, the WPSET is described for noise reduction in high-resolution THz amplitude spectra measured from ASOPS THz-TDS. A transmission spectrum of water vapor and optical properties of zinc oxide (ZnO) are investigated to verify the performance of the WPSET.

3.2.2 Experiment

Our experimental setup for ASOPS THz-TDS is illustrated in Fig. 3.1. We employ a laser system where two Ti:Sapphire fs lasers are pumped by a diode-pumped solid state laser at 532 nm wavelength. The whole laser system is placed on a temperature-controlled base-plate to reduce thermal fluctuation. The fs laser 1 and 2 have a center wavelength of 800 nm and a pulse duration of 10 and 20 fs, respectively. Two phase-locked loops are used to stabilize the repetition frequencies of the fs lasers. The repetition frequencies of fs laser 1 (f_{r1}) and 2 (f_{r2}) are stabilized at 100 MHz and a variable frequency respectively so that the difference frequency ($\Delta f_r = f_{r1} - f_{r2}$) can be adjusted. By using double-balanced mixers (DBM), the tenth harmonics of f_{r1} and f_{r2} are compared with the outputs of a 1 GHz dielectric resonator oscillator (DRO) and a signal generator (Agilent Technologies N5181A), respectively. The DRO and signal generator share a 10 MHz reference oscillator to reduce the relative timing jitter between the optical pulses from the two fs lasers. The phase error signal output from the DBM is amplified by a proportional-integral amplifier and a high-voltage amplifier and is supplied to a piezoelectric transducer (PZT) to which a cavity mirror is attached. The repetition frequencies are stabilized by controlling the cavity lengths via the PZTs.

Two low-temperature-grown GaAs photoconductive antennas are used for THz emission and detection. The optical pulses from the fs laser 1 are incident on the THz emitter to generate THz pulses, which are guided into the THz detector (DT) by using four off-axis parabolic mirrors. The optical pulses from the fs laser 2 are used to optically sample the THz pulses incident upon the DT. The photocurrent output from the DT represents the magnitude of the electric field of the THz pulses temporally sampled. It is amplified by a variable-gain current amplifier and then is input to a 24-bit flexible resolution digitizer (National Instruments PXI-5922). The digitizer is triggered by a cross-correlation signal generated from a nonlinear optical crystal (2 mm-thick BBO crystal) on which the optical pulses from the two fs lasers are non-collinearly focused. The trigger signal has a repetition frequency equal to the difference frequency. The digitizer acquires time-domain data when triggered by the cross-correlation signal, and we can average over consecutive traces to reduce the noise. The time axis is converted from a real time to a time delay by

$$\tau \text{ (time delay)} = t \text{ (real time)} \times \frac{\Delta f_r}{f_{r1}}. \quad (3.1)$$

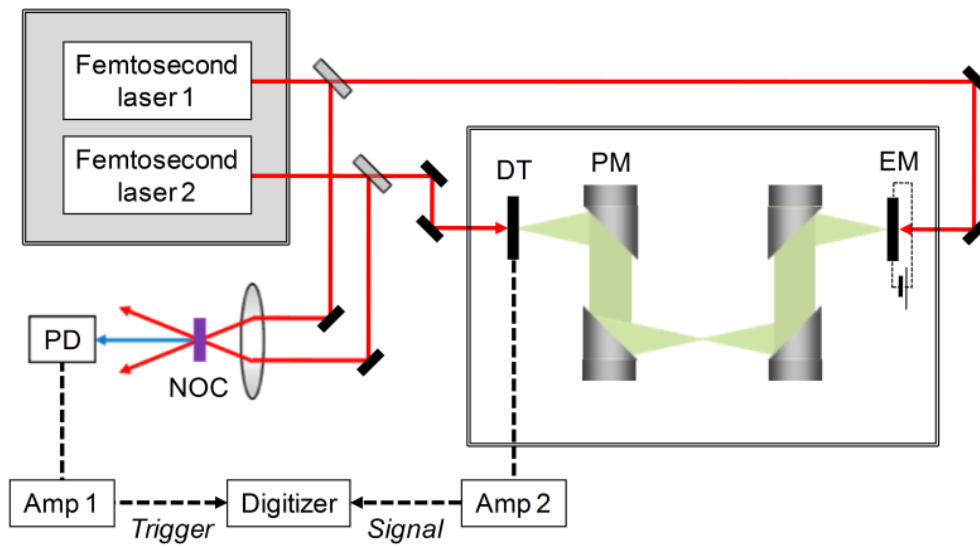


Figure 3.1: Experimental setup for ASOPS THz-TDS. PD: photodetector, EM: THz emitter, DT: THz detector, PM: off-axis parabolic mirror, Amp: variable-gain current amplifier, and NOC: nonlinear optical crystal.

A typical time-domain signal with a 10 ns time delay window measured from the ASOPS THz-TDS is displayed in Fig. 3.2(a). It is acquired by averaging over 1,000 traces during 100 s at a difference frequency of 20 Hz. It can be seen that the tail signal following the main pulse lasts for several nanoseconds. The tail signal is considered to arise from multiple reflections within and between optical components. Fig. 3.2(b) shows a typical THz amplitude spectrum with a frequency resolution of 100 MHz given by the fast Fourier transform (FFT) of the time-domain waveform in Fig. 3.2(a). The long-lasting tail signal leads to the noise-like fluctuations on the spectrum above the background noise level. The fluctuation is not observed in the conventional THz-TDS using an optical delay stage since it has a low spectral resolution due to a much shorter time delay window. The time-domain waveform around the main pulse is displayed on a time delay window of 100 ps in the inset of Fig. 3.2(a). Its spectrum with a frequency resolution of 10 GHz has almost no fluctuation, as shown in the inset of Fig. 3.2(b). Hence, a signal processing technique is needed to remove the fluctuation on high-resolution THz amplitude spectra measured from the ASOPS THz-TDS.

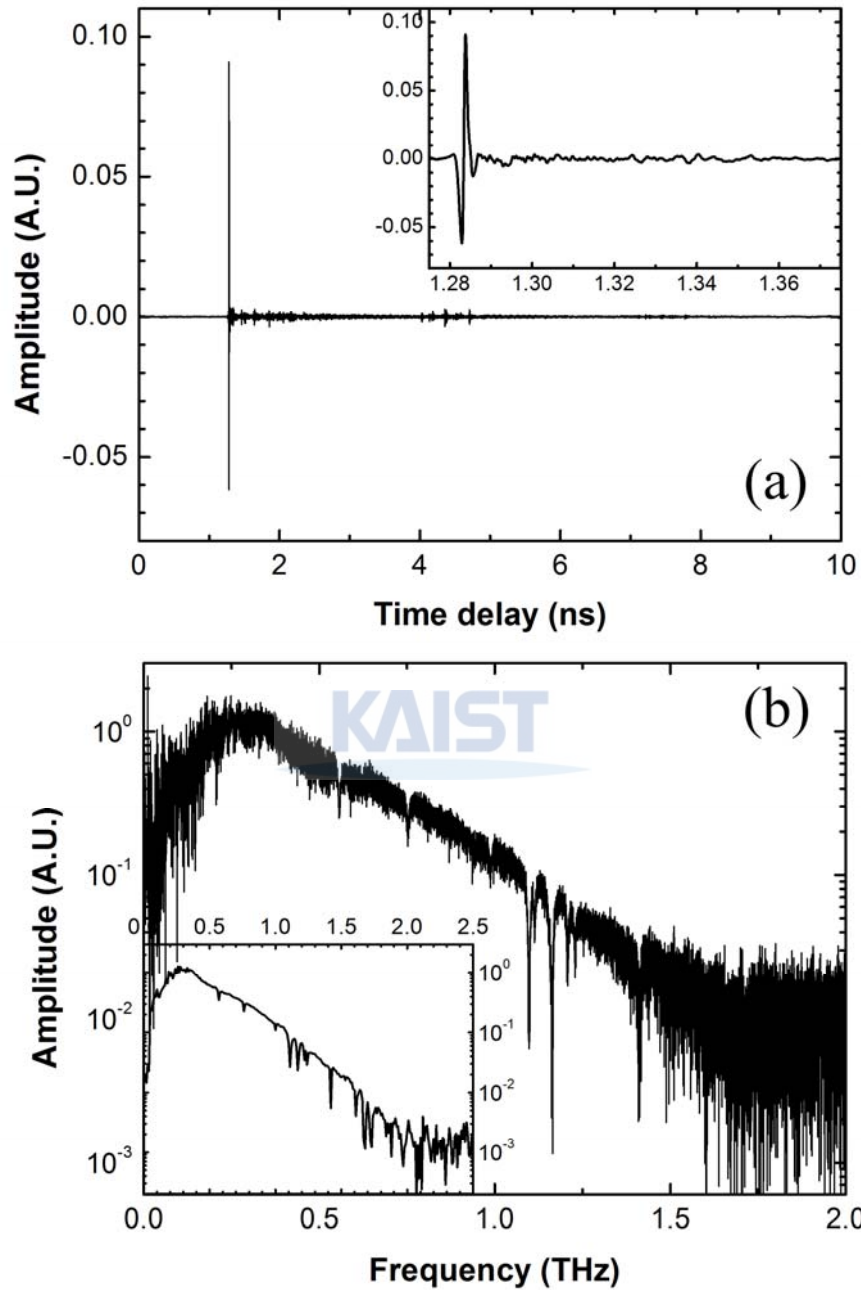


Figure 3.2: (a) Typical time-domain waveform on a 10 ns time delay window measured from ASOPS THz-TDS at relative humidity of 28 %. (b) THz amplitude spectrum obtained by FFT of the time-domain waveform in (a).

3.2.3 Theoretical description of the WPSET

Wavelet based signal processing appears a natural choice for denoising THz pulses since wavelet analysis is good for capturing singularities both in the time and frequency domains [32]. Signals can be analyzed by wavelet transform using a set of basis shifted and dilated from a mother wavelet $\psi(t)$, defined as

$$\left\{ \psi_{j,n}(t) = \frac{1}{\sqrt{2^j}} \psi\left(\frac{t-2^j n}{2^j}\right) \right\}_{(j,n) \in \mathbb{Z}^2}, \quad (3.2)$$

where j and n mean the scale and location indices, respectively, and \mathbb{Z} is the set of integers. A wavelet basis is an orthogonal basis of $L^2(\mathbb{R})$, where \mathbb{R} is the set of real numbers and $L^2(\mathbb{R})$ corresponds to the Hilbert space for functions $f(t)$ with finite energy such that $\int |f(t)|^2 dt < +\infty$ [32]. In $L^2(\mathbb{R})$, the inner

product $\langle f, g \rangle$ is defined as $\langle f, g \rangle = \int f(t)g(t)dt$. It is known that any signal $f(t) \in L^2(\mathbb{R})$ can be represented as

$$f = \sum_{j=-\infty}^{\infty} \sum_{n=-\infty}^{\infty} \langle f, \psi_{j,n} \rangle \psi_{j,n}. \quad (3.3)$$

By introducing a scaling function ϕ , we can also represent Eq. (3.3) as

$$f = \sum_{j=-\infty}^J \sum_{n=-\infty}^{\infty} \langle f, \psi_{j,n} \rangle \psi_{j,n} + \sum_{n=-\infty}^{\infty} \langle f, \phi_{J,n} \rangle \phi_{J,n}, \quad (3.4)$$

where the scaling function ϕ can be readily derived from a mother wavelet ψ and J is the maximum scale index for dilation. Then, the approximation coefficients $\{a_j[n]\}_{j,n}$ and detail coefficients $\{d_j[n]\}_{j,n}$ are defined by

$$a_j[n] = \langle f, \phi_{j,n} \rangle, \quad d_j[n] = \langle f, \psi_{j,n} \rangle. \quad (3.5)$$

Similarly, the discrete signal $\{f[n]\}_{0 \leq n < N}$ can be represented as

$$f = \sum_{j=0}^J \sum_{n=0}^{N-1} \langle f, \psi_{j,n} \rangle \psi_{j,n} + \sum_{n=0}^{N-1} \langle f, \phi_{J,n} \rangle \phi_{J,n}, \quad (3.6)$$

where $\{\phi_{j,n}\}_{0 \leq n < N}$ and $\{\psi_{j,n}\}_{0 \leq n < N}$ denote the discrete scaling and wavelet functions at scale j , respectively. In wavelet denoising, the approximation and detail coefficients are processed using a shrinkage operator $\rho_T(\cdot)$:

$$\tilde{f} = \sum_{j=0}^J \sum_{n=0}^{N-1} \rho_T(d_j[n]) \psi_{j,n} + \sum_{n=0}^{N-1} \rho_T(a_J[n]) \phi_{J,n} \quad (3.7)$$

Many different types of shrinkage operator $\rho_T(\cdot)$ have been proposed depending on applications. For

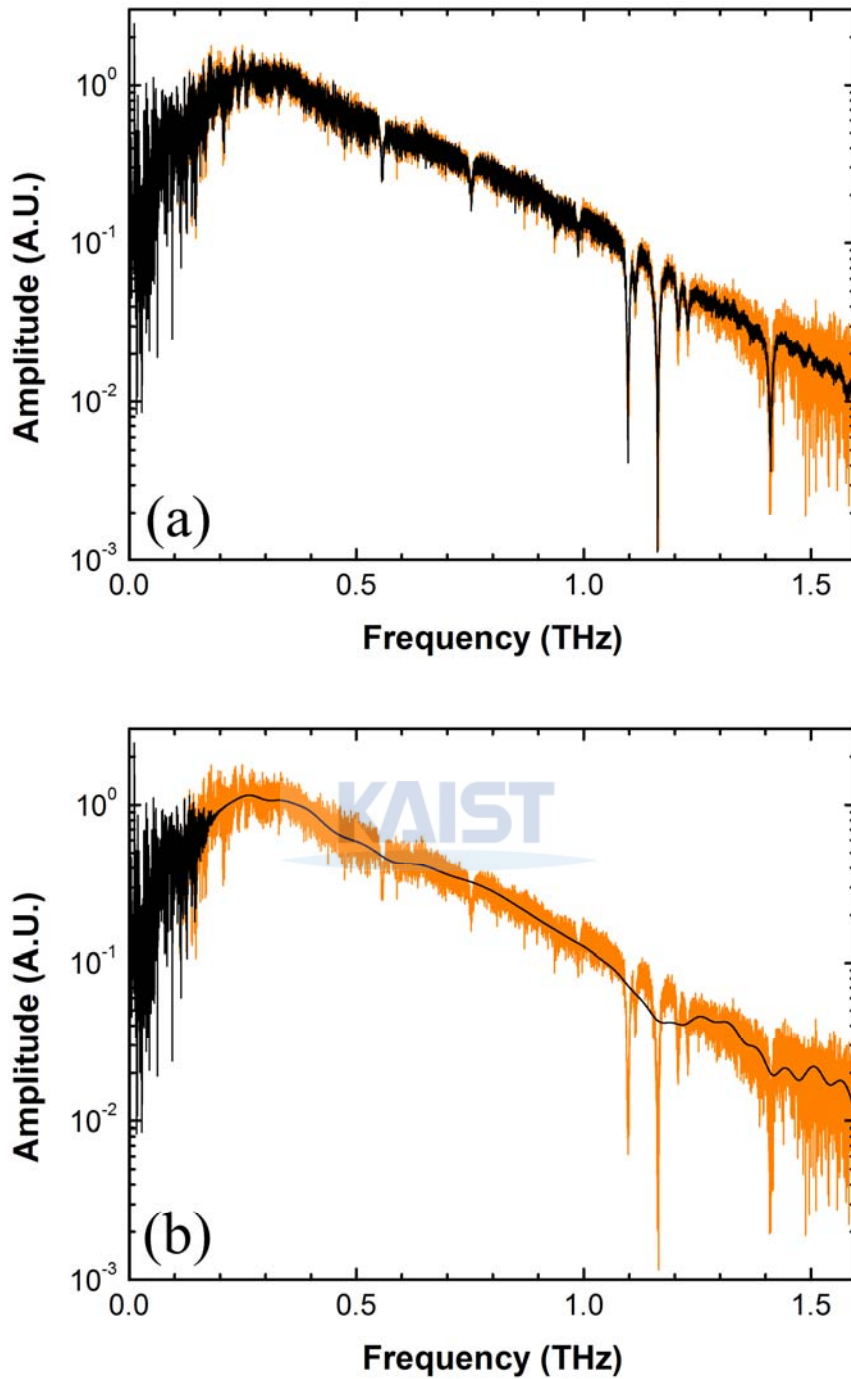


Figure 3.3: THz amplitude spectra of wavelet-denoised time-domain waveforms. The orange lines show the raw spectrum in Fig. 3.2(b) and the black lines the spectra of the time-domain waveforms that are denoised using the Daubechies wavelet with 10 vanishing moments at the scale of 5 for a low (a) and high (b) threshold value, respectively. The low threshold can scarcely remove the fluctuation, whereas the high threshold distorts the singularities.

example, the hard-thresholding defined as

$$\rho_T(x) = \begin{cases} x, & |x| \geq T; \\ 0, & \text{otherwise} \end{cases} \quad (3.8)$$

is one of popular methods for denoising. Not that an appropriate choice of wavelet is especially important in wavelet analysis. A mother wavelet is usually designed to have appropriate vanishing moments, support size, symmetry, regularity, and etc. Specifically, a wavelet ψ is said to have p vanishing moments if

$$\int_{-\infty}^{\infty} t^k \psi(t) dt = 0, \quad 0 \leq k < p. \quad (3.9)$$

This implies that the corresponding detail coefficient $\{d_j[n]\}_{j,n}$ is zero if a signal can be approximated with polynomials up to order $p-1$. Hence, the vanishing moment determines the decay rate of the wavelet coefficients, which is one of the important factors in determining the denoising performance. The support of the wavelet – the nonzero span of mother wavelet – is another important factor to consider. A wavelet with smaller support is better in capturing singularities or peak values. However, a wavelet with smaller support usually tends to have fewer vanishing moments and thus exhibits a lower decay rate. In order to have p vanishing moments, the support size of the mother wavelet ψ should be at least $2p-1$. Therefore, there exists a fundamental tradeoff between capability of capturing singularities and denoising performance. It is now known that the Daubechies wavelet has the maximum vanishing moment for a given support size.

A time-domain waveform from conventional THz-TDS can be directly processed using a wavelet denoising algorithm. For example, Mittleman et al. demonstrated that the noises in THz time-domain signals can be effectively suppressed by appropriate choice of wavelets [28]. Ferguson et al. further demonstrated the T-ray images are also greatly improved by wavelet denoising followed by Wiener deconvolution [29]. However, the time-domain wavelet denoising cannot effectively remove the fluctuation on a spectrum with keeping spectral information since the fluctuation does not come from noises, rather from the long-lasting signal of the time-domain waveform. Fig. 3.3 shows results of the time-domain wavelet denoising where the Daubechies wavelet with 10 vanishing moments was used at the scale of 5. For a low threshold value, the fluctuation is hardly reduced even though the spectral features remain unchanged, as shown in Fig. 3.3(a). On the contrary, a high threshold value results in distortion at the singularities as well as reduction of the fluctuation, as shown in Fig. 3.3(b).

Therefore, we employ a direct power spectrum estimation technique to denoise the spectrum [33]. Here, the estimation problem of the power spectrum of THz-TDS data is regarded as a nonparametric statistical estimation problem of a stationary random process. More specifically, time-domain data $x[n]$ is assumed as a real wide-stationary Gaussian random process with zero mean and covariance

$R_x[n] = E[x[m]x[m+n]]$, where the $E[\cdot]$ is the expectation of an inside parameter. The periodogram of $x[n]$ is then described by

$$I_N(\nu) = \left| \sum_{n=0}^{2N-1} x[n] e^{-i2\pi n\nu} \right|^2, \quad -\frac{1}{2} < \nu \leq \frac{1}{2}. \quad (3.10)$$

The periodogram is often used as an estimate of the power spectrum $S(\nu)$, which is defined as

$$S(\nu) = \sum_{n=-\infty}^{\infty} R_x[n] e^{-i2\pi n\nu}, \quad -\frac{1}{2} < \nu \leq \frac{1}{2}. \quad (3.11)$$

If $S(\cdot)$ is sufficiently smooth and N is large enough, the periodogram and power spectrum satisfy the following asymptotic relation [33]:

$$\ln I_N\left(\frac{k}{2N}\right) - \gamma = \ln S\left(\frac{k}{2N}\right) + \varepsilon(k), \quad k = 0, 1, \dots, N \quad (3.12)$$

where $\gamma \approx 0.5772$ denotes the Euler-Mascheroni constant, and $\{\varepsilon(k) : k = 0, \dots, N\}$ are independent and identically distributed (i.i.d.) with zero mean and variance of $\pi^2/6$. It is known that the periodogram is asymptotically unbiased [32]. Hence, the periodogram is quite often used as an estimate of the power spectrum. In wavelet power spectrum estimation, the wavelet transform is directly applied to the log periodogram in Eq.

(3.12). The resultant approximation and detailed coefficients are then given by

$$\begin{aligned} a_j[n] &= \langle \ln I_N - \gamma, \phi_{j,n} \rangle \\ d_j[n] &= \langle \ln I_N - \gamma, \psi_{j,n} \rangle = \langle \ln I_N, \psi_{j,n} \rangle \end{aligned} \quad (3.13)$$

where $\{\phi_{j,n}\}_{0 \leq n < N}$ and $\{\psi_{j,n}\}_{0 \leq n < N}$ denote the discrete scaling and wavelet functions at scale j , respectively, and the last equality in Eq. (3.13) comes from the vanishing moment condition of Eq. (3.9). Similarly, we can define the detailed coefficients for $\ln S(\cdot)$ and $\varepsilon(\cdot)$:

$$\begin{aligned} d_j^S[n] &= \langle \ln S, \psi_{j,n} \rangle \\ d_j^\varepsilon[n] &= \langle \varepsilon, \psi_{j,n} \rangle \end{aligned} \quad (3.14)$$

Hence, Eq. (3.12) can be equivalently transformed into

$$d_j[n] = d_j^S[n] + d_j^\varepsilon[n]. \quad (3.15)$$

If $\max_\nu |\psi(\nu)| = M < \infty$, then the probability density function of $d_j^\varepsilon[\cdot]$ converges to the Gaussian probability density function as N grows. Since N is sufficiently large in high-resolution THz-TDS, the model Eq. (3.15) is accurate and the noise has an i.i.d. Gaussian distribution with zero mean [33]. Under this condition, the result of wavelet denoising is a nearly minimax optimal estimate of the underlying true log power spectrum [34], and the estimate can be represented by

$$\ln S = \sum_{j=0}^J \sum_{n=0}^{N-1} \rho_T \left(\langle \ln I_N, \psi_{j,n} \rangle \right) \psi_{j,n} + \sum_{n=0}^{N-1} \rho_T \left(\langle \ln I_N - \gamma, \phi_{J,n} \rangle \right) \phi_{J,n} \quad (3.16)$$

where the shrinkage operator ρ_r is given by Eq. (3.8).

3.2.4 Spectrum denoising by the WPSET

We denoised the THz amplitude spectrum in Fig. 3.2(b) using the WPSET as described above. It is presented in Fig. 3.4 that the WPSET can effectively remove the fluctuations above the background noise level on the THz amplitude spectrum without altering the water vapor absorption lines. The Daubechies wavelet with 10 vanishing moments was used at the scale of 5. To find optimal parameters for wavelet power spectrum estimation, we compared the spectra denoised with different choices of the wavelet and scale. Fig. 3.5 shows magnified views around 1.16 THz of the raw spectrum and denoised spectra. The Haar wavelet overestimated the noise at 1.1645 GHz as a real singularity, as shown in Fig. 3.5(b). The Daubechies wavelet offers the minimum support for a given number of vanishing moments [29], which means that it is an optimal wavelet for denoising and detecting singularities simultaneously. Fig. 3.5(c) and (d) show the spectra that were denoised using the Daubechies wavelet with 10 vanishing moments at the scale of 4 and 5, respectively. It is apparently shown that the spectrum is more effectively denoised at the scale of 5, compared to the scale of 4. We also observed that the scales over 6 caused distortion at singularities (not shown here). Therefore, we chose the Daubechies wavelet with 10 vanishing moments and the scale of 5 for the following studies.

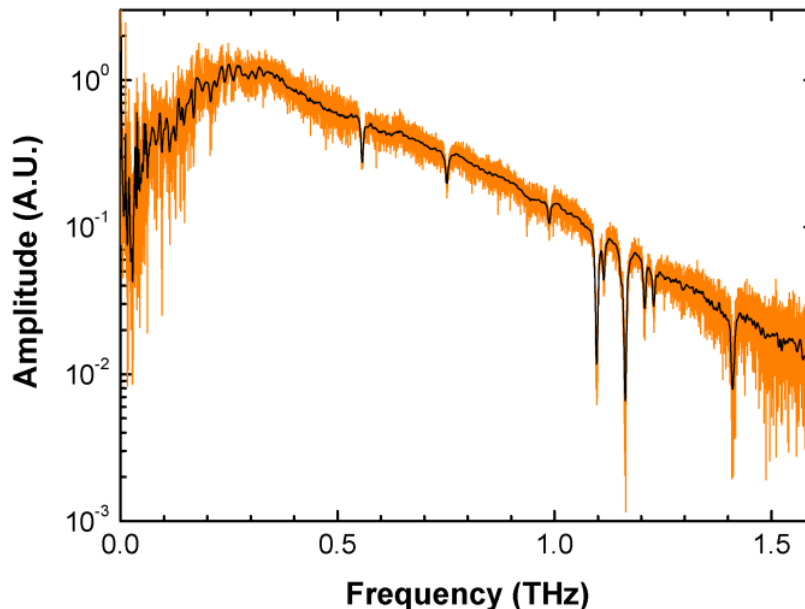


Figure 3.4: THz amplitude spectrum denoised by using the WPSET. The orange and black lines display the raw and denoised spectra, respectively.

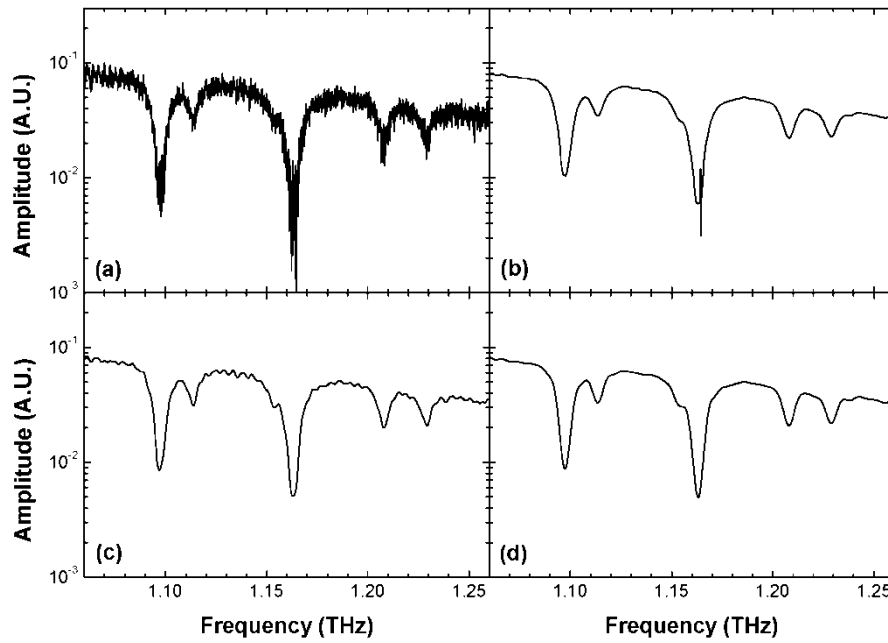


Figure 3.5: Magnified views at around 1.16 THz of the raw spectrum (a) and the spectra denoised using the Haar wavelet at the scale of 5 (b), the Daubechies wavelet with 10 vanishing moments at the scale of 4 (c), and the Daubechies wavelet with 10 vanishing moments at the scale of 5, respectively.

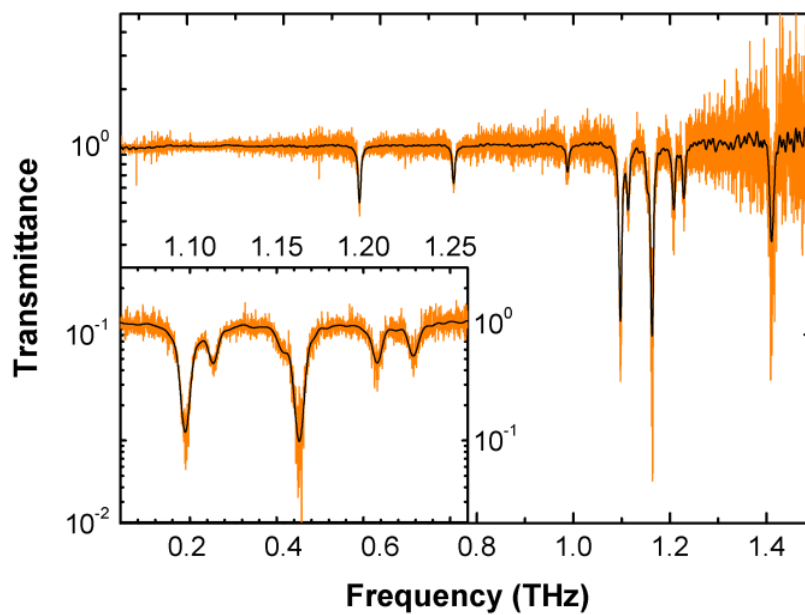


Figure 3.6: THz transmission spectra of water vapor resulting from the raw (orange line) and denoised (black line) amplitude spectra. The inset is an enlarged view around 1.16 THz.

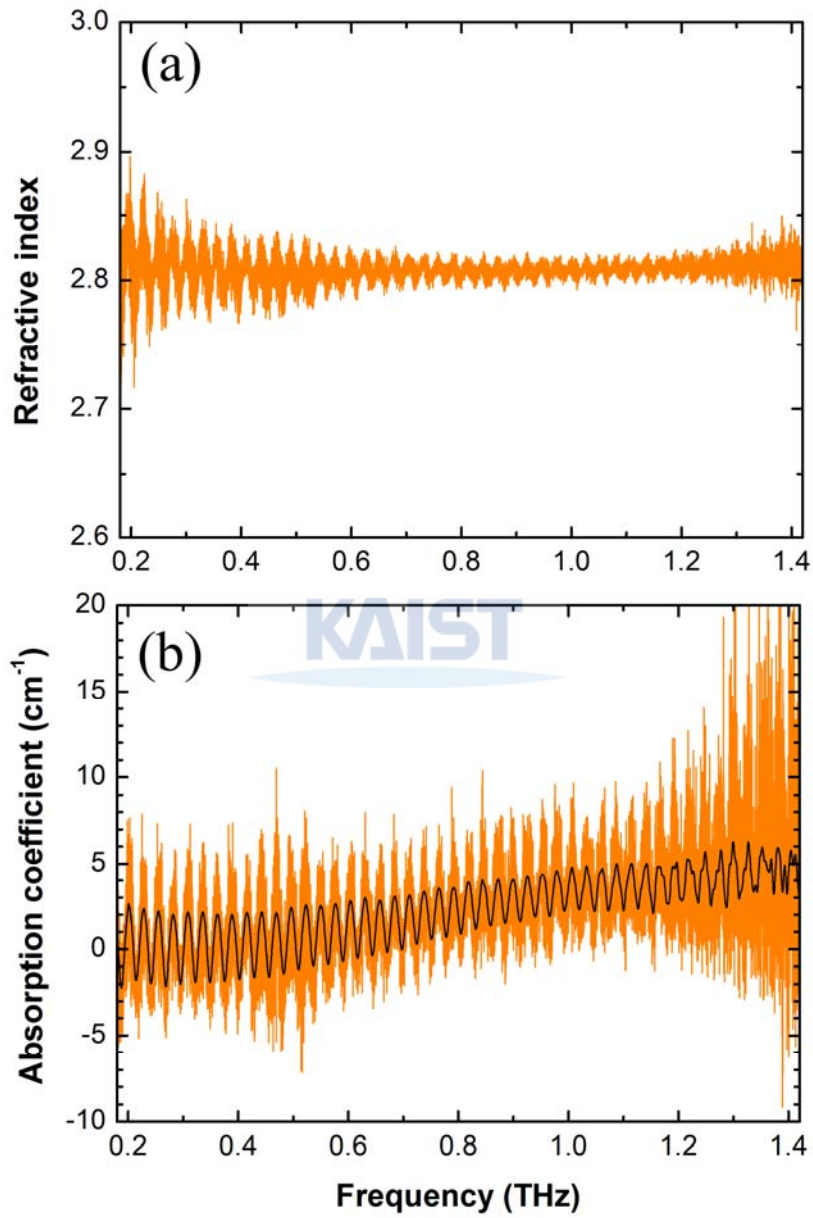


Figure 3.7: Frequency-dependent refractive index (a) and absorption coefficient (b) of ZnO. The raw and de-noised results are indicated by the orange and black lines, respectively.

Table 3.1: Center frequencies, linewidths, and transmittances of the absorption lines extracted from the raw and denoised transmission spectra of water vapor.

	Center frequency (GHz)			Linewidth (GHz)			Transmittance		
	Raw spectrum	Error	Denoised spectrum	Raw spectrum	Error	Denoised spectrum	Raw spectrum	Error	Denoised spectrum
1	557.09	0.09	557.08	7.99	0.28	8.06	0.4879	0.0353	0.4905
2	752.17	0.11	752.16	7.11	0.36	7.22	0.6183	0.0382	0.6220
3	988.00	0.26	987.96	7.87	0.85	7.74	0.7221	0.0644	0.7251
4	1097.30	0.12	1097.30	10.64	0.39	10.52	0.1241	0.0676	0.1178
5	1113.65	0.18	1113.64	7.85	0.60	7.75	0.5495	0.0746	0.5492
6	1152.78	0.44	1152.79	7.00	1.51	6.73	0.7971	0.1129	0.8078
7	1162.98	0.16	1162.98	11.08	0.50	10.85	0.1190	0.0891	0.0988
8	1207.71	0.16	1207.72	8.28	0.51	8.19	0.4884	0.0661	0.4806
9	1228.74	0.17	1228.76	7.39	0.53	7.47	0.5390	0.0697	0.5367
10	1410.98	0.49	1410.99	11.13	1.61	10.98	0.2761	0.2529	0.2617

To verify the performance of the WPSET, we investigated a THz transmission spectrum of water vapor. A THz transmission spectrum of water vapor was obtained from THz amplitude spectra measured at relative humidity of 28 % and 2 % and at 21.5 °C. Fig. 3.6 shows the transmission spectra of water vapor before and after applying the WPSET with the optimized parameters, which are indicated by the orange and black lines, respectively. It is clearly demonstrated that the WPSET can effectively remove the fluctuations without distortion in the water vapor absorption lines. We extracted the center frequencies, linewidths, and transmittances of the 10 strongest absorption lines from the raw and denoised transmission spectra over the frequency range up to 1.5 THz by fitting them to Lorentzian line shapes. Table 3.1 lists them along with the error values of the fitting results from the raw spectrum. The fitting results from the raw spectrum are in good agreement with those from the denoised spectrum within the error values.

We also investigated optical properties of ZnO. A both-side polished 2 mm-thick ZnO single crystal with an orientation of <0001> was measured using ASOPS THz-TDS. The refractive index $n(\omega)$ and absorption coefficient $\alpha(\omega)$ of ZnO are simply given by

$$n(\omega) = \frac{c_0 \varphi(\omega)}{\omega d} + 1, \quad (3.17)$$

$$\alpha(\omega) = \frac{2}{d} \ln \left(\frac{4n(\omega)}{T(\omega) \cdot (n(\omega) + 1)^2} \right), \quad (3.18)$$

where ω is the angular frequency, c_0 is the velocity of light in vacuum, d is the thickness of the ZnO crystal, φ is the phase difference between the sample and reference waveforms, and T is the transmittance that can be denoised by use of the WPSET [35]. Fig. 3.7 shows the frequency-dependent refractive index and absorption coefficient of ZnO. There exists the periodic ripple in the results due to multiple reflections within the ZnO crystal. The orange and black lines represent raw and denoised results, respectively. The refractive index is obtained from the raw phase spectrum, and it cannot be denoised since, to our knowledge, no denoising technique for a phase spectrum has yet been reported. Nevertheless, the fluctuations in the absorption coefficient can be considerably reduced by denoising the amplitude spectrum only, as shown in Fig. 3.7(b). This result shows that the WPSET can effectively denoise an absorption coefficient spectrum measured from high-resolution THz-TDS.

3.3 Terahertz frequency-comb multiheterodyne spectroscopy

3.3.1. Introduction



Fourier-transform (FT) spectroscopy is widely used for characterization and identification of molecules particularly in the infrared (IR) range that is abundant in molecular fingerprints [36]. High frequency resolution would allow for precise frequency measurements on molecular characteristics. Basically, one source and an interferometer are used to measure an interferogram in FT spectroscopy, where a moving mirror on one arm of the interferometer scans a time delay. In analogy with THz-TDS, the moving distance of the mirror determines a time delay window whose inverse equals a frequency resolution. Thus, there exists a fundamental tradeoff between a frequency resolution and a measurement time.

Spectrometry using two frequency combs (FCs) with slightly different mode spacing was proposed, which has the advantages of rapid data acquisition and high frequency resolution [37]. Subsequently, coherent multiheterodyne spectroscopy using frequency combs was implemented in the mid-IR range, where two mid-IR FCs with thermally stabilized different repetition frequencies were used to scan a time delay without an optical delay stage [38]. They showed rapid transient spectroscopy of non-repetitive phenomena using the FC FT spectroscopy [39]. Also, near-IR multiheterodyne spectroscopy was demonstrated using actively stabilized FCs [40]. They achieved a high frequency resolution and accuracy thanks to actively stabilized FCs. Earlier, subterahertz spectroscopy using a dual-source interferometer was demonstrated by employing electronic mi-

crowave and millimeter wave techniques [41].

3.3.2. Principles of operation

A harmonic THz FC can be produced from an optical FC emitted by a mode-locked fs Ti:Sapphire laser through the well-known methods such as the photoconduction and optical rectification [42]. In the frequency domain, two harmonic THz FCs with slightly different mode spacings are represented as

$$\begin{aligned} n f_{r1} (n=1,2,3,\dots) \\ n f_{r2} (n=1,2,3,\dots) \end{aligned} \quad (3.19)$$

where f_{r1} and f_{r2} are respective repetition frequencies, as illustrated in Fig 3.8. Superposition of the two harmonic FCs is used in the multiheterodyne spectroscopy. When the two FCs superposed by a beam combiner are detected, the multiheterodyne beat of the two FCs results in a detector signal at harmonic beat frequencies $n\Delta f_r (n=1,2,3,\dots)$, where $\Delta f_r = f_{r1} - f_{r2}$. Then, the beat FC is approximately a replica of the THz-FC, frequency-downscaled by the factor of $\Delta f_r / f_{r1}$ [39].

In the time domain, the two THz-FCs are periodic THz wave pulses repeating at f_{r1} and f_{r2} , respectively, as shown in Fig. 3.8. The relative time delay between the two THz pulses varies continuously owing to the difference in repetition frequencies, whereas the conventional FT spectroscopy utilizes a mechanical delay method to scan the time delay. Consequently, the beats of the two THz pulses result in interferograms repeating at Δf_r , usually in the radio-frequency (RF) region. The THz-FC spectrum can be obtained by recording the time-domain signal, namely the interferogram, Fourier-transforming the interferogram to obtain the RF beat spectrum, and scaling the beat frequency by $f_{r1} / \Delta f_r$ [39].

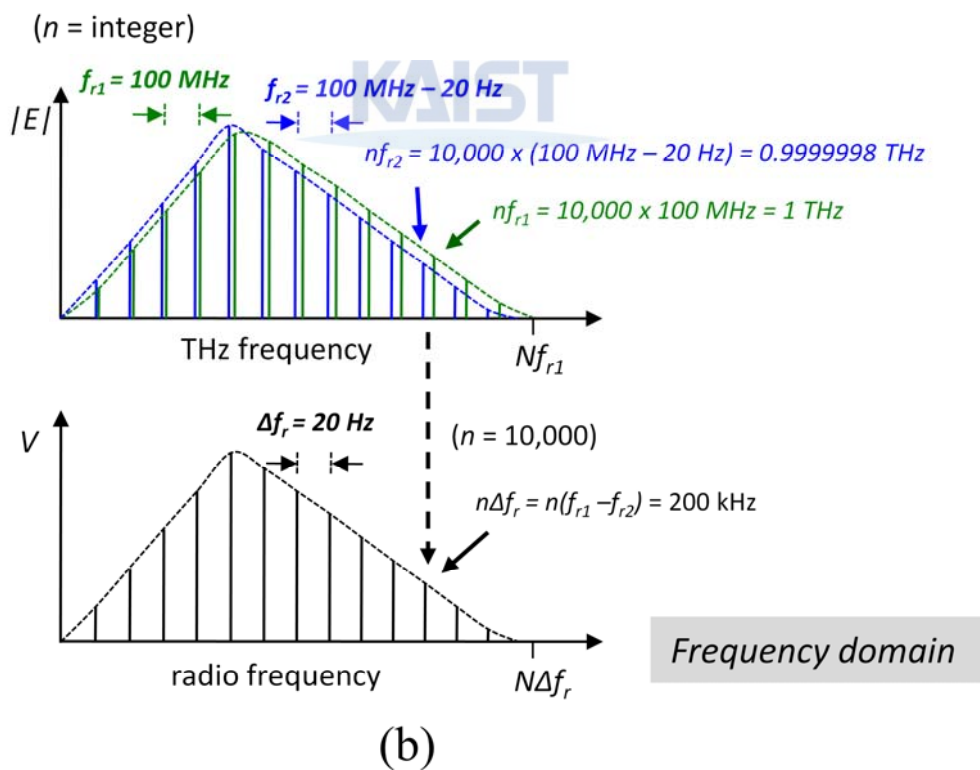
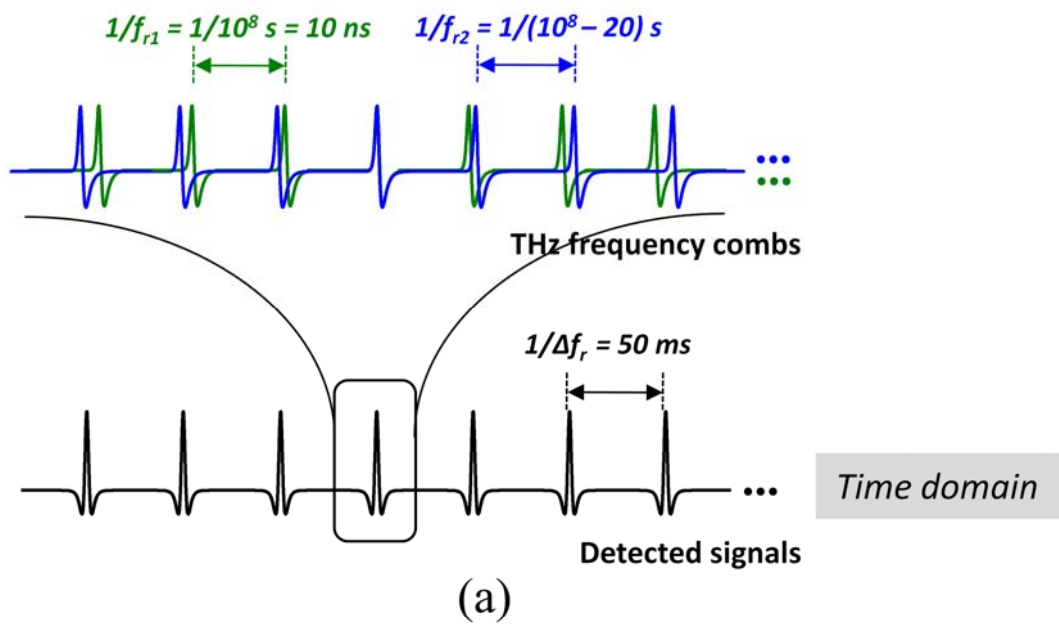


Figure 3.8: Illustration of the principles of the TFCMS in (a) the time domain and (b) the frequency domain.

3.3.3. Experiment

We developed an experimental setup for multiheterodyne spectroscopy using stabilized THz-FCs. Fig. 3.9 shows a schematic diagram for the experimental setup. We employ a laser system comprising two 100 MHz Ti:Sapphire fs lasers (FEMTOLASERS, TWIN SYNERGY) and two phase-locked loops (PLLs) (MenloSystems) for active stabilization of the respective repetition frequencies of the fs lasers. A continuous-wave optical beam with a wavelength of 532 nm and an optical power of 8.2 W that is output by a pump laser is split into two beams of 4.1 W to pump the fs lasers, respectively. The fs lasers emit optical pulse trains with a central wavelength of 800 nm and an average optical power of about 600 mW. The optical pulses from the fs laser 1 and 2 have pulse durations of 10 and 20 fs, respectively. All the optical parts are placed on a temperature-controlled base plate in one box to reduce the thermal fluctuation and expansion.

Two THz pulse trains are generated from two photoconductive antennas (PCAs) (EKSPLA) illuminated by the two optical pulse trains from the fs lasers, respectively. They are THz-FCs composed of a number of THz modes at harmonics of the repetition frequencies [42]. The THz-FCs emitted from the PCAs are collimated by off-axis parabolic mirrors and are combined by a THz beam combiner that is a 2 μm -thick nitrocellulose film with a metallic coating (RadiaBeam Technologies). It provides $\sim 25\%$ reflection and $\sim 25\%$ transmission over a wide frequency range. The combined THz-FC is guided by another off-axis parabolic mirror to a cryogenic bolometer (QMC Instruments, QFI/0BI) operating at 4.2 K, followed by a preamplifier with a 3-dB bandwidth of 1 MHz. A low-pass filter installed in front of the bolometer in a liquid helium bath cryostat blocks electromagnetic waves at frequencies above 3 THz. Also, an optical sum-frequency signal at a wavelength around 400 nm is generated in a nonlinear optical crystal (a 2 mm-thick BBO crystal) on which the two optical beams from the fs lasers are non-collinearly focused, and is detected by a 12.5 MHz photodetector (PD 3), as the cross-correlator shows in Fig. 3.9. The cross-correlation signal from the PD 3 is electrical pulses repeating at Δf_r . A 24-bit flexible resolution digitizer (National Instruments, PXI-5922) acquires an interferogram from the signal detected by the bolometer, when triggered by the cross-correlation signal. The sampling rate of the digitizer is varied with Δf_r such that the time delay step is 100 fs, given by

$$\Delta\tau_s = \frac{\Delta f_r}{R_s f_{r1}} \quad (3.20)$$

where $\Delta\tau_s$ is the time delay step and R_s is the sampling rate of the digitizer. The real time on the time axis of an interferogram is converted to the time delay by the scaling factor $\Delta f_r / f_{r1}$. The time delay between the THz-FCs is repetitively scanned at Δf_r , and the maximum time delay window of 10 ns can be obtained, corresponding to the pulse-to-pulse time interval. We can average over successive interferogram traces for noise

reduction.

To enhance the frequency accuracy and resolution, we stabilize the repetition frequencies of the fs lasers. A portion of the optical beam from the fs laser 1 is split off to be detected by a 1 GHz photodetector (PD 1). In the PLL 1, the tenth harmonic signal at 1 GHz from the PD 1 is compared with a 1 GHz reference signal from a dielectric resonator oscillator (DRO), and the phase error is fed back to the piezoelectric transducer, to which a cavity mirror in the fs laser 1 is attached, to control the cavity length of the fs laser 1. The stabilization of f_{r2} is quite similar to that of the fs laser 1, except that a signal generator (Agilent Technologies, N5181A) is used to provide a reference signal. f_{r1} and f_{r2} are stabilized at a fixed frequency of 100 MHz and a variable frequency, respectively, so that Δf_r can be adjusted. A rubidium (Rb) frequency standard (Stanford Research Systems, FS725) with a frequency accuracy $< 5 \times 10^{-11}$ and a frequency stability $< 2 \times 10^{-11}$ at a gate time of 1 s is used as the reference oscillator of the whole system. To reduce the relative timing jitter between the fs lasers, the internal reference oscillator of the signal generator, which is locked to the Rb frequency standard, is used as the external reference oscillator of the DRO. Also, the DRO, PD 1, and PD 2 are placed on the base plate for the optical parts to lower their thermal fluctuation.

The cross-correlation signal can be used to estimate a relative timing jitter between the fs lasers as well as to trigger the digitizer. For this purpose, the trigger and subsequent pulses were measured in the average mode using a digital oscilloscope, with Δf_r set to 20 Hz. As shown in Fig. 3.10, the trigger pulse has a full width at half maximum (FWHM) of 64 fs, which results from the response time of the PD 3 and the pulse broadening through dispersive optics. However, the subsequent pulse shows a FWHM of 260 fs. The difference between the two FWHM values is caused by the relative time jitter between the fs lasers. The time delay resolution due to the relative timing jitter ($\Delta \tau_j$) gradually increases with the time delay from the trigger point [18]. Hence, it can be said that $\Delta \tau_j$ is better than 260 fs over the entire time delay window of 10 ns.

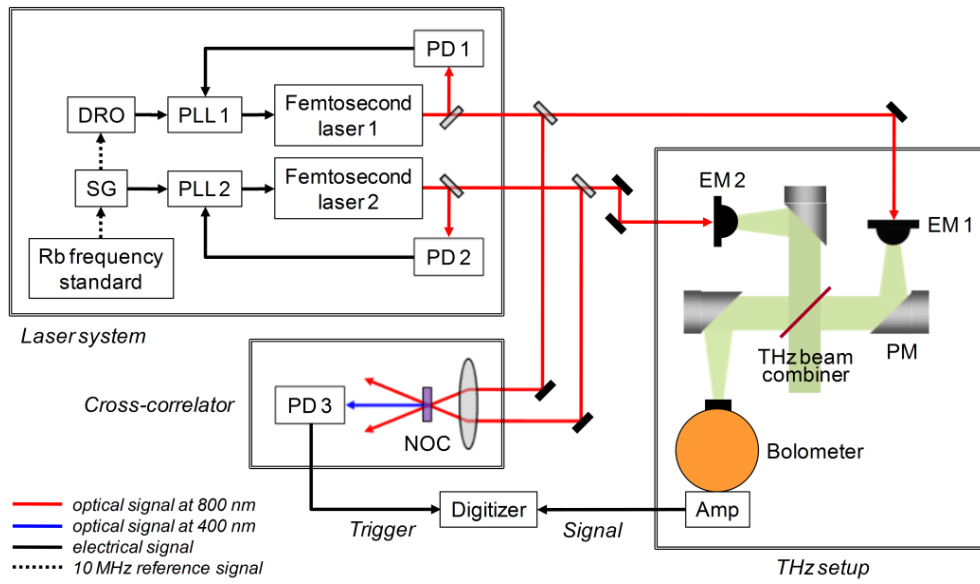


Figure 3.9: Schematic diagram of the experimental setup for THz-FC multiheterodyne spectroscopy. PD: photodetector, DRO: dielectric resonator oscillator, SG: signal generator, PLL: phase-locked loop, EM: THz emitter (PCA here), Amp: preamplifier, and NOC: nonlinear optical crystal.

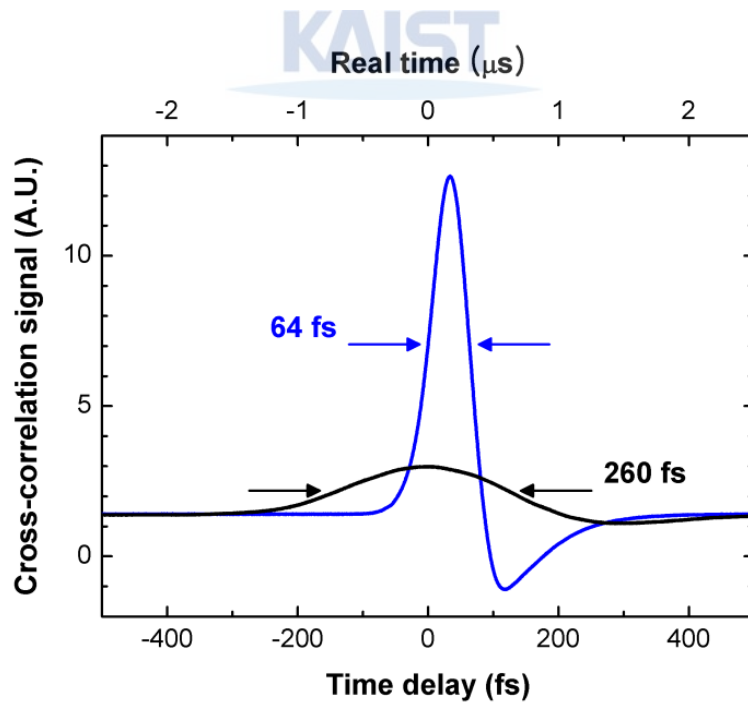


Figure 3.10: Cross-correlation signal between two optical pulses emitted from the fs lasers. The blue line indicates the trigger pulse used to trigger the digitizer and the black one the subsequent pulse 50 ms away from the trigger pulse, with Δf_r set to 20 Hz.

3.3.4. Results and data analysis

Fig. 3.11 shows a typical interferogram measured using the experimental setup for TFCMS. With Δf_r set to 20 Hz, the interferogram was measured over a real time window of 50 ms, as shown on the upper horizontal axis. The data acquisition rate is proportional to half of Δf_r since the lack of waiting time for trigger signal, i.e. the waiting time for the trigger signal right after the number of the time domain data as large as 10^5 is acquired is not enough due to the high speed data acquisition. We averaged over 10,000 interferogram traces acquired during 1,000 s to enhance the signal-to-noise ratio (SNR). The real time is converted to the time delay on the lower horizontal axis, which has a window of 10 ns. The inset displays a zoom into the interferogram at the zero time delay. The interferogram has a nearly symmetric shape around the zero time delay, which reflects that the two THz-FCs have similar time-domain waveforms.

Fig. 3.12 plots THz power spectra obtained by fast Fourier transform (FFT) of interferograms measured with Δf_r of 20 and 100 Hz. The time delay resolution can be limited by the detection bandwidth as well as the relative timing jitter. The time delay resolution limit due to the detection bandwidth is written as

$$\Delta \tau_d = \frac{\Delta f_r}{B_d f_{r1}} \quad (3.21)$$

where $\Delta \tau_d$ is the time delay resolution limit and B_d is a detection bandwidth [18]. When Δf_r is 100 Hz, the time delay resolution is actually limited to 1 ps by the detection bandwidth of 1 MHz rather than by the relative timing jitter. For comparison, we choose 20 Hz for Δf_r so that $\Delta \tau_d$ is 200 fs close to $\Delta \tau_j$. As a result, the spectrum is broader with Δf_r of 20 Hz, as shown in Fig. 3.12. In other words, the detection bandwidth limits the spectrum bandwidth to $1/\Delta \tau_d$ and thus the spectrum bandwidth is broadened up to the maximum bandwidth limited by the relative timing jitter as Δf_r decreases. In this study, we set Δf_r to 20 Hz to acquire data as rapidly as possible without sacrificing the spectrum bandwidth. The spectrum has a 2 THz bandwidth above the noise level and a frequency step of 100 MHz. The spectrum has data points at harmonics of the repetition frequency, corresponding to individual THz-FC modes. There exists a ripple with a 24-GHz period on the spectra, which is considered to be due to multiple reflections between the low-pass filter holder and the entrance aperture of the Winston cone just before the bolometer in the cryostat. Many water vapor absorption lines are observed in the spectra since the measurements were performed at the ambient humidity.

We analyzed the peak SNR of the THz power spectra with varying the measurement time, which was evaluated from the signal and noise spectra. As shown in Fig. 3.13, the peak SNR increases from 20 to 2,000 as the measurement time is augmented from 0.1 s to 1,000 s. We can choose an appropriate value for the measurement time according to requirements for a measurement. Since the peak SNR is proportional to the

square root of the measurement time, i.e., the number of averaged interferogram traces, it is concluded that the signals are at the shot-noise limit.

For the purpose of presenting the high-resolution capability of the spectroscopy, we investigate a THz transmission spectrum of water vapor that is obtained from THz power spectra measured at 5 and 29 % of the relative humidity inside the enclosure of the THz setup, as shown in Fig. 3.14. Actually, the combined THz-FC should probe water vapor for measuring an exact transmission spectrum. In Fig. 3.14(a), the spectrum is plotted together with the dynamic range limit given by the SNR in the frequency range up to 2 THz. The absorption lines seen in Fig. 3.14(a) were fitted to Lorentzian line shape functions whose center frequencies and linewidths are listed in Table 3.2. The standard errors in the parameters for the lines at frequencies above 1.5 THz are larger since the transmittances at the lines are not well within the dynamic range limit. Fig. 3.14(b) displays a magnified view of the spectrum at around 1.16 THz. Thanks to the high spectral resolution, the weak absorption line (indicated by the blue arrow) 10.3 GHz apart from the strong one is clearly resolved and the standard errors in its center frequency and linewidth are only 0.04 and 0.13 GHz, respectively.

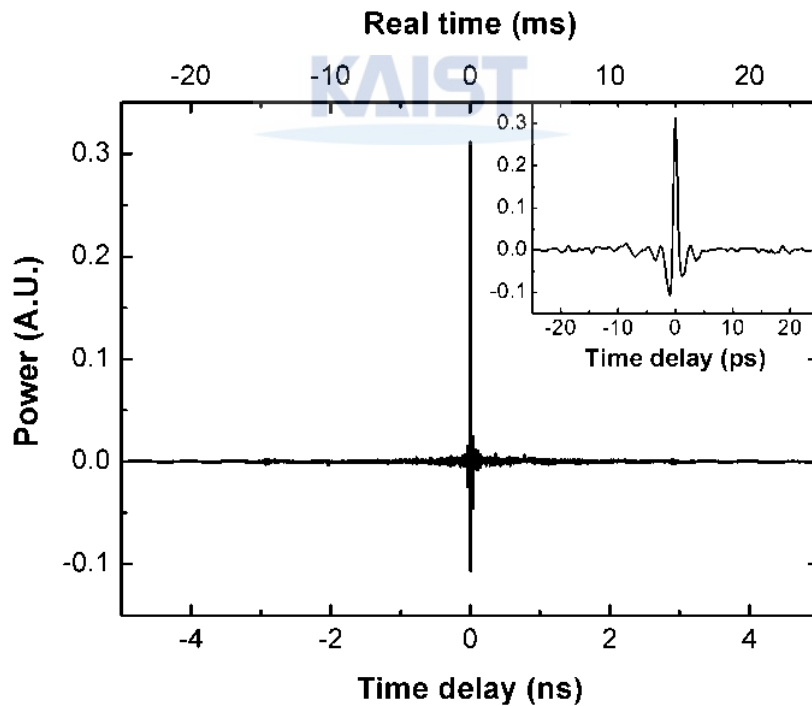


Figure 3.11: Typical interferogram measured from THz-FC multiheterodyne spectroscopy. With Δf_r set to 20 Hz, 10,000 interferogram traces acquired during 1,000 s were averaged to enhance the SNR. The inset shows a zoom into the interferogram at the zero time delay.

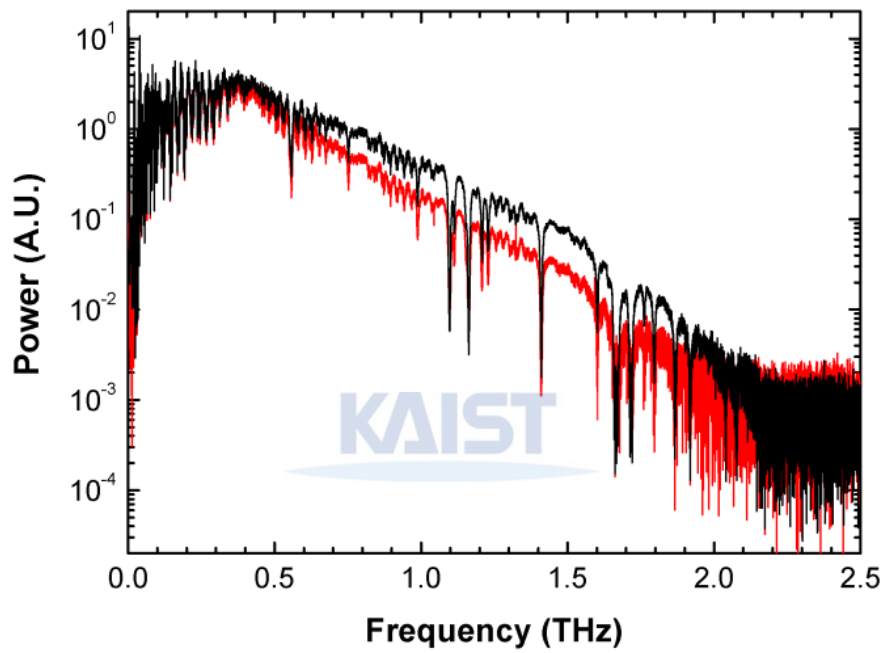


Figure 3.12: THz power spectra obtained by FFT of interferograms measured with Δf_r of 20 (black line) and 100 (red line) Hz. The spectrum acquired with Δf_r of 20 Hz is broader than that with Δf_r of 100 Hz.

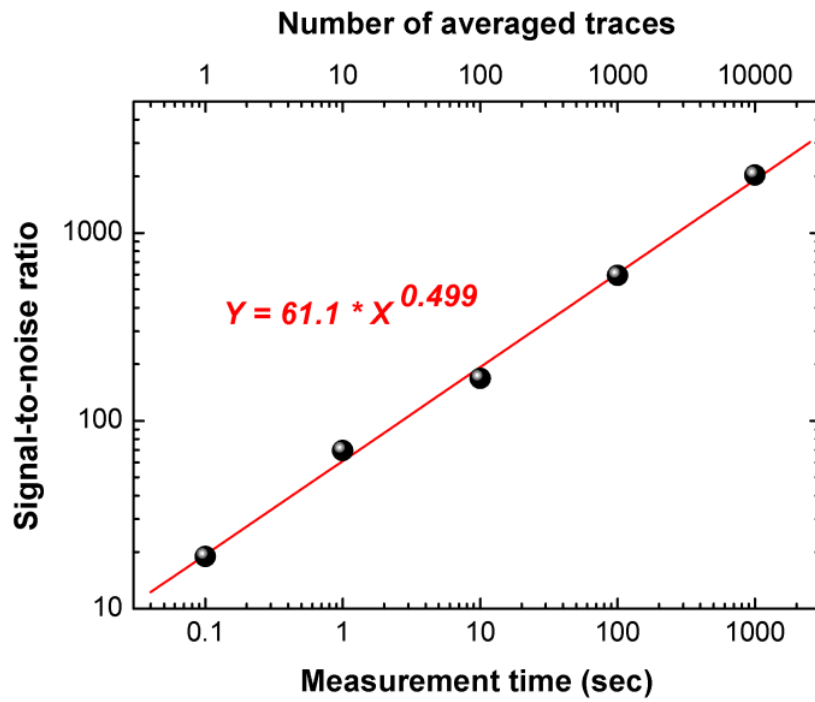


Figure 3.13: The Peak SNR of the THz power spectrum versus the measurement time. The closed circles are experimental results and the red line a fitting result of them.

KAIST

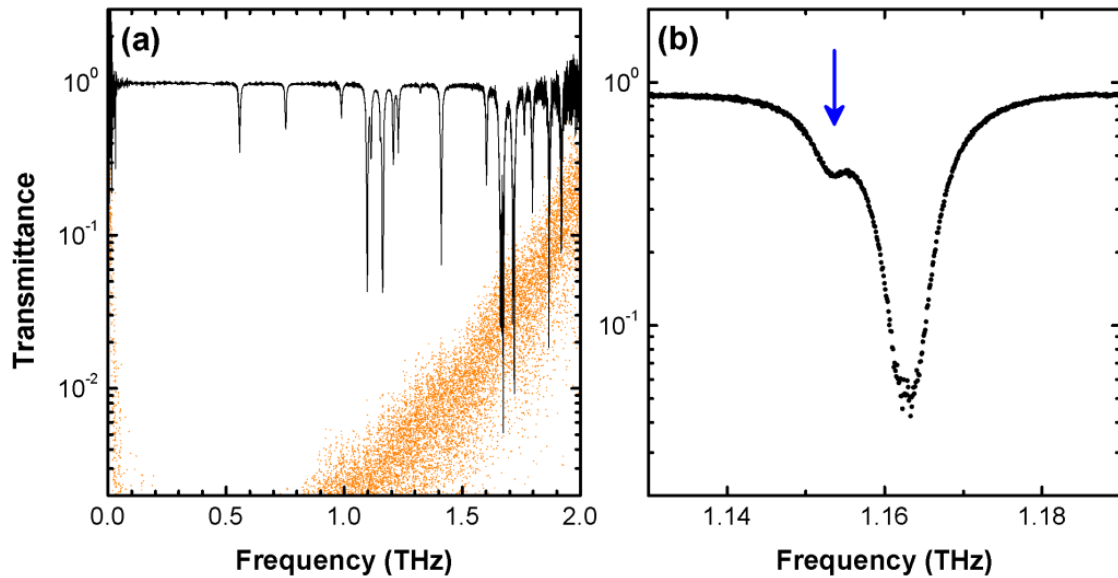


Figure 3.14: (a) THz transmission spectrum of water vapor (black line) and the dynamic range limit (orange dot) in the frequency range up to 2 THz. (b) A zoom into the spectrum in (a) around 1.16 THz.

Table 3.2: Fitting Parameters for Water Vapor Absorption Lines in Fig. 3.14(a).

	Center frequency (GHz)	Linewidth (GHz)
1	557.25 ± 0.01	8.16 ± 0.04
2	752.27 ± 0.01	7.35 ± 0.03
3	987.95 ± 0.03	7.20 ± 0.10
4	1097.43 ± 0.01	11.58 ± 0.04
5	1113.62 ± 0.02	7.77 ± 0.06
6	1152.79 ± 0.04	7.21 ± 0.13
7	1163.10 ± 0.02	12.35 ± 0.05
8	1207.86 ± 0.01	7.63 ± 0.04
9	1228.87 ± 0.02	7.75 ± 0.05
10	1321.80 ± 0.06	5.07 ± 0.19
11	1410.78 ± 0.01	10.81 ± 0.05
12	1602.19 ± 0.07	7.78 ± 0.23
13	1660.33 ± 0.22	16.34 ± 0.58
14	1673.78 ± 0.24	16.13 ± 0.68
15	1716.60 ± 0.10	19.57 ± 0.32
16	1762.15 ± 0.12	6.62 ± 0.35
17	1796.16 ± 0.08	9.59 ± 0.25
18	1867.74 ± 0.08	11.55 ± 0.25
19	1919.15 ± 0.08	11.29 ± 0.26

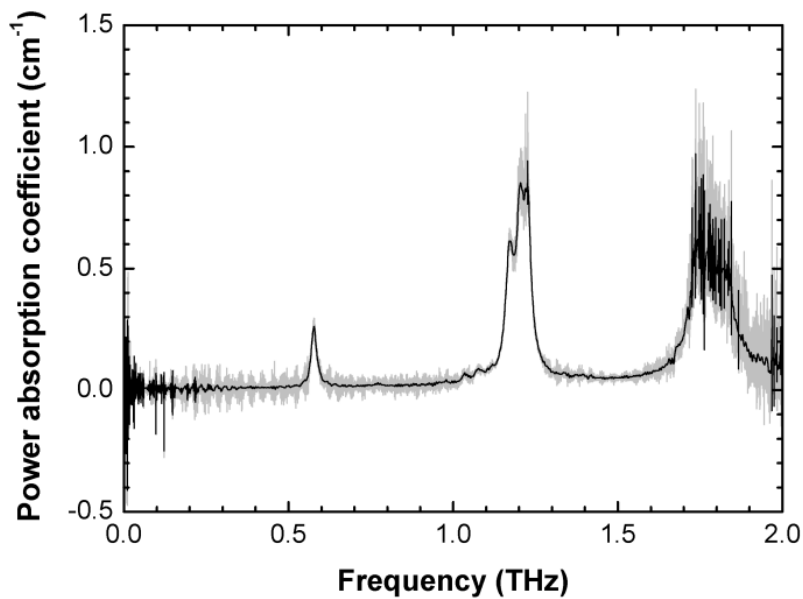


Figure 3.15: Power absorption spectrum (gray line) of ammonia at 1 atm in the frequency range up to 2 THz, measured using a gas cell. The black line displays the denoised spectrum through the wavelet power spectrum estimation.

To test the spectrometer, we also measured ammonia as a sample gas. A gas cell with a 1.5 inch diameter and a 50 mm length was used for this measurement, which has 3-mm-thick polyethylene windows. With the gas cell placed just before the cryostat containing the bolometer, we measured a power absorption spectrum of ammonia at 1 atm, as shown in Fig. 3.15. The measured spectrum was also denoised through the wavelet power spectrum estimation, as indicated by the black line in Fig. 3.15 [43]. Rotational lines of ammonia are shown in the absorption spectrum over the frequency range up to 2 THz. The line of $J = 0$ has a center frequency of 577.69 GHz and a linewidth of 26.44 GHz [44,45]. The lines at around 1.2 and 1.8 THz cannot be well analyzed since the transmitted powers at the lines fall into the noise level due to the strong absorption of ammonia at the high pressure.

3.4 Electronically controlled optical sampling THz-TDS

3.4.1. Introduction

The ASOPS always makes the time delay scanned over a whole time delay window determined by a laser repetition frequency. For example, the ASOPS system using 100 MHz repetition-rate fs lasers has a fixed

time delay window of 10 ns. Unless high frequency resolution is needed, only a time delay window of several tens picoseconds is generally enough to investigate a material response in the THz spectral range. In this case, more than 99 % of the data acquisition time is unnecessary. Thus, there is room to enhance the measurement speed by avoiding the unnecessary time delay scanning.

3.4.2. Principles of operation

For high-speed measurement, we apply the ECOPS technique to the THz-TDS. In the ECOPS technique, two synchronized fs lasers produce pump and probe optical pulses, respectively, and modulation of the cavity length of one of the lasers via a piezoelectric transducer (PZT) serves to sweep the probe pulse against the pump pulse in a precisely controlled manner [35]. The ECOPS technique has been recently applied to optical coherence tomography [36]. The main advantage of the ECOPS technique is that a temporal scan range as well as a scan frequency can be electronically adjusted. With a narrowed temporal scan range, a scan frequency can be raised and consequently a measurement time can be shortened. In this letter, we demonstrate high-speed THz-TDS based on the ECOPS using two synchronized Ti:sapphire fs lasers with a 100 MHz repetition frequency.



3.4.3. Experiment

Fig. 3.16 illustrates our experimental setup for ECOPS THz-TDS. Two synchronized fs lasers emit pump and probe optical pulses used for THz wave generation and detection, respectively. The fs lasers have a center wavelength of 800 nm and a pulse duration of 10 and 20 fs, respectively. For synchronization, the tenth harmonics of the repetition frequencies of the two lasers are separately phase-locked to the 1 GHz common output of a signal generator. The phase error signal output from a double-balanced mixer is supplied via a proportional-integral amplifier and a high-voltage amplifier to a PZT which a cavity mirror is attached to. The two laser repetition frequencies are synchronized at 100 MHz by controlling the cavity lengths via the PZTs. Then, the phase difference between the pump and probe pulses can be controlled by an external offset voltage applied to the locking electronics for one of the lasers, as shown in Fig. 3.16. Thus, the time delay between the pump and probe pulses can be repetitively scanned at the modulation frequency of the external offset voltage. The scan rate and time delay window can be adjusted by the modulation frequency and amplitude of the external offset voltage. The signal generator and the function generator supplying the external offset voltage are referenced to a Rb frequency standard.

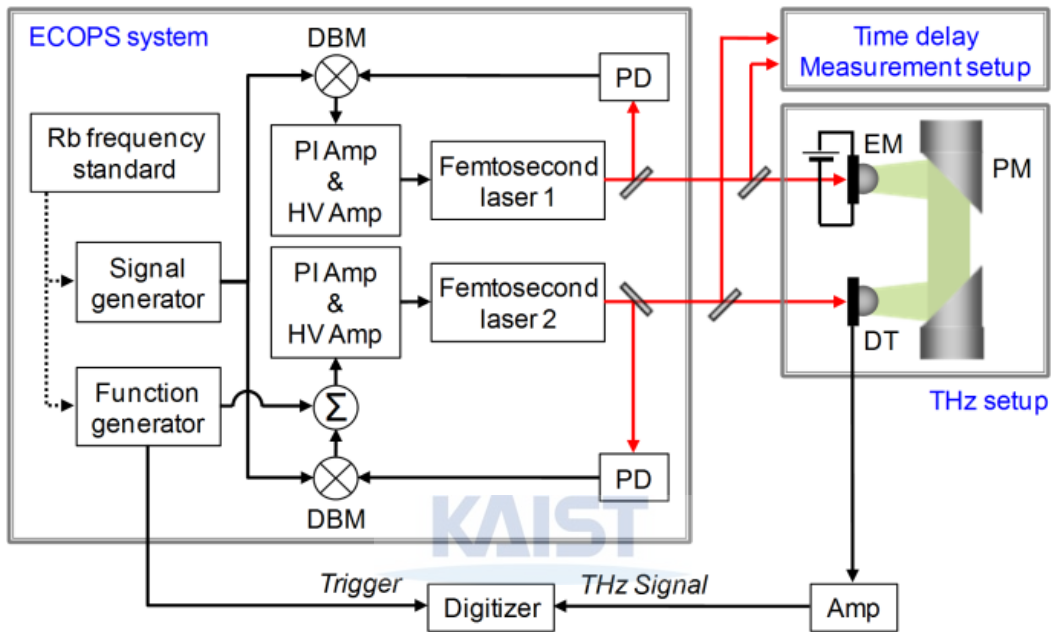


Figure 3.16: Schematic diagram of the experimental setup for ECOPS THz-TDS. DBM: double-balanced mixer, PI Amp: proportional-integral amplifier, HV Amp: high-voltage amplifier, PD: photodetector, EM: THz emitter, DT: THz detector, PM: off-axis parabolic mirror, Amp: preamplifier. Optical beams are represented by red lines, electrical signals by black solid lines, and 10 MHz reference signals by black dashed lines, respectively.

We use two low-temperature-grown GaAs photoconductive antennas as a THz emitter (EM) and detector (DT). The pump pulses are incident on the biased EM to generate THz pulses, which are guided into the DT by using two off-axis parabolic mirrors. Then, the probe pulses are used to optically sample the THz pulses incident upon the DT. The photocurrent output from the DT, which represents the magnitude of the electric field of the THz pulses, is amplified by a variable-gain preamplifier and then is acquired by a 24-bit flexible resolution digitizer triggered by the sync signal of the function generator.

3.4.4. Results and data analysis

Temporal variation of the time delay made by the ECOPS system can be measured using the time delay measurement setup depicted in Fig. 3.17(a). Optical pulse trains from the two fs lasers are detected by photodetectors, respectively. Amplifiers and 100 MHz low-pass filters filter out the 100 MHz fundamental components from the output signal of the photodetectors. The phase difference signal of the fundamental components, output from a 1.9 MHz low-pass filter following a double-balanced mixer, is acquired by the digitizer triggered by the sync signal of the function generator. The signal ($V(t)$) measured from the time delay measurement setup is related to the phase difference ($\Delta\phi(t)$) by $V(t) = A_0 \cos \Delta\phi(t)$, where A_0 is a coefficient depending on measurement conditions. Fig. 3.17(b) shows $V(t)$ measured from the time delay measurement setup when the time delay is swept at a 1 kHz scan rate by the ECOPS system. The temporal variation of the time delay ($\tau(t)$) can be determined from $V(t)$ by

$$\tau(t) = \frac{\Delta\phi(t)}{2\pi f} = \frac{1}{2\pi f} \cos^{-1} \left(\frac{V(t)}{A_0} \right), \quad (3.22)$$

where f is the repetition frequency of 100 MHz here, as plotted in Fig. 3.17(b).

To evaluate the time delay resolution due to the relative timing jitter between the two fs lasers, we performed an optical cross-correlation measurement under the same condition of the ECOPS system as in Fig. 3.17(b) [48]. The cross-correlation signal was measured using an oscilloscope triggered by the sync signal of the function generator. Fig. 3.18 shows cross-correlation signals between two optical pulses emitted from the fs lasers. A single scan trace of the cross-correlation signal was measured to have a full width at half maximum (FWHM) of 25 fs. An average over 1,000 scans of the cross-correlation signal resulted in a FWHM of 67 fs, which represents the time delay resolution due to the timing jitter.

The time scale of a THz temporal waveform measured by ECOPS is calibrated using the time delay measured in such a way as described above. A typical THz waveform measured by ECOPS is plotted against the time delay in Fig. 3.19(a). Here, we set a scan rate to 1 kHz and obtained a time delay window of 77 ps

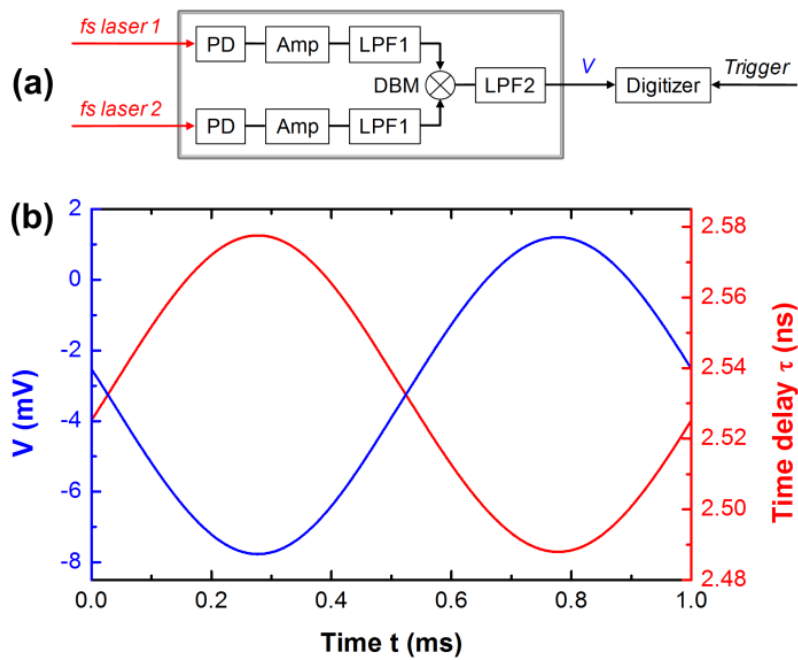


Figure 3.17: Schematic diagram of the time delay measurement setup. LPF1: 100 MHz low-pass filter, LPF2: 1.9 MHz low-pass filter. (b) Signal (blue line) measured from the time delay measurement setup and temporal variation of the time delay (red line) determined from the signal by Eq. (3.22) when the time delay is swept at a scan rate of 1 kHz by the ECOPS system.

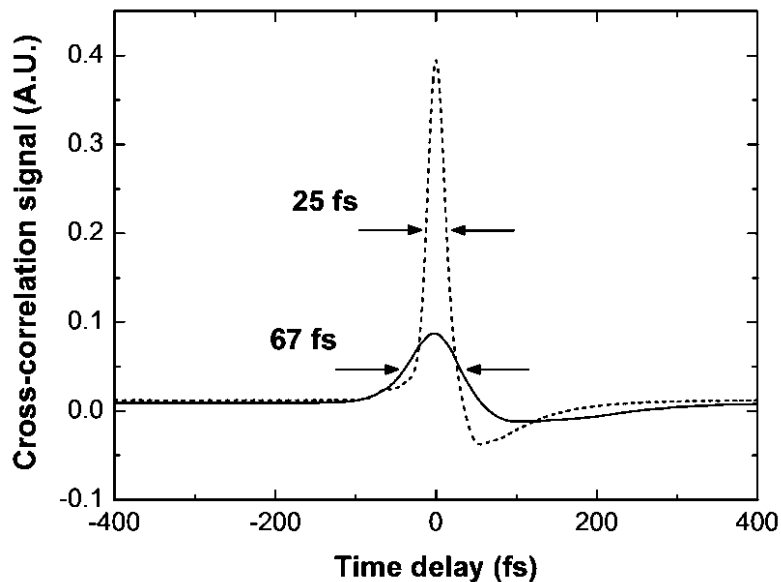


Figure 3.18: The dashed curve represents a single scan trace of cross-correlation signal and the solid curve an average over 1,000 scans of cross-correlation signal.

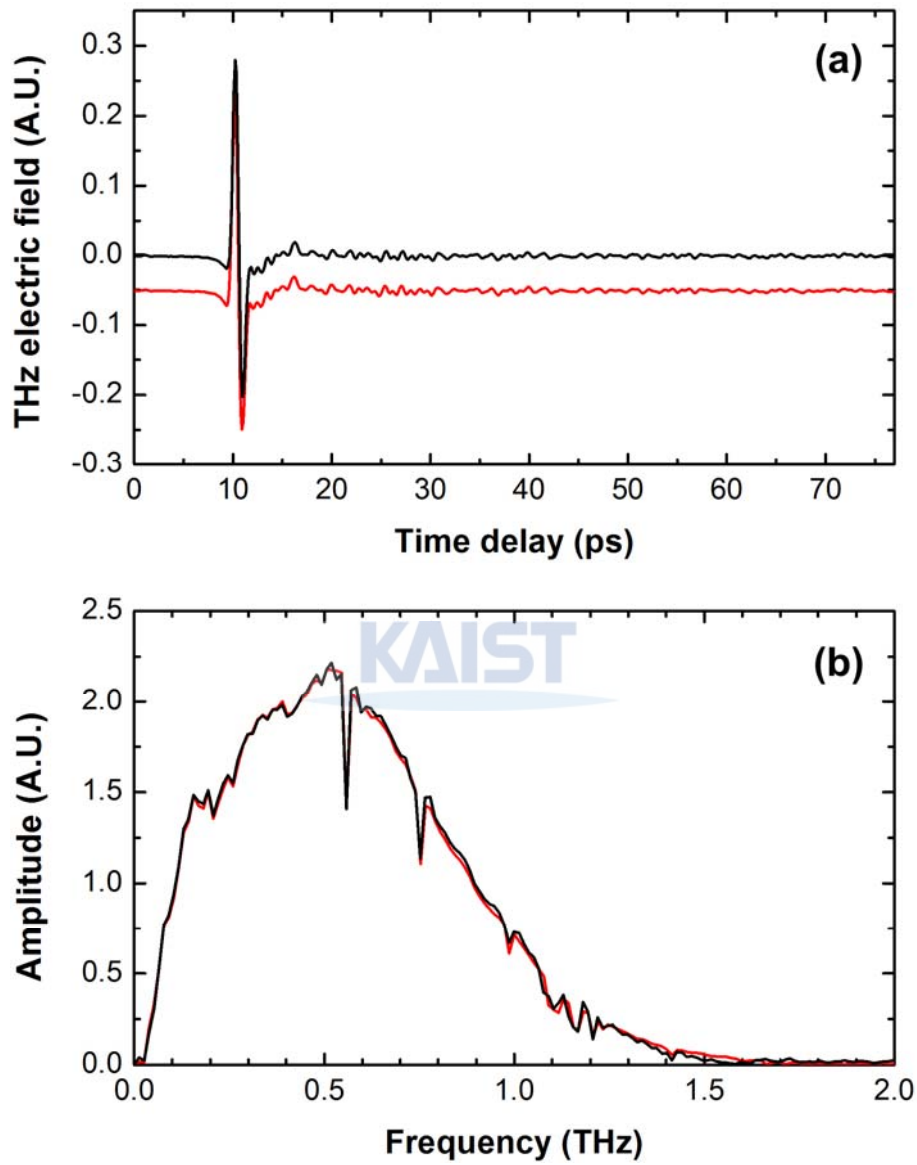


Figure 3.19: (a) Typical THz temporal waveforms measured by ECOPS and ASOPS. (b) THz amplitude spectra obtained by FFT of the waveforms in (a). The black and red curves indicate ECOPS and ASOPS results, respectively.

corresponding to a spectral resolution of 13 GHz. The gain and bandwidth of the preamplifier was set to 10^7 and 220 kHz, respectively, and the data was acquired at a sampling rate of 2 MS/s, yielding a time delay step of ~ 100 fs. For comparison, a THz waveform measured by ASOPS is also displayed in Fig. 3.19(a). For ASOPS, the laser repetition frequencies were stabilized at 100 MHz and 100 MHz - 20 Hz by using reference signals of a dielectric resonator oscillator and the signal generator, respectively [48]. All the measurement conditions else were the same with those of ECOPS. The THz waveforms measured by ECOPS and ASOPS were obtained by averaging 1,000 consecutive traces acquired during 1 and 50 sec, respectively. The THz waveform measured by ASOPS is displayed with an offset on a part of the entire 10 ns time delay window. As shown in Fig. 3.19(a), the THz waveform by ECOPS is in good agreement with that by ASOPS.

To obtain a THz spectrum by fast Fourier transform (FFT) of a time-domain data measured by ECOPS, the time-domain data should be interpolated since the time delay step is not regular. Fig. 3.19(b) shows the THz amplitude spectrum obtained by FFT after interpolation of the time-domain data by ECOPS shown in Fig. 3.19(a), together with that by ASOPS. The spectra have almost identical shapes and a spectral bandwidth of approximately 1.5 THz. We made sure that the spectral bandwidth was limited by the photoconductive antennas used for THz wave generation and detection [18], and thus it could be extended by altering the THz wave generation and detection methods [19]. Also, the frequencies of absorption lines of water vapor agree well in the spectra by ECOPS and ASOPS. Therefore, ECOPS is confirmed to exactly measure a THz pulse like ASOPS.

To compare the measurement speeds of ECOPS and ASOPS, we investigated signal-to-noise ratios (SNR) of THz temporal waveforms measured by ECOPS and ASOPS under the same measurement condition as in Fig. 3.19 with varying the number of averaged traces. For ASOPS, a scan rate given by a laser repetition frequency difference was set to 20 Hz, which led to the maximum SNR at a given measurement time, not reducing the THz spectral bandwidth with the preamplifier set to 220 kHz bandwidth offering the highest gain and lowest noise [48]. The SNR was evaluated as the ratio of the peak-to-peak value of a THz temporal waveform to the standard deviation of a noise in the time domain. Fig. 3.20 shows the SNR versus the measurement time when 1, 10, 100, and 1,000 traces are acquired and averaged. The lines are fits of the results to $Y = \alpha * X^\beta$. The noise levels are close to the shot noise limit since β is 0.49 for both the ECOPS and ASOPS. Fig. 3.20 clearly shows that the measurement speed of ECOPS is 50 times higher than that of ASOPS.

Time delay window, SNR, measurement time, and spectral bandwidth should be considered in THz-TDS. In ECOPS THz-TDS, adjustable parameters include a gain and bandwidth of the preamplifier, a sampling rate of the digitizer, and a scan rate and time delay window set by the function generator. By adjusting

the parameters, we tried to maximize a time delay window and minimize a measurement time taken to reach a desired SNR with maintaining the maximum spectral bandwidth. It was found that the measurement condition of Fig. 3.19 was optimal with a limitation of a scan rate due to use of the PZT having a finite bandwidth. A measurement time can be reduced with a shorter time delay window, or a time delay window can be extended with a longer measurement time.

For ASOPS THz-TDS, a high laser repetition frequency has an advantage for high-speed scanning as a scan rate can be even higher with a higher repetition frequency [30]. However, pump and probe pulse energies are higher with a lower repetition frequency. Consequently, a low repetition frequency is advantageous in view of a measurement time needed to reach a desired SNR. Fig. 3.20 shows that the ECOPS THz-TDS demonstrated here enables much more rapid measurement than even the ASOPS THz-TDS with a low repetition frequency of 100 MHz.

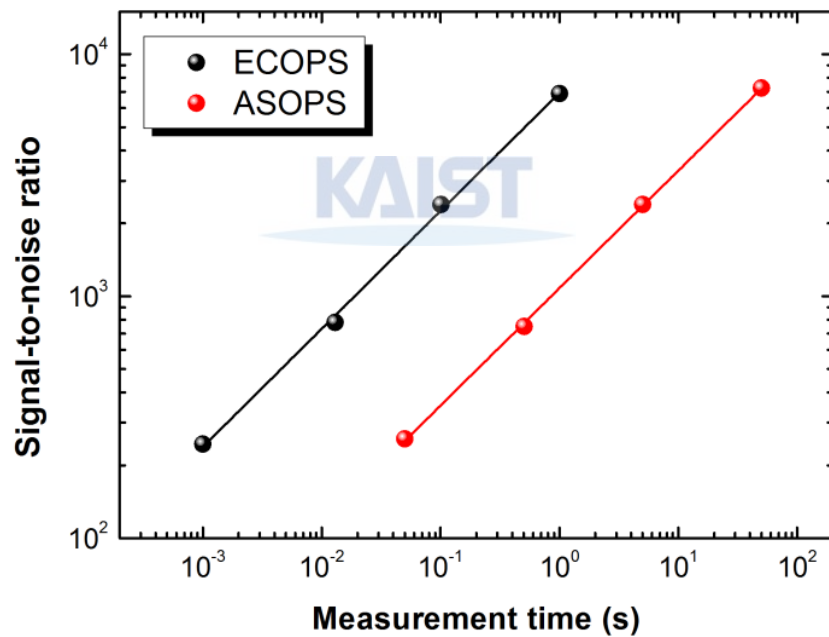


Figure 3.20: SNR versus measurement time for THz pulse measurements using ECOPS and ASOPS. The black dots represent ECOPS results and the red dots ASOPS results. The lines are fits of the results to $Y = \alpha * X^\beta$.

3.5 Discussion

We clearly demonstrated that the WPSET was successfully applied to high-resolution THz-TDS.

Through the wavelet power spectrum estimation, the fluctuations on high-resolution THz amplitude spectra could be removed with maintaining original spectral information. By investigating a THz transmission spectrum of water vapor, the parameters of the spectral singularities were shown to remain unchanged after the processing. Also, optical properties of ZnO were surveyed to show that the WPSET can effectively denoise an absorption coefficient spectrum measured from high-resolution THz-TDS. This study shows that the WPSET is ideally suitable for high-resolution THz-TDS. The WPSET will make high-resolution THz-TDS more practical by enhancing the spectrum quality. Although this work was performed in the THz frequency region, the WPSET can also be applied to high-resolution spectroscopy in other frequency regions.

Coherent multiheterodyne spectroscopy was demonstrated using stabilized harmonic THz frequency combs. fs laser based THz frequency combs with slightly different repetition frequencies are combined to be used as a source. The maximum time delay window of 10 ns can be acquired, determined by the 100 MHz repetition frequency. A THz power spectrum, which is obtained by FFT of an interferogram, has data points at harmonics of the repetition frequency, equivalent to individual THz frequency comb modes. The high-resolution capability of the TFCMS was presented through characterization of the weak absorption line in close proximity to the strong one in the THz transmission spectrum of water vapor. We have also measured ammonia using a gas cell to test the spectrometer. In addition to high-resolution spectroscopy, this spectroscopic technology is potentially applicable to transient spectroscopy of non-repetitive phenomena through repetition of a rapid single scan, which is our future work.

Lastly, we have demonstrated high-speed THz-TDS based on ECOPS. It was confirmed that ECOPS could exactly measure a THz pulse as ASOPS could. A measurement time was also shown to be reduced by a factor of 50 by using ECOPS compared with ASOPS. In terms of a measurement time taken to reach a desired SNR, ECOPS THz-TDS is the most rapid method of various ones for THz-TDS at this time to our knowledge. This high-speed ECOPS THz-TDS has potential applications such as real-time monitoring or sensing based on THz spectra and rapid THz spectroscopic imaging.

Chapter 4. Polarization-sensitive THz-TDS

4.1 Introduction

One of the basic physical parameter of a material, which used in the evaluation of components in optical system, is the birefringence. The birefringence of a material is defined by the difference in the indices of refraction for the extraordinary and ordinary waves. The birefringence in the optical region (~ 1 eV range) is related to the crystal symmetry [49]. For example, cubic crystal system is isotropic, while hexagonal, rhombohedral, tetragonal crystal systems are anisotropic and have a uniaxial birefringence ($\epsilon_{xx}(\infty) = \epsilon_{yy}(\infty) \neq \epsilon_{zz}(\infty)$). Other crystal systems, such as orthorhombic, monoclinic, and triclinic, are anisotropic and have a biaxial birefringence ($\epsilon_{xx}(\infty) \neq \epsilon_{yy}(\infty) \neq \epsilon_{zz}(\infty)$). Birefringence in the THz region (few meV range) is related with TO-LO splitting in mid-infrared range without damping, as Lyddane-Sachs-Teller relationship be obeyed as follows [50]:

$$\epsilon_{xx}(\omega) = \epsilon_{xx}(\infty) \frac{(\omega_{LO}^2 - \omega^2)}{(\omega_{TO}^2 - \omega^2)} \quad \text{and} \quad \epsilon_{zz}(\omega) = \epsilon_{zz}(\infty) \frac{(\omega_{LO}^2 - \omega^2)}{(\omega_{TO}^2 - \omega^2)}. \quad (4.1)$$

If one include a damping constant (γ), the frequency-dependent dielectric function should be modified as follows:

$$\epsilon_{xx}(\omega) = \epsilon_{xx}(\infty) \frac{(\omega_{LO}^2 - \omega^2 - i\gamma\omega)}{(\omega_{TO}^2 - \omega^2 - i\gamma\omega)}. \quad (4.2)$$

Of course, one can calculate frequency-dependent complex refractive index, $n(\omega)$, from frequency-dependent complex dielectric constant, $\epsilon(\omega)$, by using a simple formula from electrodynamics, $\epsilon(\omega) = n^2(\omega)$. Therefore, there are three main reasons for THz birefringence in the crystal: 1) The crystal symmetry of the sample is anisotropic, 2) TO-LO splitting is fundamental relationship between high-frequency dielectric constant and frequency-dependent dielectric constant, 3) such TO-LO splitting is again function of the crystal symmetry. In this chapter, we present the experimental results by using a polarization sensitive THz-TDS as well as *ab initio* calculation for the ZnO, LiNbO₃, and Al₂O₃.

Our *ab initio* calculations have been implemented with the CRYSTAL09 [51]. CRYSTAL09 has an outstanding ability to describe the ground state electronic structure of materials using Hatree-Fock and Kohnsham hamiltonians or various hybrid approximations. Fig. 4.1 shows the brief procedure of the *ab initio* calculation. As a first step of geometry optimization, the lattice parameters are optimized to minimize the total en-

ergy. Then, we use the Coupled Perturbation Kohn-Sham scheme (CPKS) for the accurate calculation of the high frequency dielectric tensor, ϵ_∞ , contributing to the frequency dependent dielectric function $\epsilon(\omega)$. Through well localized Wannier functions, we evaluate the Born charges. At last, vibrational modes frequencies are derived from the hessian matrix, whose elements are the second derivatives of the total energy with respect to the atomic Cartesian coordinates, evaluated numerically from analytical gradients.

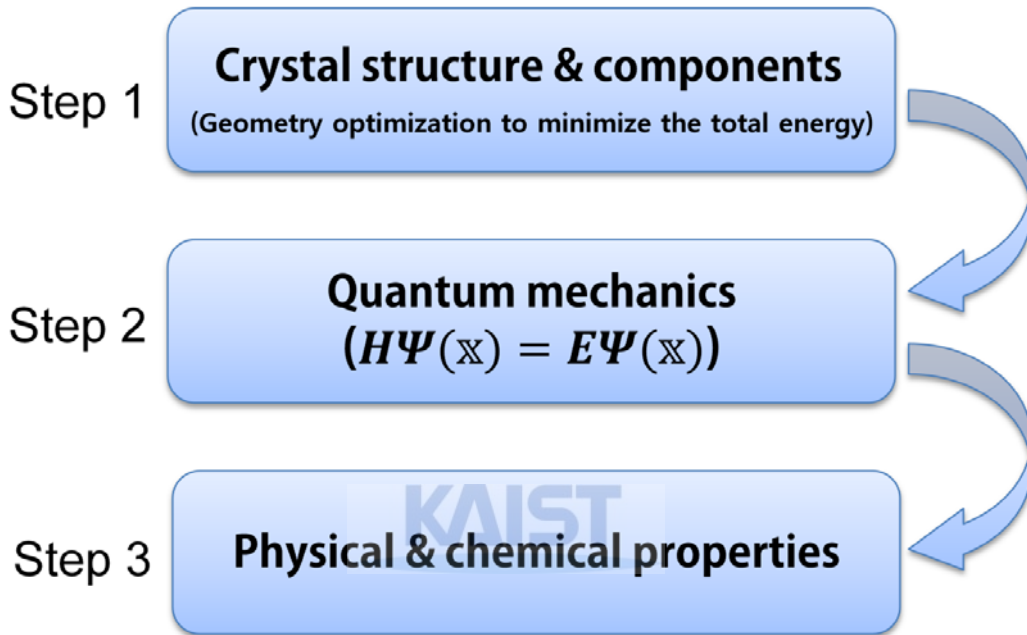


Figure 4.1: Brief procedure of *ab initio* calculation using the CRYSTAL09.

4.2 THz birefringence in ZnO

4.2.1 Introduction

Zinc oxide (ZnO) is a wide-band-gap II-VI semiconductor with a direct energy gap of 3.37 eV at room temperature. ZnO crystallizes in the wurzite structure at ambient pressure and temperature. This is hexagonal structure characterized by two interconnecting sublattices of Zn^{2+} and O^{2-} , such that each Zn ion is surrounded by a tetrahedral of O ions, and vice-versa. It is thus optically anisotropic (uniaxial). There are 4 atoms per unit cell in single crystal wurzite ZnO. Because of its transparency in the most of the visible spectral range and the opacity in the ultraviolet and blue region, ZnO has been considered with enormous attention as an ideal candidate for high-speed electro-optic, acousto-optic, and optoelectronic devices [52]. Recently, THz wave genera-

tion was demonstrated from a ZnO photoconductive antenna excited by ultraviolet pulses [53], and the far-infrared optical and dielectric properties of ZnO were experimentally characterized by use of THz-TDS [54]. ZnO has a number of advantages for THz photonics: wide bandgap, high breakdown voltage, high resistivity and mobility, optical transparency, and easy fabrication. Although there exist a lot of reports on the optical properties of ZnO [54-56], there is no experimental report on THz birefringence of ZnO.

In this chapter, we report the ordinary and extraordinary refractive indices (n_o and n_e) as well as the absorption coefficients of ZnO single crystals in the frequency region of 0.25 ~ 1.35 THz. For this, azimuthal angle dependence of transmission has been measured in a parallel-polarization configuration THz time-domain spectrometer based on asynchronous optical sampling and the experimental result is compared with an *ab initio* calculation of dielectric and optical properties. The experimental results of the THz birefringence for the samples show good agreement with the calculated values from the full phonon considerations. It is noteworthy that the difference of the TO-LO splitting between the optical phonon branches (A_1 and E_1) predominantly contributes to the huge birefringence of ZnO in the THz frequency region.

4.2.2 Experiment

We used both-side polished 10 mm × 10 mm × 2 mm-thick ZnO single crystals with crystal orientations of <10-10> and <0001>, which crystallized to a hexagonal wurzite structure, such that each Zn ion is surrounded by a tetrahedral of O ions, and vice-versa [52]. Thus, birefringence occurs for a THz wave propagating normal to the (10-10) crystal surface and not to the (0001) surface. ZnO crystal was manufactured by the hydrothermal technology. Hydrothermal ZnO single crystals are grown in high pressure autoclaves by means of direct temperature drop in aqueous solutions of KOH + LiOH at crystallization temperature 320-400 °C and pressure 20-70 MPa. Inside the autoclaves there are special vessels made of corrosion-resistant alloys – they serve to protect autoclaves from corrosion. The charge, the bait and the chemical solution are put into the vessel, then the vessel is hermetically sealed and placed into the autoclave. Finally the autoclave is filled with water and is also sealed hermetically. After that the autoclave is heated to the fixed temperature. The whole production cycle takes 100-150 days.

For a precision measurement of THz birefringence in ZnO, asynchronous-optical-sampling THz-TDS was used in transmission geometry [48,57]. The experimental configuration is illustrated in Fig. 4.2. We employed a pair of pump and probe Ti:Sapphire mode-locked fs lasers. These lasers have a center wavelength of 800 nm, and the pulse durations of pump and probe beams are 10 and 20 fs, respectively. The whole laser system is placed on a temperature-controlled base-plate to reduce thermal fluctuation. The repetition frequencies

of the pump and probe beams are stabilized at 100 MHz and 100 MHz - 20 Hz by two phase-locked loops, respectively. By using double-balanced mixers (DBM), the tenth harmonics of f_{r1} and f_{r2} are compared with the outputs of a 1 GHz dielectric resonator oscillator (DRO) and a signal generator (Agilent Technologies N5181A), respectively. The DRO and signal generator share a 10 MHz reference oscillator to reduce the relative timing jitter between the optical pulses from the two fs lasers. The phase error signal output from the DBM is amplified by a proportional-integral amplifier and a high-voltage amplifier and is supplied to a piezo-electric transducer (PZT) to which a cavity mirror is attached. The repetition frequencies are stabilized by controlling the cavity lengths via the PZTs. Two low-temperature-grown GaAs photoconductive antennas were used for emission and detection of pulsed THz waves. The pump beam is incident on the biased THz emitter to generate a pulsed THz wave linearly polarized along the vertical axis, which is collimated and focused on the ZnO sample by two off-axis parabolic mirrors. The THz wave transmitted through the ZnO sample is collimated and focused on the THz detector by two additional off-axis parabolic mirrors. The probe beam is used to optically sample the THz wave incident upon the THz detector. The photocurrent output from the THz detector represents the magnitude of the electric field of the THz wave, which is oriented such that only the vertical component of the electric field is detected. It is amplified by a variable-gain current amplifier and then is acquired by a digitizer. The enclosure containing the THz beam path is purged with dry air to eliminate the absorption by water vapor in ambient air.

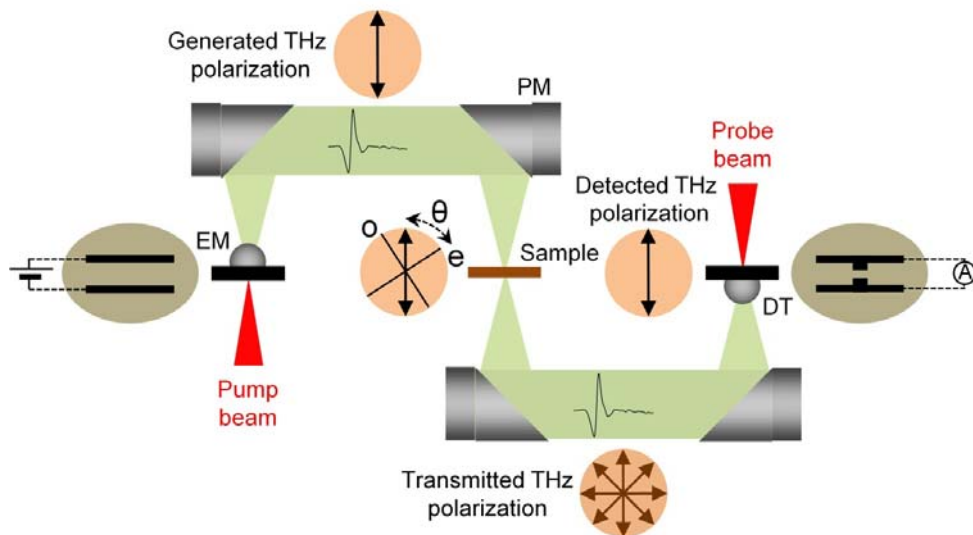


Figure 4.2: Illustration of the experimental configuration. PM: off-axis parabolic mirror, EM: THz emitter, DT: THz detector, o: ordinary axis, and e: extraordinary axis.

4.2.3 Experimental results

In contrast with the <0001> orientation, birefringence was observed in the <10-10> orientation. The reference (input) and transmitted (output) THz pulses are measured without and with the <10-10>-oriented ZnO sample, respectively. Fig. 4.3(a) shows the transmitted THz waveforms measured with rotating the sample in the parallel-polarization configuration illustrated in Fig. 4.3(b). The time delay position of the THz pulse oscillates with a 180° period of the azimuthal angle, which implies the existence of birefringence. Using Fourier analysis of input and output pulses, we can obtain the frequency-resolved index of refraction, $n(\omega)$, and absorption coefficient, $\alpha(\omega)$, given by

$$n(\omega) = 1 + \frac{c\theta(\omega)}{\omega L} \quad \text{and} \quad (4.3)$$

$$\alpha(\omega) = \frac{2}{L} \ln \left[\frac{4n(\omega)}{T(\omega)(n(\omega)+1)^2} \right], \quad (4.4)$$

where L is the crystal thickness, c is the speed of light, and T and θ are defined as $Te^{i\theta} = E_{\text{output}}(\omega)/E_{\text{input}}(\omega)$ [58]. During the process of data analysis, we have found that the phase spectra, which are used to obtain the refractive indices, better converge to zero at the zero frequency limit without the need of adding any phase offset to the phase spectra, if we choose a longer time delay window. When analyzing data over a shorter time delay window (40 ps or so), we should add a phase offset to the individual phase spectrum in order to make the spectrum converge to zero at the zero frequency limit, which may make an error in the birefringence. Thus, we used a longer time delay window despite the need of removing Fabry-Perot ripples. To remove the Fabry-Perot effect of ZnO, the amplitude and phase spectra, of which the frequency resolution is 2.63 GHz, determined from the time delay window of 380 ps, are smoothed using adjacent-averaging of 19 points, closely equal to twice the period of the Fabry-Perot ripple on the spectrum. Therefore, the spectral resolution for the refractive indices can be 50 GHz. Fig. 4.3(c) shows the dispersions of n_o and n_e of the <10-10>-oriented ZnO sample. The birefringence defined by $\Delta n = n_e - n_o$ is measured 0.180 ± 0.003 in the frequency region of 0.25 ~ 1.35 THz. Compared to the crystalline quartz ($n_o = 2.108$ and $n_e = 2.156$ at 1 THz) [59], the birefringence of the ZnO is ~3.8 times larger at 1 THz.

The birefringence causes the phase retardation, $\Delta\theta$, between the ordinary and extraordinary waves given by $\Delta\theta = \omega L \Delta n / c$, where ω is the angular frequency. Fig. 4.4(a) shows the phase retardation for the ZnO which results from the birefringence of Fig. 4.3(c). The phase retardation is shown to be π at 0.42 THz and 3π at 1.24 THz. We also measured transmission spectra of the ZnO crystal in the parallel-polarization configuration illustrated in Fig. 4.2, rotating it to change the azimuthal angle, as shown in Fig. 4.4(b). The 0° and

90° orientations correspond to the o and e waves in Fig. 4.4(b). As the azimuthal angle becomes close to 45°, the amplitude of the parallel-polarization component reduces greatly around 0.42 THz. It means that the 2-mm-thick ZnO crystal gives half-wave (π) phase retardation at 0.42 THz so that the transmitted THz wave has a perpendicular polarization at 45°. It can be also seen that 3π phase retardation occurs at 1.24 THz. Fig. 4.5 also displays the azimuthal angle dependence of the transmittances (from 0° to 360° at a step of 5°) at 0.42 and 1.24 THz, measured in the parallel-polarization configuration. The transmittances have maximum values at the 0°, 90°, and equivalent orientations without change in the polarization before and after transmission through the ZnO sample. In contrast, half-wave phase retardation makes the transmittances reach minima at the 45°, 135°, and equivalent orientations, rotating the polarization by 90°. Thus, the ZnO crystal of 2-mm thickness can be used as a half-wave plate at 0.42 and 1.24 THz, and also a quarter-wave plate at 0.62 and 1.03 THz. As shown in Fig. 4.8(b), the absorption coefficients of the ZnO sample for both ordinary and extraordinary waves are measured lower than 4 cm⁻¹ in the given THz frequency range. The low absorption property of ZnO is of benefit to THz device applications. Certainly, further design is required for broadband applications [59].

4.2.4 *Ab initio* calculation and discussion

In order to understand the giant THz birefringence in ZnO, we carried out an *ab initio* band calculation and phonon calculation using CRYSTAL09 [51] which employed a hybrid exchange-correlation function B3LYP [60] and a localized basis set of Gaussian Type Functions (GTFs). All electron GTFs were used for Zn [61] and O [62]. The bandgap was calculated ~3.23 eV with full optimization of the lattice constant and oxygen position, in good agreement with the recent band calculation of M. Du and S. B. Zhang [63]. ZnO belongs to the uniaxial system with $\epsilon_{xx} = \epsilon_{yy} \neq \epsilon_{zz}$. We performed the coupled perturbed Kohn-Sham calculation [64] to get the dielectric constant tensor in the visible region; $\epsilon_{xx} = \epsilon_{yy} = 3.3891$ and $\epsilon_{zz} = 3.4213$, which give $n_o = n_{xx} = \sqrt{\epsilon_{xx}} = 1.8410$, $n_e = n_{zz} = \sqrt{\epsilon_{zz}} = 1.8497$, and the birefringence of 0.0087. Since ZnO has ionicity [65], the birefringence in the THz region is related to the difference of the LO-TO splitting between the zone center optical phonon (A_1 and E_1) in the Infrared region (few hundred wavenumber) in addition to the birefringence in the optical region. In order to calculate the birefringence in the THz region, full phonon calculations were performed [66]. For ZnO having the wurtzite structure, it is well known that the non-degenerate A_1 and doubly degenerate E_1 modes are Infrared active. Our calculation shows that the LO (TO) frequency of the A_1 mode is 589.18 cm⁻¹ (384.31 cm⁻¹) and the LO (TO) frequency of the E_1 mode is 606.38 cm⁻¹ (418.05 cm⁻¹). The relative intensity ratio of the A_1 and E_1 modes is 664 : 1270.

Symmetry analysis shows that $\epsilon_{xx} = \epsilon_{yy} = n_o^2$ is related to the E_I modes and $\epsilon_{zz} = n_e^2$ to the A_I modes. The dielectric constant tensor, $\epsilon(0)$, in the THz region can be expressed in terms of the LO and TO phonon frequencies and the dielectric constant tensor, $\epsilon(\infty)$, in the high-frequency region according to the Lyddane-Sachs-Teller relationship; $\epsilon_{xx}(0)\omega_{E_I,TO}^2 = \epsilon_{xx}(\infty)\omega_{E_I,LO}^2$ and $\epsilon_{zz}(0)\omega_{A_I,TO}^2 = \epsilon_{zz}(\infty)\omega_{A_I,LO}^2$. Having all the necessary information from the *ab initio* calculation, calculations of the complex dielectric constant tensor in the infrared region were performed. Fig. 4.6 shows the *ab initio* calculation results for the complex dielectric functions and refractive indices of ZnO in the frequency range between 0 and 30 THz for the extraordinary and ordinary waves. In this calculation, we assume the damping constant as the same value (27.3 cm^{-1}) as in ref [54]. Although it is experimentally meaning-less birefringence due to strong absorption coefficient in the frequency range over the 10 THz, we can get calculated birefringence data as shown in Fig. 4.7. To compare the experimental results, Fig. 4.8 shows the calculated and measured real part of complex refractive indices and absorption coefficients of ZnO in the frequency region of 0.25 ~ 1.35 THz with respect to the two different polarizations: the extraordinary and ordinary refractive indices. The refractive indices at 1 THz are 2.841 and 2.671 for extraordinary and ordinary waves, respectively, and thus, the birefringence at 1 THz is 0.170, which is about 20 times larger than the birefringence in the visible region. The calculation reproduces the experimental results quite well. Fig. 4.8 shows also the absorption of ZnO in two different polarizations, showing that the absorption in this region is very small for wideband applications. Our *ab initio* calculation shows that the huge birefringence in the THz region originates from the difference of the TO-LO splitting between the optical phonon branches (A_I and E_I).

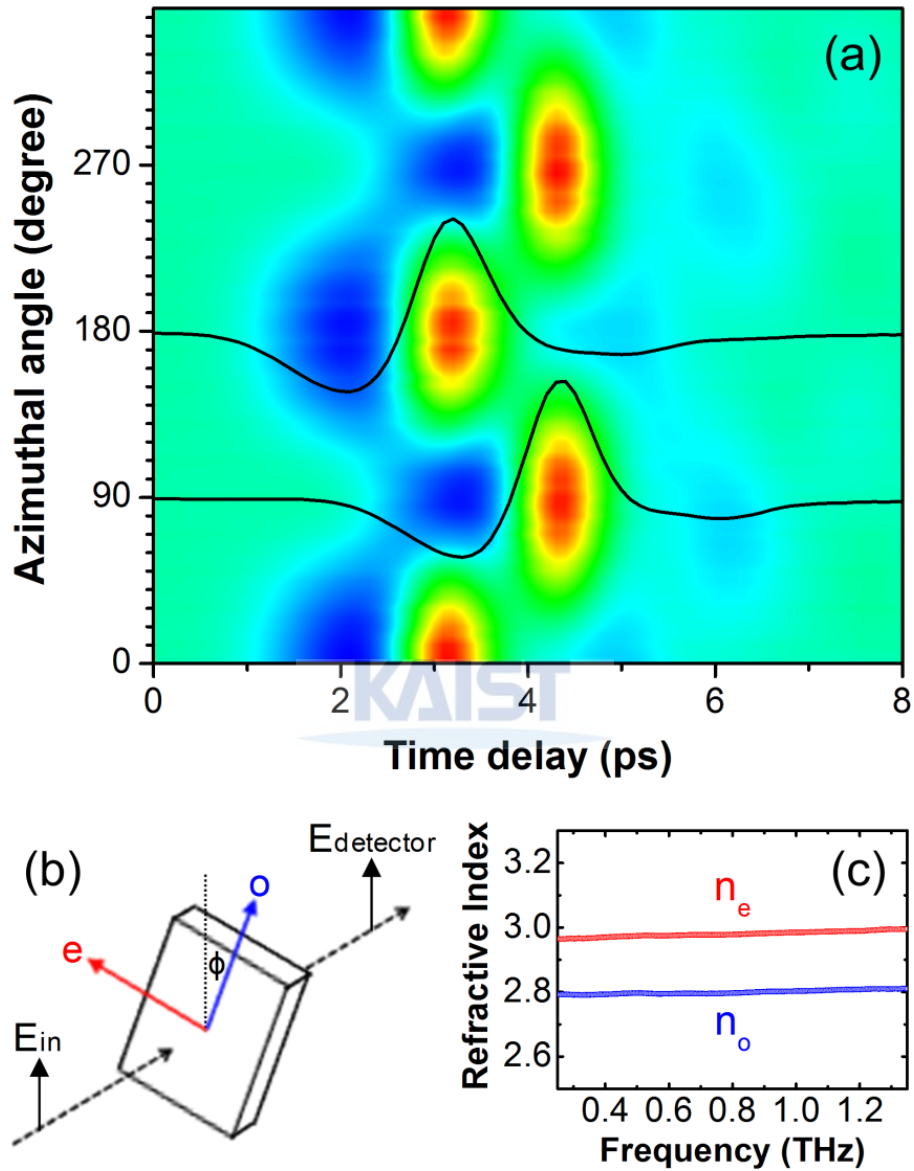


Figure 4.3: Transmitted THz waveforms (a) measured with varying the azimuthal angle ϕ of the ZnO sample in the parallel-polarization configuration illustrated in (b), and measured ordinary and extraordinary refractive indices (c) of the ZnO sample. The solid curves in (a) represent the waveforms measured at 90° and 180° , respectively.

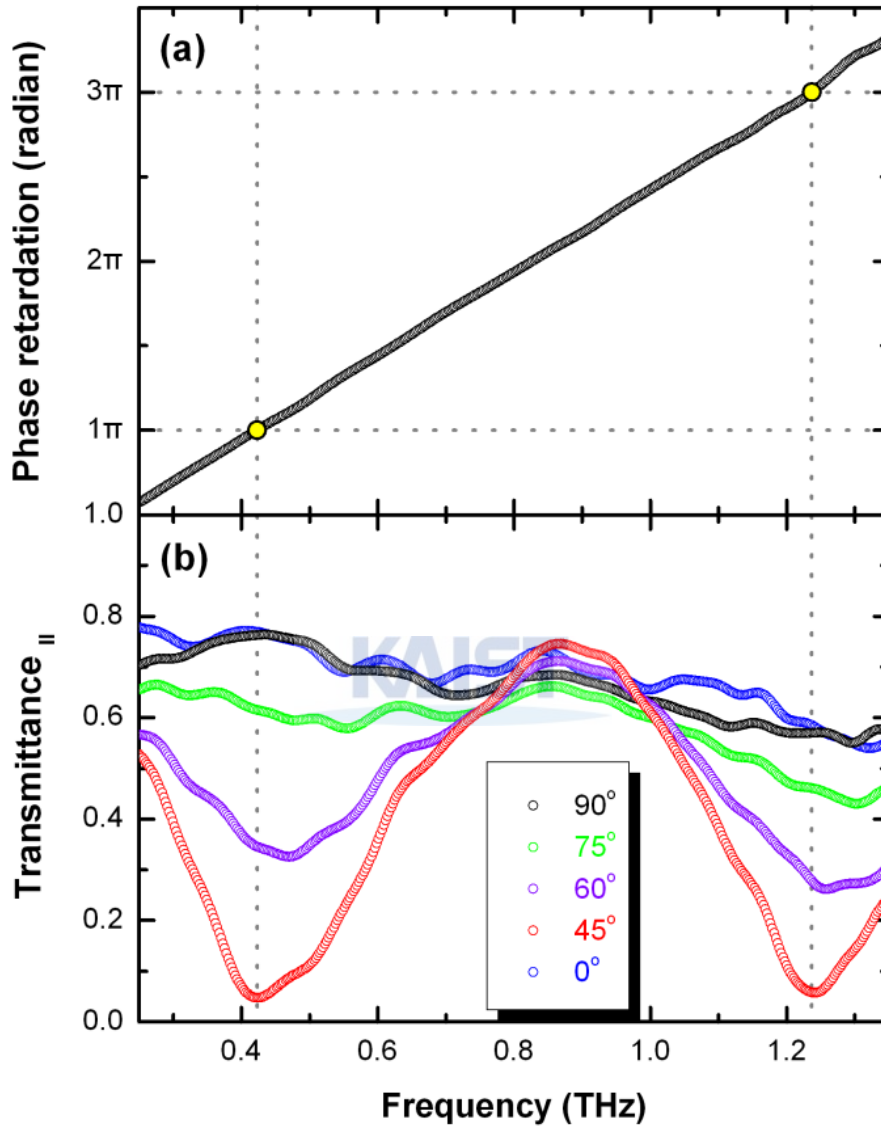


Figure 4.4: (a) Frequency-dependent phase retardation through the 2-mm-thick ZnO crystal. (b) THz transmission spectra of the 2-mm-thick ZnO crystal measured at various azimuthal angles in the parallel-polarization configuration.

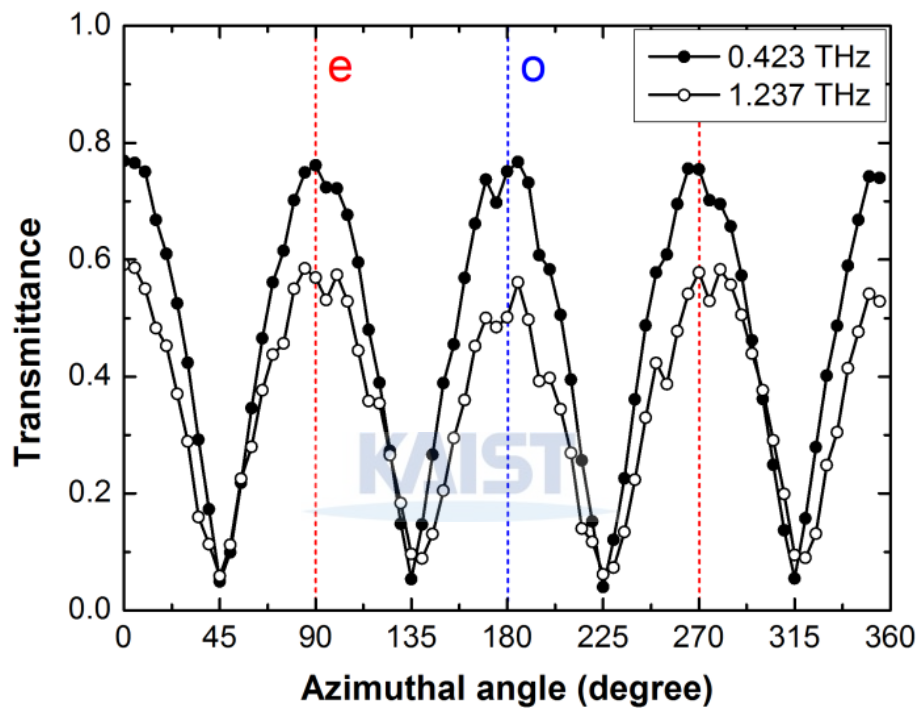


Figure 4.5: Azimuthal angle dependence of transmittances at 0.42 and 1.24 THz of the 2-mm-thick ZnO crystal, measured in the parallel-polarization configuration. The 0° (180°) and 90° (270°) orientations represent extraordinary and ordinary waves, respectively.

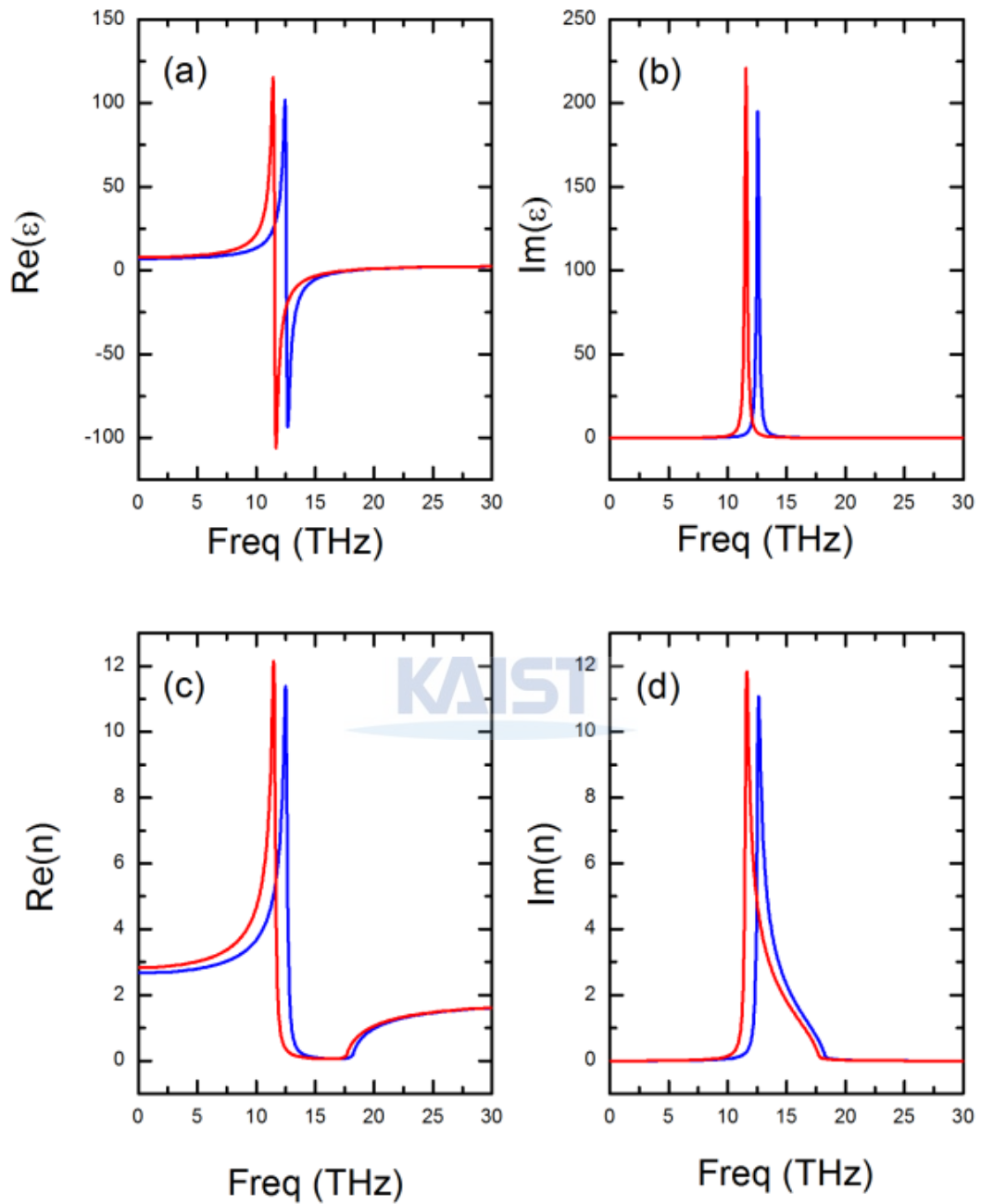


Figure 4.6: *Ab initio* calculation results for the ZnO. (a) Real and (b) imaginary part of complex dielectric constant, and (c) real and (d) imaginary part of complex refractive index of ZnO in the frequency range between 0 and 30 THz for the extraordinary (red line) and ordinary (blue line) waves, respectively.

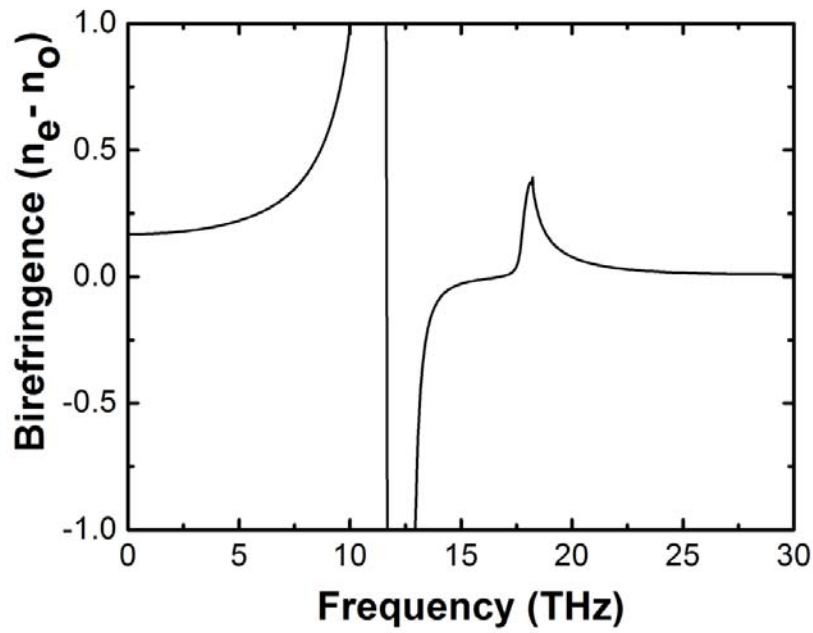


Figure 4.7: Calculated birefringence in the frequency range between 0 to 30 THz. Note that the imaginary part of the complex refractive index is huge in the larger birefringence region from 5 THz to 20 THz, as shown in Fig. 4.6.

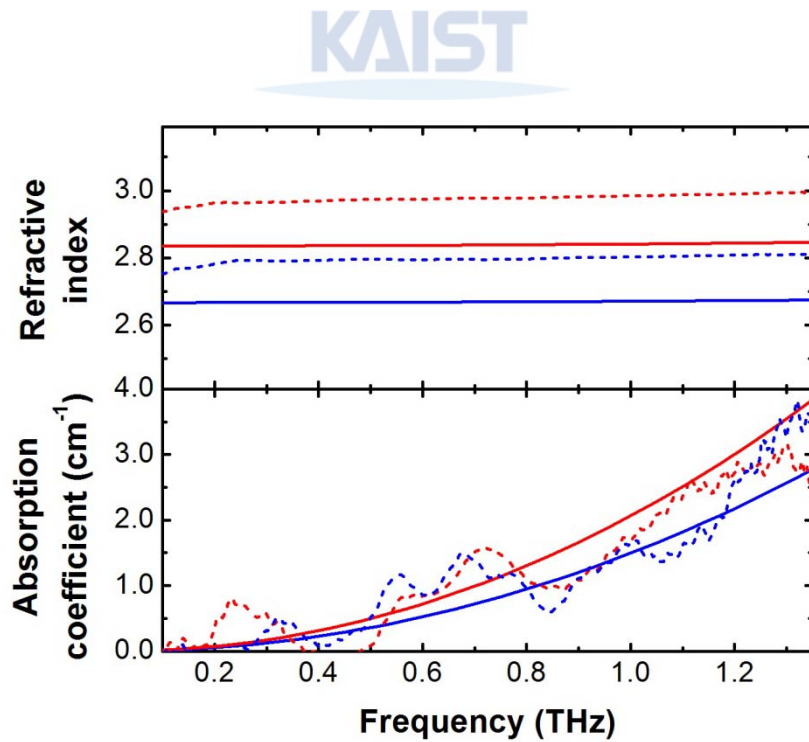


Figure 4.8: Refractive indices and absorption coefficients of ZnO in the THz region for the extraordinary (red curve) and ordinary (blue curve) waves, obtained from the *ab initio* calculation. The dashed curves indicate experimental results.

4.3 THz birefringence in LiNbO₃, and Al₂O₃

4.3.1 Introduction

Lithium niobate (LiNbO₃) is one of the considerable attractive materials for optoelectronics, due to its excellent electro-optic, acousto-optic, and nonlinear optical properties. Moreover, it has good chemical and mechanical stabilities and wide transparency range. Thus, it is widely used as electro-optic modulator and Q-switch for Nd:YAG, Nd:YLF, and Ti:Sapphire lasers as well as modulator for fiber optics. Moreover, frequency doublers (only for wavelength $> 1 \mu\text{m}$), quasi-phase-matched devices, and optical parametric oscillators pumped at 1064 nm are mostly employed for LiNbO₃ crystal. To increase its resistance to optical damage known as photorefractive damage, LiNbO₃ can be doped by magnesium oxide. Also, Fe, Zn, Hf, Cu, Gd, Er, Y, Mn, and B can be dopants. Using a Czochralski process, which is a method of crystal growth, LiNbO₃ can be grown. Recently, the researches of THz wave controlled by use of the birefringence property of the LiNbO₃ crystal, as well as optical properties of LiNbO₃ have extensively studied [67,68]. LiNbO₃ crystal has a birefringence because it has trigonal crystal system which is anisotropic system. Fig. 4.9 shows the crystal structure of LiNbO₃. Green, blue and red spheres represent the Li, Nb, and O elements, respectively.

Aluminium oxide (Al₂O₃, commonly referred to as alumina, corundum as well as many other names) is the family of inorganic compounds. It comes in different colors given by various other impurities. It has a unique combination of outstanding chemical, physical, and optical properties. Al₂O₃ crystal has a relatively large-band-gap of $\sim 9.5 \text{ eV}$ [69] and a high strength at high temperatures, good thermal properties, and excellent optical transparency. Its mechanical properties begin to decline after $800 \text{ }^\circ\text{C}$. Moreover, It is an electrical insulator but has a high thermal conductivity ($30 \text{ W m}^{-1}\text{K}^{-1}$) for a ceramic material. Thus, Al₂O₃ is generally and extensively being used as a substrate for many epitaxial films as well as commonly used for protected window from the vacuum ultraviolet to the IR spectrum range. And its hardness makes it properly suitable for use as a component in cutting tools. For example, it is widely used as a fine or coarse abrasive, including as a much less expensive substitute for industrial diamond. Fig. 4.10 shows the crystal structure of Al₂O₃. Gray and red spheres represent the Al⁺³ and O⁻² elements, respectively. As shown in Fig. 4.10, Al₂O₃ has trigonal structure that is anisotropic system.

In this chapter, we present the measurement of the extraordinary and ordinary refractive indices (n_e and n_o) of Al₂O₃ and LiNbO₃ single crystals in the frequency range of $0.25 \sim 1.40 \text{ THz}$. The THz birefringence ($\Delta n = n_e - n_o$) is measured by using a THz-TDS which is used to enable polarization sensitive THz

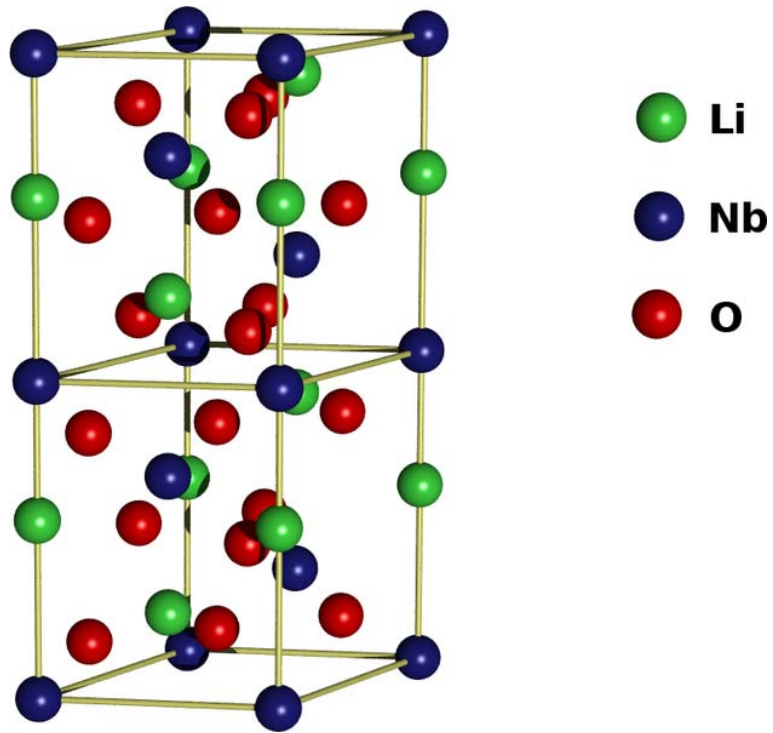


Figure 4.9: The atomic structure of LiNbO_3 . [82]

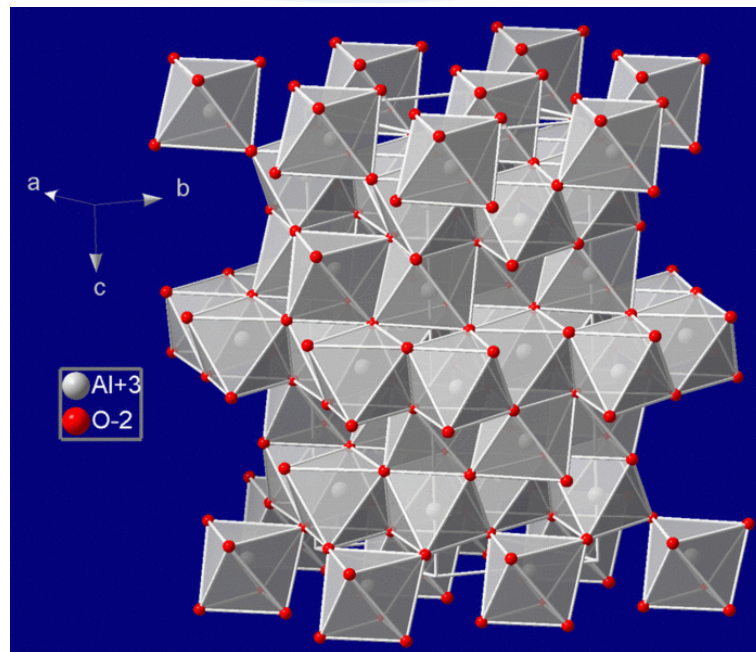


Figure 4.10: The atomic structure of Al_2O_3 . [83]

detection, demonstrated previously with zinc oxide (ZnO) [70], and the result is compared with the earlier FT-THz measurements [71,72]. For more comprehensive understanding of the THz birefringence of materials, we compared the experimental results of THz birefringence with the calculated results carried out an *ab initio* phonon calculation using CRYSTAL09 code [51]. The experimental results of the THz birefringence for the samples show good agreement with the calculated values from the full phonon considerations.

4.3.2 Polarization sensitive THz detection

The experimental configuration is illustrated in Fig. 4.11. A pump beam, the sub-picosecond infrared (800 nm) pulses from a Ti:sapphire laser oscillator, was incident on the THz emitter which was the biased photoconductive antenna (PCA). The pulsed THz waves polarized linearly along the vertical axis were generated from the PCA and focused on the sample with a spot size of ~ 2 mm. Then the THz waves transmitted through the sample were guided into the ZnTe crystal overlapping with the linearly polarized probe beam along the horizontal axis by using four off-axis parabolic mirrors. The enclosure containing the THz beam path was purged with nitrogen gas to eliminate the absorption by water vapor in ambient air. After the ZnTe crystal, the probe beam passed through a quarter wave plate (QWP) and was split by a Wollaston prism (WP) into the two orthogonal polarization components, which were then respectively sent two detectors. The intensity difference measured from the detectors between the two orthogonal polarization components was proportional to the detected THz field amplitude E_{THz} . In the theoretical calculation [73], the intensity difference is given by

$$\begin{aligned} \Delta I(\alpha, \varphi) &= I_p \frac{\omega n^3 E_{THz} r_{41} L}{2c} (\cos \alpha \sin 2\varphi + 2 \sin \alpha \cos 2\varphi), \end{aligned} \quad (4.5)$$

where I_p is the probe beam intensity, ω is the angular frequency of the probe beam, n is the refractive index of ZnTe, c is the speed of light in vacuum, r_{41} and L are the only nonzero coefficient of the electro-optic tensor and the thickness of the ZnTe, respectively. As shown in the inset at up right of Fig. 4.11, α and φ are the angles of the THz and probe beam polarizations with respect to the (001) axis of ZnTe, respectively. In our experimental condition, the angle of THz polarization is perpendicular to that of the probe beam polarization ($\varphi = \alpha + 90^\circ$).

Fig. 4.12 shows the measured THz time-domain waveforms as a function of the THz polarization angle α from 0° to 360° at a step of 10° with respect to the (001) axis of ZnTe when the probe beam polarization angle φ is fixed at 180° . It can be found from Eq.(4.5) that, ignoring the sign of THz amplitude, there

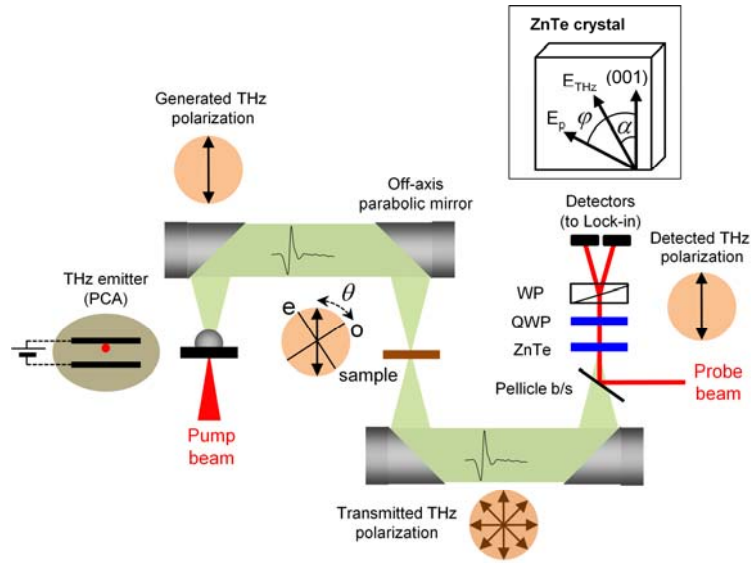


Figure 4.11: Illustration of the experimental configuration. PCA: photoconductive antenna, WP: Wollaston prism, QWP: quarter waveplate, Pellicle b/s: Pellicle beamsplitter, o: ordinary axis, and e: extraordinary axis. The directions of the generated and detected THz polarizations are depicted beside the THz emission and detection parts, respectively. The inset shows the angles of the THz and probe beam polarization directions with respect to the (001) axis of the ZnTe crystal.

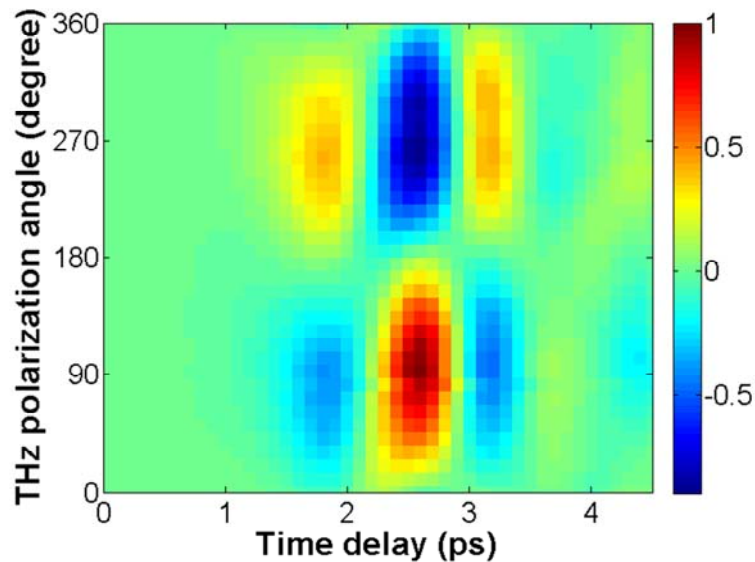


Figure 4.12: THz polarization-dependent THz time-domain waveforms (arbitrary units) measured with varying the THz polarization angle α with respect to the (001) axis of the ZnTe crystal.

are the two absolute maxima of the THz amplitude at the THz polarization angles, α , of 90° and 270° . Using this polarization sensitive THz-TDS, we measured the THz refractive indices for Al_2O_3 and LiNbO_3 crystals according to an azimuthal angle, θ , rotating them placed on the focal plane, as shown in Fig. 4.11.

4.3.3 Measurement for THz birefringence

We used single crystals of Al_2O_3 and LiNbO_3 to investigate the birefringence in THz frequency. The samples are prepared both-side polished with 0.5-mm thickness. The (10-10) crystal orientation was prepared for Al_2O_3 , and x-cut for LiNbO_3 . We note that both Al_2O_3 and LiNbO_3 crystals correspond to the trigonal structures having a uniaxial birefringence.

The reference and transmitted temporal waveforms of THz pulses, which were measured over a 34 ps in time-domain data, were recorded with and without the samples, respectively. Fig. 4.13 displays the transmitted THz waveforms measured with rotating the LiNbO_3 from 0 to 360° at a step of 5° in the THz-TDS that is described above and illustrated in the inset at top right of Fig. 4.13. The transmitted THz waveforms measured with rotating the Al_2O_3 were also measured (data not shown). The time delay position of the THz pulse oscillates with a 180° period of the azimuthal angle, θ , which implies the existence of birefringence. From the result of Fig. 4.13, we can characterize the crystal orientation of the LiNbO_3 crystal without *a priori* knowledge of the crystal orientation. For a given crystal orientation, the index of refraction of the sample is obtained by comparing the THz waveform measurements with and without the sample [58]. Briefly, the ratio between the reference and transmitted THz spectra is given by (for the notation, see Fig. 4.14)

$$\frac{\tilde{E}_{sample}(\omega)}{\tilde{E}_{reference}(\omega)} = \frac{\tilde{n}_s(\omega)(\tilde{n}_1 + \tilde{n}_2)(\tilde{n}_2 + \tilde{n}_3)}{\tilde{n}_2(\tilde{n}_1 + \tilde{n}_s(\omega))(\tilde{n}_s(\omega) + \tilde{n}_3)} e^{-i(\tilde{n}_s(\omega) - \tilde{n}_2)\omega L/c} = \rho(\omega)e^{-i\varphi(\omega)}, \quad (4.6)$$

where $\rho(\omega) = \left| \frac{\tilde{E}_{sample}(\omega)}{\tilde{E}_{reference}(\omega)} \right|$ and $\varphi(\omega) = \arg\left(\frac{\tilde{E}_{sample}(\omega)}{\tilde{E}_{reference}(\omega)}\right)$. For a sample with very low absorption, and $\tilde{n}_1 = \tilde{n}_2 = \tilde{n}_3 = 1$, the frequency-dependent real part of the complex refractive index of the sample, $n_s(\omega)$, is given by

$$n_s(\omega) = 1 + \frac{c\varphi(\omega)}{\omega d}, \quad (4.7)$$

where d is the crystal thickness and c is the speed of light. Fig. 4.15 shows the measured dispersion of extraordinary and ordinary refractive indices (n_e and n_o) for the Al_2O_3 and LiNbO_3 samples.

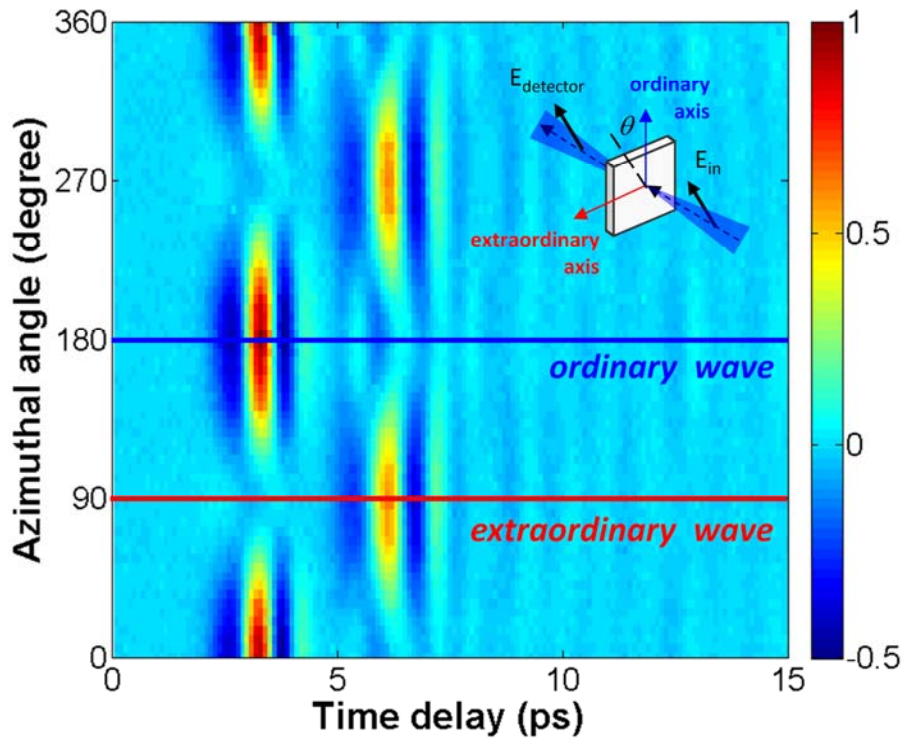


Figure 4.13: Transmitted THz time-domain waveforms (arbitrary units) measured with varying the azimuthal angle θ of the LiNbO₃.

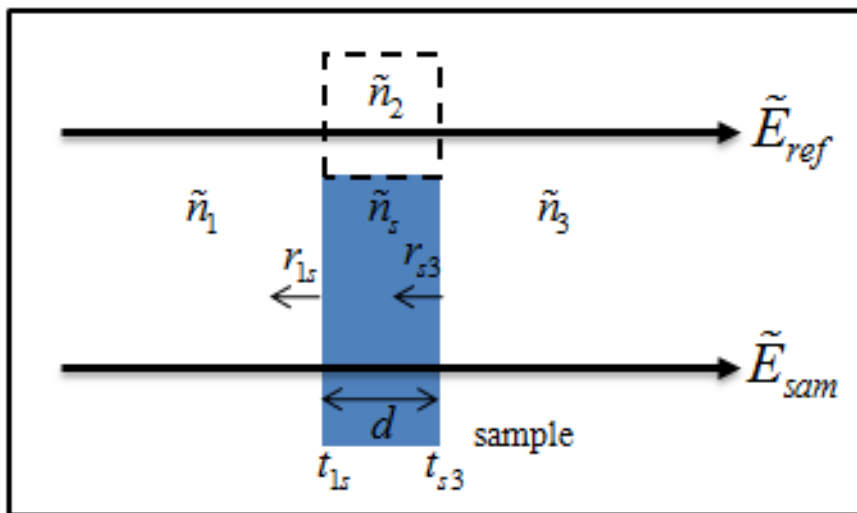


Figure 4.14: Measurement of THz waveforms with and without the sample. The frequency dependent complex refractive index of sample, $\tilde{n}_s(\omega)$, is obtained from Eqs (4.7) and (4.8).

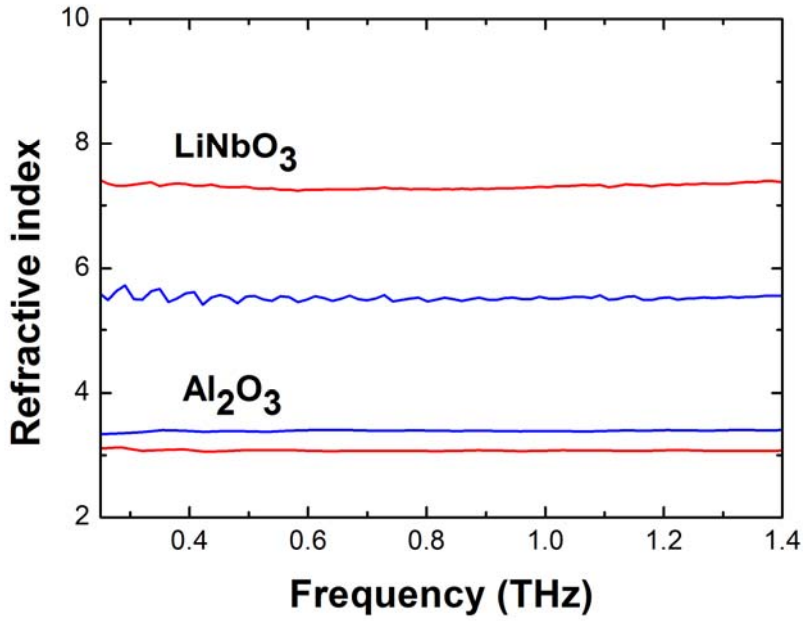


Figure 4.15: Dispersion of measured ordinary and extraordinary refractive indices of Al₂O₃ and LiNbO₃. The extraordinary and ordinary waves are indicated by the red and blue curves, respectively.

4.3.4 Calculation for THz birefringence

For more comprehensive understanding of THz birefringence, the measured birefringence is compared with the result of *ab initio* calculation. We carried out an *ab initio* phonon calculation using CRYSTAL09 which employed a hybrid exchange-correlation functional PBE0 [74] and a localized basis set of Gaussian type functions (GTFs) of Oxygen (6-31d1) and Aluminium (8-511d1) for Al₂O₃ and Lithium (6-11G) and Haywsc pseudopotential of Niobium (Haywsc-31d) and Oxygen (6-31d1) for LiNbO₃ [75]. Starting from experimentally known trigonal space group (R-3c, No. 167 for Al₂O₃ and R3c, No. 161 for LiNbO₃) [76], internal coordinates of each atom and lattice parameters are varied to minimize total energy for a given symmetry. And then coupled perturbed Kohn-Sham equation has been solved for each optimized structure in order to get dielectric function at optical frequency [77]. And finally, full phonon calculation has been applied to get phonon spectrum at zone center [78]. The calculated phonon spectrum including longitudinal and transverse phonon has been used to get frequency dependent dielectric constant in the THz region.

We also carried out reproduce the reference results, which is the dispersion of refractive indices using the fitting parameters obtained from the references. The theoretical fitting formula of the frequency-dependent dielectric function is obtained as follow. The coupling of the electric field E of the photon with the dielectric polarization of the TO phonon mode is described by the electromagnetic wave equation [50]:

$$c^2 K^2 E = \omega^2 (E + 4\pi P) \quad (4.8)$$

At low wavevectors the TO phonon frequency ω_{TO} is independent of K . And the polarization is proportional to the displacement of the positive ions relative to the negative ions, so that the equation of motion of the polarization is like that of an oscillator and may be written as, with $P = Nqu$

$$-\omega^2 P + \omega_{TO}^2 P = \left(\frac{Nq^2}{M} \right) E, \quad (4.9)$$

where there are N ion pairs of effective charge q and reduced mass M , per unit volume. Then the dielectric function obtained as

$$\varepsilon(\omega) = 1 + 4\pi \frac{P}{E} = 1 + \frac{4\pi Nq^2 / M}{\omega_{TO}^2 - \omega^2}. \quad (4.10)$$

In the frequency range from zero up through the infrared, Eq. (4.10) can be written as

$$\varepsilon(\omega) = \varepsilon(\infty) + \frac{4\pi Nq^2 / M}{\omega_{TO}^2 - \omega^2}. \quad (4.11)$$

Using a static dielectric function of $\varepsilon(0) = \varepsilon(\infty) + 4\pi Nq^2 / M \omega_{TO}^2$, we can obtain the frequency dependent dielectric function ($\varepsilon(\omega)$) as follow,

$$\varepsilon(\omega) = \varepsilon(\infty) + [\varepsilon(0) - \varepsilon(\infty)] \frac{\omega_{TO}^2}{\omega_{TO}^2 - \omega^2} = \varepsilon(\infty) \left(\frac{\omega_{LO}^2 - \omega^2}{\omega_{TO}^2 - \omega^2} \right). \quad (4.12)$$

The zero of $\varepsilon(\omega)$ defines the frequency ω_{LO} , as the pole of $\varepsilon(\omega)$ defines ω_{TO} . The zero frequency gives

$$\frac{\omega_{LO}^2}{\omega_{TO}^2} = \frac{\varepsilon(0)}{\varepsilon(\infty)}, \quad (4.13)$$

which is the Lyddane-Sachs-Teller relation. If one include a damping constant (γ), the frequency-dependent dielectric function, Eq. (4.13), should be modified as follows:

$$\varepsilon(\omega) = \varepsilon(\infty) \frac{(\omega_{LO}^2 - \omega^2 - i\gamma\omega)}{(\omega_{TO}^2 - \omega^2 - i\gamma\omega)}. \quad (4.14)$$

Thus, we can obtain the refractive index from the frequency-dependent dielectric function through the relation of $\varepsilon(\omega) = \varepsilon' + i\varepsilon'' = (n_r + in_i)^2$, where n_r and n_i correspond to the real and imaginary part of refractive index, respectively. In generally, we can reproduce the fitting results of refractive indices with reference fitting parameters using Eq. (4.14). In the case of LiNbO₃, K. Sakai obtained the fitting parameter from his experimental data using a typical relation of Eq. (4.12) [79]. The values of fitting parameters for extraordinary (ordinary) waves were $\varepsilon_\infty = 4.68(4.98)$, $\varepsilon_0 = 25.4(43.6)$, $\omega_{TO} = 210 \text{ cm}^{-1}(165 \text{ cm}^{-1})$, respectively. In the case of Al₂O₃, Baker fitted his spectra with the dielectric-function model [80] :

$$\varepsilon(\nu) = \varepsilon(\infty) + \sum_i \Delta\varepsilon_i \frac{\nu_{iTO}^2}{\nu_{iTO}^2 - \nu^2 + i\gamma_{iTO}\nu}. \quad (4.15)$$

Here, $\Delta\varepsilon_i$ is the oscillator strength. Table 4.1 lists the fitting parameters of Al_2O_3 [80,81].

Figure 4.16 shows the calculated refractive indices of Al_2O_3 and LiNbO_3 with respect to the two different polarizations from the full phonon considerations, which are the result from the *ab initio* calculation: the extraordinary and ordinary refractive indices. The measured and calculated refractive indices of the Al_2O_3 and LiNbO_3 at 1 THz are listed in Table 4.2. Our *ab initio* calculation reproduces the experimental results quite well as listed in Table 1, as well as the FT-THz measurements in Refs. [71,72]

In conclusion, we have studied the THz birefringence of Al_2O_3 and LiNbO_3 , which correspond to the trigonal structures that have a uniaxial birefringence. Using a polarization sensitive THz-TDS, we measured the extraordinary and ordinary refractive indices of the Al_2O_3 and LiNbO_3 in the frequency range of 0.25 to 1.40 THz. The experimental results of the THz birefringence for the samples show good agreement with the calculated values from the full phonon considerations. Therefore, the birefringence for the sample in the THz frequency region can be well understood in conjunction with the phonon consideration.

Table 4.1: Classical oscillator fitting parameter for Al_2O_3 [80,81].

		$\nu_i \text{ (cm}^{-1}\text{)}$	λ_i	$\Delta\varepsilon_i$	γ_i / ν_i	ν_i (longitudinal mode)	ε_∞	ε_0
Ordinary ray	Mode 1	385	26.0	0.30	0.015	388	3.2	9.395
	Mode 2	442	22.6	2.70	0.010	480		
	Mode 3	569	17.6	3.00	0.020	625		
	Mode 4	635	15.7	0.30	0.020	900		
Extraordinary ray	Mode 1	400	25.0	6.80	0.020	512	3.1	11.589
	Mode 2	583	17.1	1.70	0.035	871		

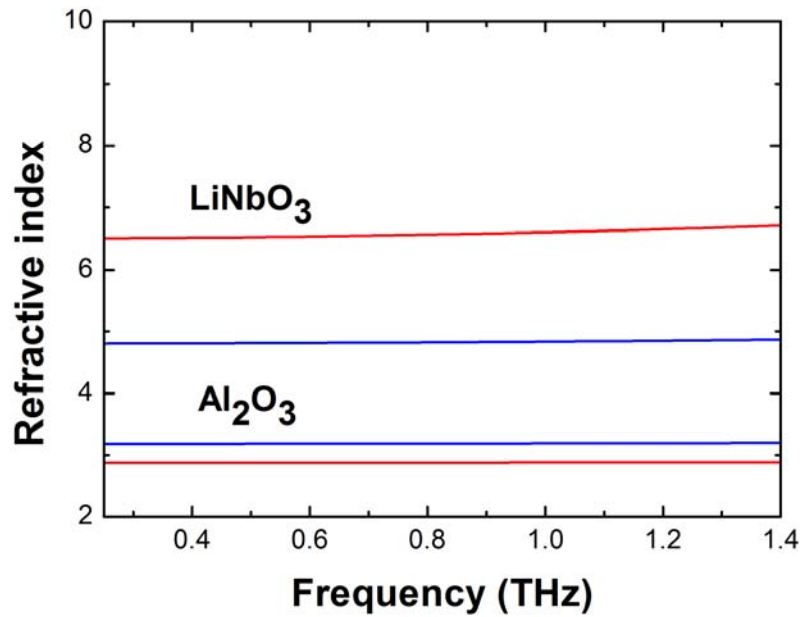


Figure 4.16: Dispersion of calculated ordinary and extraordinary refractive indices of Al_2O_3 and LiNbO_3 by using an *ab initio* calculation. The extraordinary and ordinary waves are indicated by the red and blue curves, respectively.

Table 4.2: Measured and calculated refractive indices of Al_2O_3 and LiNbO_3 at 1 THz.

Refractive index @ 1 THz	Al_2O_3			LiNbO_3		
	n_e	n_o	Δn	n_e	n_o	Δn
Measurement	3.07	3.39	-0.32	7.29	5.51	1.78
Calculation	2.88	3.19	-0.31	6.60	4.83	1.77
Reference [24,25]	3.09	3.41	-0.32	6.72	5.09	1.63

4.4 Discussion

We have developed a polarization sensitive THz-TDS. Using this technique, we have studied the THz birefringence of the ZnO, Al₂O₃, and LiNbO₃ crystals. The results are verified with *ab initio* calculations. The birefringence of ZnO, which corresponds to the hexagonal structure, measured about 0.180 in the 0.25~1.35 THz frequency range shows good agreement with the calculated value of 0.170 from the full phonon consideration. This huge birefringence of ZnO in the THz frequency region is well understood in conjunction with the TO-LO phonon splitting. Furthermore, we have studied the THz birefringence of Al₂O₃ and LiNbO₃, which correspond to the trigonal structures that have a uniaxial birefringence. Using a polarization sensitive THz-TDS, we measured the extraordinary and ordinary refractive indices of the Al₂O₃ and LiNbO₃ in the frequency range of 0.25 to 1.40 THz. The experimental results of the THz birefringence for the samples show good agreement with the calculated values from the full phonon considerations. Therefore, the birefringence for the sample in the THz frequency region can be well understood in conjunction with the phonon consideration.



Chapter 5. Conclusions

In this thesis, we have newly developed and demonstrated various high-speed, high-resolution, and polarization-sensitive THz spectroscopic techniques. In addition, using a polarization-sensitive THz measurement setup, we have comprehensively studied material birefringence in THz frequency range for a number of uniaxial crystals, such as ZnO, LiNbO₃, and Al₂O₃ crystals.

We have devised and demonstrated a number of new high-speed, high-resolution THz spectroscopy techniques. They are (1) wavelet power spectrum estimation technique (WPSET), (2) THz frequency-comb multiheterodyne spectroscopy (TFCMS), and (3) electronically controlled optical sampling (ECOPS) THz-TDS. In WPSET, the wavelets used in power spectrum efficiently have suppressed measurement noise and enhanced the retrieved spectral quality. Although this work has been focused on THz frequency region, this WPSET method can also be applied to high-resolution spectroscopy in other frequency regions. Secondly, TFCMS is a new type of high resolution time-domain THz spectroscopic methods, which has been firstly demonstrated in this thesis. The high resolution capability of TFCMS has been demonstrated with gaseous materials of water and ammonia. Finally, ECOPS is a modified version ASOPS, which shows high speed time-domain spectroscopy in such a way that the frequency difference is electronically swept at a rate of up to 1 kHz. It has been confirmed that ECOPS can exactly reproduce a THz pulse of distortion-free spectrum, equivalent to a typical ASOPS measurement, by adopting a proper calibration of time-delay. The measurement time has been reduced by a factor of 50 in ECOPS compared with in ASOPS. Among the THz-TDS methods as known today, the devised ECOPS THz-TDS has achieved the most rapid measurement in terms of a measurement time taken to reach a desired SNR. This high-speed ECOPS THz-TDS has potential applications such as real-time monitoring or sensing based on THz spectra and rapid THz spectroscopic imaging.

Additionally, we have developed polarization-sensitive THz spectroscopic technique. Using this technique, we have comprehensively studied THz birefringence of uniaxial crystals, such as ZnO, LiNbO₃, and Al₂O₃. Experimental measurements using polarization-sensitive THz-TDS have been compared with theoretical results based on *ab initio* calculation. The birefringence of ZnO measured about 0.18 in the 0.25 - 1.35 THz frequency range has shown good agreement with the calculated value of 0.170 from the full phonon consideration. This huge birefringence of ZnO in the THz frequency region is well understood in conjunction with the TO-LO phonon splitting. Furthermore, we have studied the THz birefringence of the LiNbO₃, and Al₂O₃ crystals in trigonal structures. The uniaxial birefringence of these materials have been investigated us-

ing a polarization sensitive THz-TDS, and the extraordinary and ordinary refractive indices of the Al_2O_3 and LiNbO_3 have been measured in the frequency range of 0.25 to 1.40 THz. The experimental results of the THz birefringence for the samples show good agreement with the calculated values from the full phonon considerations. Therefore, the birefringence for the sample in the THz frequency region can be well understood in conjunction with the phonon consideration.



References

- [1] X.-C. Zhang and J. Xu, *Introduction to THz wave photonics*, (Springer, New York, 2010).
- [2] B. Ferguson and X.-C. Zhang, "Materials for terahertz science and technology," *Nat. Mater.* **1**, 26 (2002).
- [3] M. Tonouchi, *Nat. Photonics*, "Cutting-edge terahertz technology," **1**, 97 (2007).
- [4] L. B. Braly, J. D. Cruzan, K. Liu, R. S. Fellers, and R. J. Saykally, "Terahertz laser spectroscopy of the water dimer intermolecular vibrations. I. (D₂O)₂," *J. Chem. Phys.* **112**, 10293 (2000).
- [5] B. B. Jin, P. Kuzel, F. Kadlec, T. Dahm, J. M. Redwing, A. V. Pogrebnyakov, X. X. Xi, and N. Klein, "Terahertz surface impedance of epitaxial MgB₂ thin film," *Appl. Phys. Lett.* **87**, 092503 (2005).
- [6] F. N. Keutsch, M. G. Brown, P. B. Petersen, R. J. Saykally, M. Geleijns, and A. V. D. Avoird, "Terahertz vibration-rotation-tunneling spectroscopy of water clusters in the translational band region of liquid water," *J. Chem. Phys.* **114**, 3994 (2001).
- [7] Y.-S. Lee, *Principles of terahertz science and technology*, (Springer, New York, 2009).
- [8] B. B. Hu and M. C. Nuss, "Imaging with terahertz waves," *Opt. Lett.* **20**, 1716 (1995).
- [9] K. Kawase, Y. Ogawa, Y. Watanabe, and H. Inoue, "Non-destructive terahertz imaging of illicit drugs using spectral fingerprints," *Opt. Express* **11**, 2549 (2003).
- [10] J. B. Jackson, M. Mourou, J.F. Whitaker, I.N. Duling III, S.L. Williamson, M. Menu, and G.A. Mourou, "Terahertz imaging for non-destructive evaluation of mural paintings," *Opt. Commun.* **281**, 527 (2008).
- [11] M. van Exter, C. Fattinger, and D. Grischkowsky, "Terahertz time-domain spectroscopy of water vapor," *Opt. Lett.* **14**, 1128 (1989).
- [12] D. Grischkowsky, S. Keiding, M. van Exter, and C. Fattinger, "Far-infrared time-domain spectroscopy with terahertz beams of dielectrics and semiconductors," *J. Opt. Soc. Am. B* **7**, 2006 (1990).
- [13] E. Pickwell, and V. P. Wallace, "Biomedical applications of terahertz technology," *J. Phys. D: Appl. Phys.* **39**, R301 (2006).
- [14] H. Hoshina, T. Seta, T. Iwamoto, I. Hosako, C. Otani, and Y. Kasai, "Precise measurement of pressure broadening parameters for water vapor with a terahertz time-domain spectrometer," *J. Quant. Spectrosc. Radiat. Transfer.* **109**, 2303 (2008).
- [15] G. J. Kim, S. G. Jeon, J. I. Kim, and Y. S. Jin, "Fast scanning of a pulsed terahertz signal using an

- oscillating optical delay line,” *Rev. Sci. Instrum.* **79**, 106102 (2008).
- [16] T. Yasui, E. Saneyoshi, and T. Araki, “Asynchronous optical sampling terahertz time-domain spectroscopy for ultrahigh spectral resolution and rapid data acquisition,” *Appl. Phys. Lett.* **87**, 061101 (2005).
- [17] A. Bartels, A. Thoma, C. Janke, T. Dekorsy, A. Dreyhaupt, S. Winnerl, and M. Helm, “High-resolution THz spectrometer with kHz scan rates,” *Opt. Express* **14**, 430 (2006).
- [18] A. Bartels, R. Cerna, C. Kistner, A. Thoma, F. Hudert, C. Janke, and T. Dekorsy, “Ultrafast time-domain spectroscopy based on high-speed asynchronous optical sampling,” *Rev. Sci. Instrum.* **78**, 035107 (2007).
- [19] G. Klatt, R. Gebbs, C. Janke, T. Dekorsy, and A. Bartels, “Rapid-scanning terahertz precision spectrometer with more than 6 THz spectral coverage,” *Opt. Express* **17**, 22847 (2009).
- [20] D.-S. Yee, Y. Jang, Y. Kim, and D.-C. Seo, “Terahertz spectrum analyzer based on frequency and power measurement,” *Opt. Lett.* **35**, 2532 (2010).
- [21] R. Dovesi, V. R. Saunders, C. Roetti, R. Orlando, C. M. Zicovich-Wilson, F. Pascale, B. Civalleri, K. Doll, N. M. Harrison, I. J. Bush, Ph. D’Arco, and M. Llunell, *CRYSTAL09 (CRYSTAL09 User's Manual, University of Torino, Torino, 2009)*.
- [22] A. D. Becke, “Density-functional thermochemistry. III. The role of exact exchange,” *J. Chem. Phys.* **98**, 5648 (1993).
- [23] C. Janke, M. Först, M. Nagel, H. Kurz, and A. Bartels, “Asynchronous optical sampling for high-speed characterization of integrated resonant terahertz sensors,” *Opt. Lett.* **30**, 1405 (2005).
- [24] T. Yasui, Y. Kabetani, E. Saneyoshi, S. Yokoyama, and T. Araki, “Terahertz frequency comb by multifrequency-heterodyning photoconductive detection for high-accuracy, high-resolution terahertz spectroscopy,” *Appl. Phys. Lett.* **88**, 241104 (2006).
- [25] S. Yokoyama, R. Nakamura, M. Nose, T. Araki, and T. Yasui, “Terahertz spectrum analyzer based on a terahertz frequency comb,” *Opt. Express* **16**, 13052 (2008).
- [26] P. A. Elzinga, R. J. Kneisler, F. E. Lytle, Y. Jiang, G. B. King, and N. M. Laurendeau, “Pump/probe method for fast analysis of visible spectral signatures utilizing asynchronous optical sampling,” *Appl. Opt.* **26**, 4303 (1987).
- [27] C. Kistner, A. Andre, T. Fischer, A. Thoma, C. Janke, A. Bartels, T. Gisler, G. Maret, and T. Dekorsy, “Hydration dynamics of oriented DNA films investigated by time-domain terahertz spectroscopy,” *Appl. Phys. Lett.* **90**, 233902 (2007).
- [28] D. M. Mittleman, R. H. Jacobsen, R. Neelamani, R. G. Baraniuk, and M. C. Nuss, “Gas sensing us-

- ing terahertz time-domain spectroscopy,” *Appl. Phys. B* **67**, 379 (1998).
- [29] B. Ferguson, and D. Abbott, “De-noising techniques for terahertz responses of biological samples,” *Microelectronics Journal* **32**, 943 (2001).
- [30] B. Ferguson, and D. Abbott, “Wavelet de-noising of optical terahertz pulse imaging data,” *Fluctuation and Noise Letters* **1**, L65 (2001).
- [31] D. M. Mittleman, M. Gupta, R. Neelamani, R.G. Baraniuk, J. V. Rudd, and M. Koch, “Recent advances in terahertz imaging,” *Appl. Phys. B* **68**, 1085 (1999).
- [32] S. G. Mallat, *A wavelet tour of signal processing* (Elsevier Academic Press, 1999).
- [33] P. Moulin, “Wavelet thresholding techniques for power spectrum estimation,” *IEEE Trans. Signal Processing* **42**, 3126 (1994).
- [34] D. L. Donoho, and I. M. Johnstone, “Ideal spatial adaptation by wavelet shrinkage,” *Biometrika* **81**, 425 (1994).
- [35] Y. Hu, P. Huang, L. Guo, X. Wang, and C. Zhang, “Terahertz spectroscopic investigations of explosives,” *Phys. Lett. A* **359**, 728 (2006).
- [36] P. R. Griffiths and J. A. de Haseth, *Fourier Transform Infrared Spectrometry* (Wiley, New York, 1986).
- [37] S. Schiller, “Spectrometry with frequency combs,” *Opt. Lett.* **27**, 766 (2002).
- [38] F. Keilmann, C. Gohle, and R. Holzwarth, “Time-domain mid-infrared frequency-comb spectrometer,” *Opt. Lett.* **29**, 1542 (2004).
- [39] A. Schliesser, M. Brehm, F. Keilmann, and D. W. van der Weide, “Frequency-comb infrared spectrometer for rapid, remote chemical sensing,” *Opt. Express* **13**, 9029 (2005).
- [40] I. Coddington, W. C. Swann, and N. R. Newbury, “Coherent multiheterodyne spectroscopy using stabilized optical frequency combs,” *Phys. Rev. Lett.* **100**, 013902 (2008).
- [41] D. W. van der Weide, J. Murakowski, and F. Keilmann, “Gas-absorption spectroscopy with electronic terahertz techniques,” *IEEE Trans. Microwave Theory Tech.* **48**, 740 (2000).
- [42] T. Yasui, Y. Kabetani, E. Saneyoshi, S. Yokoyama, and T. Araki, “Terahertz frequency comb by multifrequency-heterodyning photoconductive detection for high-accuracy, high-resolution terahertz spectroscopy,” *Appl. Phys. Lett.* **88**, 241104 (2006).
- [43] Y. Kim, D.-S. Yee, J. C. Ye, and J. Ahn, in *Conference on Lasers and Electro-Optics/International Quantum Electronics Conference and Photonic Applications Systems Technologies*, Technical Digest (CD) (Optical Society of America, 2009), paper CMX4.
<http://www.opticsinfobase.org/abstract.cfm?URI=CLEO-2009-CMX4>.

- [44] H. Harde, J. Zhao, M. Wolff, R. A. Cheville, and D. Grischkowsky, "THz time-domain spectroscopy on ammonia," *J. Phys. Chem. A* **105**, 6038 (2001).
- [45] H. Liu, Y. Chen, T. Yuan, F. A. Douser, J. Xu, and X.-C. Zhang, "Quantitative analysis of ammonia by THz time-domain spectroscopy," *Proc. SPIE* **5268**, 43 (2004).
- [46] F. Tauser, C. Rausch, J. H. Posthumus, and F. Lison, "Electronically controlled optical sampling using 100 MHz repetition rate fiber lasers," *Proc. SPIE* **6881**, 68810O (2008).
- [47] S. Kray, F. Spöler, T. Hellerer, and H. Kurz, "Electronically controlled coherent linear optical sampling for optical coherence tomography," *Opt. Express* **18**, 9976 (2010).
- [48] Y. Kim, D. S. Yee, M. Yi, and J. Ahn, "High-speed high-resolution terahertz spectrometers," *J. Korean Phys. Soc.* **56**, 255 (2010).
- [49] J. C. Decius and R. M. Hexter, *Molecular vibrations in Crystal*, (McGraw-Hill, New York, 1977).
- [50] C. Kittel, *Introduction to Solid State Physics*, (John Wiley & Sons, 2005).
- [51] R. Dovesi, V. R. Saunders, C. Roetti, R. Orlando, C. M. Zicovich-Wilson, F. Pascale, B. Civalleri, K. Doll, N. M. Harrison, I. J. Bush, Ph. D'Arco, and M. Llunell, *CRYSTAL09 (CRYSTAL09 User's Manual*, University of Torino, Torino, 2009).
- [52] C. Jagadish and S. J. Pearton, *Zinc Oxide Bulk, Thin Films and Nanostructures: Processing, Properties and Applications* (Elsevier, Oxford, 2006).
- [53] S. Ono, H. Murakami, A. Quema, G. Diwa, N. Sarukura, R. Nagasaka, Y. Ichikawa, H. Ogino, E. Ohshima, A. Yoshikawa, and T. Fukuda, "Generation of terahertz radiation using zinc oxide as photoconductive material excited by ultraviolet pulses," *Appl. Phys. Lett.* **87**, 261112 (2005).
- [54] A. K. Azad, J. Han, and W. Zhang, "Terahertz dielectric properties of high-resistivity single-crystal ZnO," *Appl. Phys. Lett.* **88**, 021103 (2006).
- [55] Y. S. Park and J. R. Schneider, "Index of refraction of ZnO," *J. Appl. Phys.* **39**, 3049 (1968).
- [56] W. L. Bond, *J. Appl. Phys.* "Measurement of the refractive indices of several crystals," **36**, 1674 (1965).
- [57] T. Yasui, E. Saneyoshi, and T. Araki, "Asynchronous optical sampling terahertz time-domain spectroscopy for ultrahigh spectral resolution and rapid data acquisition," *Appl. Phys. Lett.* **87**, 061101 (2005).
- [58] S. P. Micken and X.-C. Zhang, "T-ray sensing and imaging," *IJHSES.* **13**, 601 (2003).
- [59] J.-B. Masson and G. Gallot, "Terahertz achromatic quarter-wave plate," *Opt. Lett.* **31**, 265 (2006).
- [60] A. D. Becke, "Density-functional thermochemistry. III. The role of exact exchange," *J. Chem. Phys.* **98**, 5648 (1993).

- [61] J. E. Jaffe and A. C. Hess, "Hartree-Fock study of phase changes in ZnO at high pressure," *Phys. Rev B* **48**, 7903 (1993).
- [62] M. D. Towler, N. L. Allan, N. M. Harrison, V. R. Saunders, W. C. Mackrodt, and E. Apra, "Ab initio study of MnO and NiO," *Phys. Rev. B* **50**, 5041 (1994).
- [63] M.-H. Du and S. B. Zhang, "Impurity-bound small polarons in ZnO: Hybrid density functional calculations," *Phys. Rev. B* **80**, 115217 (2009).
- [64] M. Ferrero, M. Rerat, R. Orlando, and R. Dovesi, "The calculation of static polarizabilities of 1-3D periodic compounds. the implementation in the crystal code," *J. Comput. Chem.* **29**, 1450 (2008).
- [65] Mulliken charge analysis shows that the charge of Zn ion is +1.155e and that of Oxygen is -1.155 e, whereas Born charge tensor analysis, related with phonon vibration, shows that the Zn ion has +2.056e dynamic charge and the Oxygen ion has -2.056e dynamic charge.
- [66] F. Pascale, C. M. Zicovich-Wilson, F. L. Gejo, B. Civalleri, R. Orlando, and R. Dovesi, "The calculation of the vibrational frequencies of crystalline compounds and its implementation in the CRYSTAL code," *J. Comput. Chem.* **25**, 888 (2004).
- [67] D. Li, G. Ma, J. Ge, S. Hu, and N. Dai, "Terahertz pulse shaping via birefringence in lithium niobate crystal," *Appl. Phys. B* **94**, 623 (2009).
- [68] S. Kojima, N. Tsumura, H. Kitahara, M. W. Takeda, S. Nishizawa, "Terahertz time domain spectroscopy of phonon-polaritons in ferroelectric lithium niobate crystals," *Jpn. J. Appl. Phys. Part 1* **41**, 7033 (2002).
- [69] *Sov. Phys. Sol. St.* **21**, 47 (1979).
- [70] Y. Kim, J. Ahn, B. G. Kim, and D.-S. Yee, "Terahertz birefringence in zinc oxide," *Jpn. J. Appl. Phys.* **15**, 103 (2011).
- [71] E. D. Palik, *Handbook of Optical Constants of Solids II* (Academic, New York, USA, 1985), p. 765.
- [72] E. D. Palik, *Handbook of Optical Constants of Solids I* (Academic, New York, USA, 1985), p. 700.
- [73] P. C. M. Planken, H.-K. Nienhuys, H. J. Bakker, and T. Wenckebach, "Measurement and calculation of the orientation dependence of terahertz pulse detection in ZnTe," *J. Opt. Soc. Am. B* **18**, 313 (2001).
- [74] C. Adamo and V. Barone, "Toward reliable density functional methods without adjustable parameters: the PBE0 model," *J. Chem. Phys.* **110**, 6158 (1999).
- [75] http://www.crystal.unito.it/Basis_Sets/Ptable.html.
- [76] ICSD (International Crystal Structure database) website, ID 5674 for Al₂O₃ and ID 11588 for

LiNbO₃.

- [77] M. Ferrero, M. Rérat, R. Orlando, and R. Dovesi, “Coupled perturbed Hartree-Fock for periodic systems: the role of symmetry and related computational aspects,” *J. Chem. Phys.* **128**, 014110 (2008).
- [78] C.M. Zicovich-Wilson, F. J. Torres, F. Pascale, L. Valenzano, R. Orlando, and R. Dovesi, “Ab initio simulation of the IR spectra of pyrope, grossular and andradite,” *J. Comput. Chem.* **29**, 2268 (2008).
- [79] K. Sakai, *Appl. Phys.* “Michelson-type Fourier Spectrometer for the far infrared,” **11**, 2894 (1972).
- [80] A. S. Barker, “Infrared Lattice Vibrations and Dielectric Dispersion in Corundum,” *Phys. Rev.* **132**, 1474 (1963).
- [81] J. Fontanella, C. Andeen, and D. Schuele, “Low-frequency dielectric constants of α -quartz, sapphire, MgF₂, and MgO,” *J. Appl. Phys.* **45**, 2852 (1974).
- [82] http://en.wikipedia.org/wiki/Lithium_niobate.
- [83] <http://en.wikipedia.org/wiki/Sapphire>.

The logo for KAIST (Korea Advanced Institute of Science and Technology) is displayed in a light blue color. It consists of the letters 'KAIST' in a bold, sans-serif font, with a horizontal line underneath the letters.

요 약 문

고속, 고분해능, 그리고 편광 민감 테라헤르츠 분광 기술 개발에 관한 연구

한 대의 펄스 레이저와 선형 모터 스테이지를 사용하여 시간 지연을 주는 기존의 테라헤르츠 시간영역 분광 기술에서 전체 시간 지연 구간이 주파수 분해능과 반비례 관계가 있기 때문에 빠른 측정과 정밀한 주파수 분해능을 함께 구현하는 것이 어려운 과제였다. 최근, 모터로 구동되는 선형 스테이지를 사용하지 않고, 약간 다른 반복 주파수를 갖는 두 대의 펄스 레이저를 사용하는 비동기성 광 샘플링 방법이 테라헤르츠 시간영역 분광(THz-TDS)에 적용되었다. 이 방법을 이용하면 기존의 테라헤르츠 시간영역 분광에서 높은 주파수 분해능과 짧은 측정 시간을 함께 구현하지 못하는 한계를 극복할 수 있으며, 모터로 구동되는 선형 스테이지를 사용하면서 발생하는 진동과 빔 정렬에 따른 오차를 제거할 수 있다. 비록 비동기성 광 샘플링 기술이 개발되어 초고속 시간 분해 분광에 사용된 것이 1987 년이지만 2005 년이 되어서야 테라헤르츠 시간영역 분광에 처음으로 적용되었다. 그러므로 이전의 테라헤르츠 분광에 대한 연구는 다양한 발전 가능성을 가지고 있으며 측정 속도 향상과 같은 분광 기술의 개발이 가능하다.

본 논문에서는 고속, 고분해능, 그리고 편광 민감 테라헤르츠 분광 기술을 개발하고 시연하였다. 특히, 편광 민감 테라헤르츠 시간 영역 분광기를 이용하여 ZnO, LiNbO₃, 그리고 Al₂O₃ 단결정에서의 테라헤르츠 복굴절에 대한 측정을 수행하였으며 이 결과를 이론적인 계산인 *ab-initio* 계산 결과와 비교하였다. 먼저 고속 고분해능 테라헤르츠 분광으로서 비동기성 광 샘플링 테라헤르츠 시간영역 분광 (asynchronous optical sampling THz-TDS)과 테라헤르츠 주파수 빔 분광 (THz frequency comb spectroscopy)을 구현하였다. 이 때 두 대의 펄스 레이저의 반복 주파수를 안정화시켰으며, 차주파수를 최적화 시켰다. 다음으로, 새로운 고속 고분해능 테라헤르츠 시간영역 분광 기술인 (1) 웨이블릿 파워 스펙트럼 추정 기술 (wavelet power spectrum estimation technique), (2) 테라헤르츠 주파수 빔 다중헤테로다인 분광(terahertz frequency comb multiheterodyne spectroscopy), 그리고 (3) 전기적으로 제어되는 광 샘플링 방식의 테라헤르츠 시간영역 분광 (electronically controlled optical sampling THz-TDS)을 구현하였다. 웨이블릿 파워 스펙트럼 추정 기술은 노이즈 제거 기술로서 고분해능 테라헤르츠 시간영역 분광에 적용되었다. 또한 고분해능 분광 기술로서 새로운 THz-TDS 기술인 테라헤르츠 다중헤테로다인 분광 기술을 이용하여 수증기와 암모니아 가스의 흡수선을 정확히 측정하였다. 그리고 고속 측정 기술인 전기적으로 제어되는 광 샘플링 방식의 THz-TDS 을 시연하였다. 이 방법을 이용하여 측정된 테라헤르츠 펄스가 시간 영역과 주파수 영역에서 왜곡되지 않았다는 것을 비동기성 광 샘플링 방식으로 측정된 결과와 비교하여 확인하였다. 마지막으로, 편광 민감 THz-TDS 를 개발하여 이것을 이용하여 ZnO, LiNbO₃, 그리고 Al₂O₃ 와 같이 테라헤르츠 영역에서 복굴절을 갖는 물질에 대하여 실험적으로 굴절율을 측정하였으며 이 결과를 *ab-initio* 계산을 이용한 이론적인 계산 결과와 비교하여 테라헤르츠 영역에서의 복굴절 물질 대한 정확한 측정 및 계산을 수행 하였다.

핵심어: 테라헤르츠, 테라헤르츠 시간영역 분광, 비동기성 광샘플링, 복굴절